UNIVERSITYOF CALIFORNIA

Santa Barbara

Investigation of p-type GaN / AlGaN superlattices:

Defining a pathway towards low sheet resistance for p-channel III-nitride devices

A dissertation submitted in partial satisfaction of the

requirements for the degree Doctor of Philosophy in

Electrical and Computer Engineering

by

Athith Krishna

Committee in charge:

Professor Umesh K Mishra, Chair

Professor Steven Denbaars

Professor Shuji Nakamura

Professor James Speck

Dr. Stacia Keller, Principal Development Engineer

June 2022

The dissertation of Athith Krishna is approved.

_____

Dr. Stacia Keller

_____

Prof. James Speck

_____

Prof. Shuji Nakamura

_____

Prof. Steven Denbaars

_____

Prof. Umesh K Mishra, Committee Chair

May 2022

Investigation of p-type GaN / AlGaN superlattices:

Defining a pathway towards low sheet resistance for p-channel III-nitride devices

by

Athith Krishna

ACKNOWLEDGEMENTS

I consider it a great honor to thank the multiple individuals and groups who have helped me through my years at UCSB, and who have greatly contributed to the work presented here.

The first person I would like to thank is my advisor, Prof. Umesh Mishra, for accepting me into his group, giving me an opportunity to work in a world-class research environment, and being a wonderful guide throughout the entire process. Umesh has created an extremely productive and collaborative setting in the research group which allowed me to explore and grow tremendously over the last 5 years. While we always got the best advise on semiconductor electronics from him, it was always followed by a lesson or two about life which I enjoyed the most and will forever hold dear to my heart. When I started at UCSB, Umesh mentioned that Dr. Stacia Keller would be most important person for my PhD. work at UCSB, and he could not be more correct. It has been an immense pleasure to learn from Stacia about MOCVD growth, and work with her closely. Her excitement about research and science constantly rubs off onto us and pushes us to be better at what we do, on a daily basis. Every conversation I've had with her has ended up with me learning something new about our field, and it is almost like conversing with a walking treasure trove of knowledge. I would also like to thank Prof. Steven DenBaars, Prof. Shuji Nakamura and Prof. James Speck for being on my doctoral committee.

I would like to thank the MOCVD staff – Brian Carralejo, David Whitlach and Mike Iza, for all the help they provided with making sure the MOCVD machines and the lab equipment remained stable even through multiple shutdowns, tool failures, (and even a

natural disaster – the Thomas fire). Not sure how thanking a machine would work, but I wholeheartedly thank the MOCVD-4 tool for being my constant companion during my last 5 years and making sure I got enough experiments to lead me to a PhD degree. I would like to thank Dr. Tom Mates for all the help with SIMS measurements and calibrations without which none of the experiments could be designed for this work. I would also like to thank Mark Cornish for training me on the AFM tool when I started at UCSB in 2017. I also thank Prof. Michael Spencer, my advisor during my undergraduate studies, for being a constant pillar of support, and introducing me to the beautiful world of semiconductor electronics.

Coming to the Mishra Research group, I would like to thank Dr. Haoran Li and Dr. Nirupam Hatui, who trained me on all things MOCVD, in the lab. As I'd like to think, Haoran taught me how to do research during the PhD while Niru taught me how to enjoy the PhD student life. I would also like to thank Aditya Raj for being a wonderful colleague on the ASCENT p-GaN project from the start to finish, and processing all the devices mentioned in this work. I thank all the past members of the Mishra group – Islam Sayed, Chirag Gupta, Shubhra Pasayat, Anchal Agarwal, Elaheh Ahmadi, Silvia Chan, Steven Weinecke, Cory Lund, Maher Tahhan, Onur Koksaldi, Christian Robertson and Xun Zheng, and the present ones – Pawana Shreshtha, Brian Romanczyk, Matt Guidry, Weiyi Li, Wenjian Liu, Christian Wurm, Christopher Clymore, Emmanuel Kayede, Henry Collins, Emre Akso and Boyu, for their contributions to my work and the memorable conversations.

I would like to thank the Beyond Academia organizing committees from 2019 – 2021, who gave me an opportunity to lead and put up a successful university-wide professional conference for graduate students. I had the honor of serving as the Programming Committee Chair, and the Conference Chair during my two years of involvement, and that in essence helped me chalk out my future career path.

I would also like to thank Dr. Shawn Warner-Garcia, Ashley Rifkin, Hannah Lawrence, and Dr. Baron Haber, and my GSRC colleagues, who made my time as the International Peer Advisor, extremely productive and worthwhile. I thank Dave Adornetto, the director of the New Venture Competition at UCSB, for giving me an opportunity to explore my entrepreneurial endeavors and has been a great advisor on figuring out my future professional experiences.

My graduate school experience in Santa Barbara was further enriched by the friends I made over the years, and my housemates – Aditya, Mohith, Nikhil, Chinmay, Ashwini, Richika, Shruthi, Pooja, Chandana, Ganesh, Bhagya, Aarti, Shambhavi, Priya, Vani, Shannon, and many more- thank you very much for all the out-of-the-lab experiences since 2017.

I thank my friends from my undergrad years at Cornell, many of whom I had a chance to meet during my PhD. Somrita, Abhijit, Neha, Sandeep, Aravind, Nivedita, Akshay thanks for all the unforgettable vacations in Shaver Lake, and Portland, and those once-in-a-while zoom calls which help me remember those good old days up the hill.

Finally, I would like to acknowledge my funding sources: Office of Naval Research (ONR) supervised by Dr. Paul Maki, and Applications and Systems driven Center for Energy-Efficient Integrated NanoTechnologies (ASCENT) one of the six centers in JUMP, a Semiconductor Research Corporation (SRC) program sponsored by DARPA.

CURRICULUM VITAE
Athith Krishna

April 2022

EDUCATION

Ph.D. **University of California, Santa Barbara, CA** 2022
Electrical and Computer Engineering
Title: *Investigation of p-type GaN / AlGaN superlattices: Defining a pathway towards low sheet resistance for p-channel III-nitride devices*

M.S. **University of California, Santa Barbara, CA** 2020
Electrical and Computer Engineering
Specialization: Electronics and Photonics

B.S. **Cornell University, Ithaca, NY** 2017
Electrical and Computer Engineering (*summa-cum-laude*)
(Minors: International Relations; Archeology)

PROFESSIONAL EXPERIENCE

Bain & Company, Seattle, WA July 2022 – present
- Management Consultant

University of California, Santa Barbara, CA June 2021 – June 2022
Graduate Division & Graduate Student Resource Center
- International Graduate Student Advisor

Tesserol Inc., Goleta, CA Sept. 2020 – Dec. 2021
- Co-Founder

University of California, Santa Barbara, CA
Department of Electrical and Computer Engineering
- Graduate Student Researcher Aug. 2017 – June. 2022

Advisor: Prof. Umesh Mishra
MOCVD Growth of p-type III-nitride materials for next-generation electronics

- Teaching Assistant Jan. 2020 – June 2021

ECE 221A, ECE 221B (Instructor: Prof. Umesh Mishra)

Graduate level advanced course series on semiconductor electronic devices

- Course Grader — Jan. 2020 – June 2020

ECE 211A (Instructor: Prof. Jon Schuller)
Graduate level course on Quantum Mechanics for engineers

- Lead Teaching Assistant — Aug. 2019 – Dec 2019

ECE 134 (Instructor: Prof. Robert York)
Upper-level undergraduate core course on Electromagnetic theory

Cornell University, Ithaca, NY
School of Electrical and Computer Engineering

- Undergraduate Researcher — Dec. 2014 – May 2017

Advisor: Prof. Michael G Spencer
Fabrication and Electronic Characterization of Ultra-Wide Bandgap BN devices

- Teaching Assistant — Dec. 2016 – May 2017

ECE 4370 (Instructors: Dr. Carl Poitras, Prof. Clifford Pollock)
Upper-level Undergraduate & graduate design course on Advanced Photonics

- Grader — Jan. 2016 – Dec. 2016

ECE 2100 (Instructors: Prof. Richard Shealy, Prof. Clifford Pollock)
Introductory course on Electrical Circuit Design

- Teaching Assistant — Aug. 2014 – May 2015

PHYS 2213 (Instructors: Prof. Robert Thorne, Prof. Tomas Arias)
Sophomore-level course on Electromagnetic Theory for engineers

University of Illinois, Chicago, IL
Department of Electrical and Computer Engineering

- Undergraduate Summer Researcher — May 2016 – Aug. 2016

Advisor: Prof. Junxia (Lucy) Shi
Fabrication and Electronic Characterization of 2D MOS_2 devices for sensing

Lightning Hybrids LLC., Loveland, CO
(Now Lightning eMotors)

- Controls Engineering Co-Op — Aug. 2015 – Dec. 2015

Development of Vehicle to Hybrid system communication interface

PUBLICATIONS (Journal & Conferences)

1. **Krishna, A.**; Raj, A.; Hatui, N.; Keller, S.; Denbaars, S.; Mishra, U. K. "Acceptor Traps as the Source of Holes in P-Type N-Polar GaN/(AlN/AlGaN) Superlattices". *Appl. Phys. Lett.* **2022**, *120* (13), 132104. https://doi.org/10.1063/5.0083790.

2. **Krishna, A.**; Raj, A.; Hatui, N.; Sayed, I.; Keller, S.; Mishra, U. K. "Proposed Existence of Acceptor-like Traps at Positive Polarization Interfaces in p-Type III-Nitride Semiconductors". *Appl. Phys. Lett.* **2020**, *117* (4), 042104. https://doi.org/10.1063/5.0015290.

3. **Krishna, A.**; Raj, A.; Hatui, N.; Koksaldi, O.; Jang, R.; Keller, S.; Mishra, U. K. "AlGaN/GaN Superlattice-Based P-Type Field-Effect Transistor with Tetramethylammonium Hydroxide Treatment". *Phys. Status Solidi A* **2020**, *217* (7), 1900692. https://doi.org/10.1002/pssa.201900692.

4. **Krishna, A.**; Raj, A.; Hatui, N.; Keller, S.; Mishra, U. K. "Investigation of Nitrogen Polar P-Type Doped GaN/$Al_xGa_{(1-x)}N$ Superlattices for Applications in Wide-Bandgap p-Type Field Effect Transistors". *Appl. Phys. Lett.* **2019**, *115* (17), 172105. https://doi.org/10.1063/1.5124326.

5. **Krishna, A.**; Raj, A.; Hatui, N.; Keller, S.; Mishra, U. K. "Demonstration of acceptor-like traps at positive polarization interfaces in Ga-polar p-type (AlGaN/AlN)/GaN superlattices". *Crystals.* **2022**, (in preparation)

6. Chatzakis, I.; **Krishna, A.**; Culbertson, J.; Sharac, N.; Giles, A. J.; Spencer, M. G.; Caldwell, J. D. "Strong Confinement of Optical Fields Using Localized Surface Phonon Polaritons in Cubic Boron Nitride". *Opt. Lett.* **2018**, *43* (9), 2177. https://doi.org/10.1364/OL.43.002177.

7. Clymore, C. J.; Mohanty, S.; Jian, Z. (Ashley); **Krishna, A.**; Keller, S.; Ahmadi, E. "HfO_2 as Gate Insulator on N-Polar GaN-AlGaN Heterostructures". *Semicond. Sci. Technol.* **2021**. https://doi.org/10.1088/1361-6641/abe21c.

8. Hatui, N.; **Krishna, A.**; Li, H.; Gupta, C.; Romanczyk, B.; Acker-James, D.; Ahmadi, E.; Keller, S.; Mishra, U. K. "Ultra-High Silicon Doped N-Polar GaN Contact Layers Grown by Metal-Organic Chemical Vapor Deposition". *Semicond. Sci. Technol.* **2020**, *35* (9), 095002. https://doi.org/10.1088/1361-6641/ab9727.

9. Hatui, N.; **Krishna, A.**; Pasayat, S. S.; Keller, S.; Mishra, U. K. "Metal Organic Vapor Phase Epitaxy of Thick N-Polar InGaN Films". *Electronics* **2021**, *10* (10), 1182. https://doi.org/10.3390/electronics10101182.

10. Raj, A.; **Krishna, A.**; Hatui, N.; Romanczyk, B.; Wurm, C.; Guidry, M.; Hamwey, R.; Pakala, N.; Keller, S.; Mishra, U. K. "GaN/AlGaN Superlattice Based E-Mode p-Channel MES-FinFET with Regrown Contacts and >50 MA/Mm on-Current". In

2021 IEEE International Electron Devices Meeting (IEDM); IEEE: San Francisco, CA, USA, 2021; p 5.4.1-5.4.4. https://doi.org/10.1109/IEDM19574.2021.9720496.

11. Raj, A.; **Krishna, A.**; Hatui, N.; Gupta, C.; Jang, R.; Keller, S.; Mishra, U. K. "Demonstration of a GaN/AlGaN Superlattice-Based p-Channel FinFET With High ON-Current". *IEEE Electron Device Lett.* **2020**, *41* (2), 220–223. https://doi.org/10.1109/LED.2019.2963428.

12. Romanczyk, B.; Li, W.; Guidry, M.; Hatui, N.; **Krishna, A.**; Wurm, C.; Keller, S.; Mishra, U. K. "N-Polar GaN-on-Sapphire Deep Recess HEMTs With High W-Band Power Density". *IEEE Electron Device Lett.* **2020**, *41* (11), 1633–1636. https://doi.org/10.1109/LED.2020.3022401.

13. Romanczyk, B.; Zheng, X.; Guidry, M.; Li, H.; Hatui, N.; Wurm, C.; **Krishna, A.**; Ahmadi, E.; Keller, S.; Mishra, U. K. "W-Band Power Performance of SiN-Passivated N-Polar GaN Deep Recess HEMTs". *IEEE Electron Device Lett.* **2020**, *41* (3), 349–352. https://doi.org/10.1109/LED.2020.2967034.

14. Sayed, I.; Liu, W.; Georgieva, J.; **Krishna, A.**; Keller, S.; Mishra, U. K. "Characterization of AlSiO Dielectrics with Varying Silicon Composition for N-Polar GaN-Based Devices". *Semicond. Sci. Technol.* **2020**, *35* (9), 095027. https://doi.org/10.1088/1361-6641/ab9ecb.

15. Shrestha, P.; Guidry, M.; Romanczyk, B.; Hatui, N.; Wurm, C.; **Krishna, A.**; Pasayat, S. S.; Karnaty, R. R.; Keller, S.; Buckwalter, J. F.; Mishra, U. K. "High Linearity and High Gain Performance of N-Polar GaN MIS-HEMT at 30 GHz". *IEEE Electron Device Lett.* **2020**, *41* (5), 681–684. https://doi.org/10.1109/LED.2020.2980841.

16. Shrestha, P.; Guidry, M.; Romanczyk, B.; Karnaty, R. R.; Hatui, N.; Wurm, C.; **Krishna, A.**; Pasayat, S. S.; Keller, S.; Buckwalter, J. F.; Mishra, U. K. "A Novel Concept Using Derivative Superposition at the Device-Level to Reduce Linearity Sensitivity to Bias in N-Polar GaN MISHEMT". In *2020 Device Research Conference (DRC)*; IEEE: Columbus, OH, USA, 2020; pp 1–2. https://doi.org/10.1109/DRC50226.2020.9135169.

17. **Krishna, A.**; Raj, A.; Hatui, N.; Keller, S.; Mishra, U. K. "Demonstration of acceptor-like traps at positive polarization interfaces in Ga-polar p-type (AlGaN/AlN)/GaN superlattices". In *2022 Compound Semiconductor Week*; Ann Arbor, MI, USA, 2022

18. Raj, A.; **Krishna, A.**; Hatui, N.; Pakala, N.; Keller, S.; Mishra, U. K. "MOCVD selective area p + GaN contact regrowth for Mg-doped GaN/AlGaN superlattice fins: towards GaN hole channel FinFETs". In *2022 Compound Semiconductor Week*; Ann Arbor, MI, USA, 2022

19. **Krishna, A.**; Raj, A.; Hatui, N.; Keller, S.; Mishra, U. K. "Properties of Nitrogen-Polar p-Type AlGaN/GaN Superlattices Grown by MOCVD". In *13th International Conference on Nitride Semiconductors*; Bellevue, WA,USA, 2019.

20. Hatui, N.; **Krishna, A.**; Li, H.; Gupta, C.; Acker-James, D.; Keller, S.; Mishra, U. K. "Ultra-High Silicon Doped Nitrogen-Polar Gallium Nitride Films Using Metal-Organic Chemical Vapor Deposition". In *International Workshop on Nitride Semiconductors 2018*; Kanazawa, Japan, 2018.

21. Raj, A.; **Krishna, A.**; Hatui, N.; Jang, R.; Keller, S.; Mishra, U. K. "Optimizing Design Space for GaN/AlGaN Superlattice Based Hole Channel FinFET Using SILVACO Simulation". In *TechCon 2020*; Virtual, 2020.

22. **Krishna, A.**; Raj, A.; Hatui, N.; Keller, S.; Mishra, U. K. "MOCVD Grown Nitrogen-Polar p-Type GaN/AlGaN Superlattices with AlN Interlayer". In *8th International Symposium on Growth of III-Nitrides (ISGN8)*; San Diego, CA, USA, 2020.

23. Chatzakis, I.; **Krishna, A.**; Giles, A. J.; Sharac, N.; Spencer, M. G.; Caldwell, J. D. "Investigation of Unpatterned Etching of Nanostructures in Immobilized Cubic-Boron Nitride for Infrared Nanophotonic Elements". In *2017 MRS Fall Meeting*; Boston , MA, USA, 2017.

24. **Krishna, A.**; Chatzakis, I.; Giles, A. J.; Sharac, N.; Spencer, M. G.; Caldwell, J. D. "Investigation of Unpatterned Etching in Immobilized Cubic-Boron Nitride for Infrared Nanophotonic Elements". In *59th Electronic Materials Conference*; South Bend, IN, USA, 2017.

25. Pasayat, S.; Agarwal, A.; Wurm, C.; **Krishna, A.**; Zheng, X.; Romanczyk, B.; Gupta, C.; Guidry, M.; Keller, S.; Mishra, U. K. "Impact of Regrowth (on Wet Etched and Dry Etched Interface) on the Breakdown Performance of N-Polar GaN MIS-HEMTs". In *International Workshop on Nitride Semiconductors 2018*; Kanazawa, Japan, 2018.

26. Calderon, B.; Ji, Y.; **Krishna, A.**; Kwak, J. Y.; Hwang, J.; Al Salman, H.; Xu, X.; Spencer, M. G. "High Mobility CVD Grown Boron Nitride Devices". In *59th Electronic Materials Conference*; South Bend, IN, USA, 2017.

27. Raj, A.; **Krishna, A.**; Hatui, N.; Keller, S.; Mishra, U. K. "GaN/AlGaN Superlattice Based p- Channel Power FinFET". In *2021 SSLEEC Annual Review*; Santa Barbara, CA, USA, 2021.

28. Raj, A.; **Krishna, A.**; Hatui, N.; Romanczyk, B.; Liu, W.; Keller, S.; Mishra, U. K. "GaN/AlGaN Superlattice Based E-Mode p-Channel MES-FinFET". In *79th Device Research Conference (DRC 2021)*; Virtual, 2021.

29. Raj, A.; **Krishna, A.**; Hatui, N.; Romanczyk, B.; Liu, W.; Keller, S.; Mishra, U. K. "GaN/AlGaN Superlattice Based E-Mode Hole Channel FinFET with Schottky Gate". *IEEE Electron Device Lett.* **2021**.

30. **Krishna, A.**; Chandrashekhar, M.; Chatzakis, I.; Caldwell, J. D.; Spencer, M. G. "Electrical and Optical Characteristics of Bulk Cubic-Boron Nitride (c-BN) Crystals". In *60th Electronic Materials Conference*; Santa Barbara, CA, USA, 2018.

31. **Krishna, A.**; Raj, A.; Hatui, N.; Keller, S.; Mishra, U. K. "Effect of Acceptor Traps at Positive Polarization Interfaces on the Charge and Mobility of Holes in N-Polar p-Type GaN/(AlN/AlGaN) Superlattices". In *63rd Electronic Materials Conference*; Virtual, 2021.

32. **Krishna, A.**; Raj, A.; Hatui, N.; Koksaldi, O.; Romanczyk, B.; Keller, S.; Mishra, U. K. "Development of P-Type AlGaN/GaN Superlattice Field Effect Transistor". In *International Workshop on Nitride Semiconductors 2018*; Kanazawa, Japan, 2018.

33. **Krishna, A.**; Raj, A.; Hatui, N.; Keller, S.; Mishra, U. K. "Acceptor Traps as Sources of Holes in P-GaN/(AlN/AlGaN) Superlattices". In *2021 SSLEEC Annual Review*; Santa Barbara, CA, USA, 2021.

34. Ji, Y.; Calderon, B.; Kwak, J. Y.; **Krishna, A.**; Hwang, J.; AlSalman, H.; Xu, X.; Spencer, M. G. "Chemical Vapor Deposition Growth of Large Single-Crystal Monolayer and Bilayer Hexagonal Boron Nitride". In *59th Electronic Materials Conference*; South Bend, IN, USA, 2017.

Awards

UCSB Academic Senate Doctoral Student Travel Grant – 2022

Walsin Lihwa Family Fellowship - 2019

Qualcomm Innovation Fellowship – North America Finalist – 2019

Cornell University – Tata Scholarship – Class of 2017

Proctor & Gamble – Technical Excellence Award 2016

Academic Excellence Award – Cornell University Diversity Programs in Engineering 2017

ABSTRACT

Investigation of p-type GaN / AlGaN superlattices: Defining a pathway towards low sheet resistance for p-channel III-nitride devices

by

Athith Krishna

Post the commercialization and widespread use in light emitting diodes (LEDs), heterostructures of III-nitride semiconductors (GaN, AlN, InN, and BN) with their alloys, have shown immense promise in applications not limited to optoelectronics, but ranging from high power and high frequency electronics to plasmonics, sensor technology and quantum computing. While the superior properties of electrons and the two-dimensional electron gas (2DEG) have peaked a great deal of attention on this materials system, similar levels of advancements in p-type III-nitrides are required to tap into the complete benefits this semiconductor family can potentially provide. Like in most other wide-bandgap materials, the poor performance of p-type material in III-nitrides has led to only a few studies reported on p-channel III-nitride electronic devices. The use of p-type superlattice (SL) is valuable for III-nitride semiconductor-based p-channel Field effect transistors (pFETs) and LEDs because the polarization effects create a periodic oscillation of the energy bands, enhancing the ionization of the deep acceptors. Thus, the use of Mg-doped GaN/AlGaN SL is a pathway to get high hole concentration and mobility simultaneously,

and pFETs engineered around a GaN/AlGaN SL have demonstrated record electrical performance.

The present study will systematically explore the electrical properties of epitaxially grown p-type Ga-polar and N-polar, modulation doped and uniformly doped GaN/AlGaN, and GaN/AlN/AlGaN superlattices (grown using the MOCVD growth technique). Following this, the discovery of a novel acceptor trap, proposed at 0.8 eV above the valence band of GaN, will be presented with simulations and experiments. The implications of this trap level, and its impact as the source of holes in dopant-deficient systems will be elucidated. This study will also explain in detail how charge balance is achieved in recent p-channel III-nitride electronic and optoelectronic devices. A detailed methodology will also be presented to predict and explain the mobility and high sheet concentration of holes in p-type III-nitride systems. p-type III-nitride material with record sheet resistance as low as 1.5 kΩ/sq will be shown. This work concludes with the development of highly doped p-GaN regrowth for use in p-channel III-nitride FETs with record normally-off performance.

TABLE OF CONTENTS

LIST OF FIGURES

LIST OF TABLES

Chapter 1

Introduction

A. III-nitride semiconductor family

III-nitride (GaN, AlN, InN, BN) heterostructures and their alloys are at the forefront of fulfilling the needs of next generation power conversion technology, and communication systems – enabling a compact, affordable and energy efficient future for all humanity. In addition to its widespread use in state-of-the-art light emitting diodes (LEDs) [1,2] and laser diodes (LDs) [3,4], this semiconductor family is leading the way by replacing conventional semiconductors in high power [5-8] and RF electronics [9-12] and has more recently shown immense promise for use in solar cells and thermoelectric generators [13,14], novel spintronic and nuclear detection devices [15], plasmonics [16,17], and quantum computing systems [18,19]. Following are the reasons for the attractiveness of this materials system:

(a) Polarization fields enable multiple applications within the same material: The large magnitude of spontaneous and piezoelectric polarization fields in III-nitrides [20], and their variation across the different crystal orientations, have provided a valuable tool to engineer electronic properties (charge distributions and energy bands) of this semiconductor family based on the applications. As summarized in Figure 1.1: (i) the more conventional Ga-Polar

orientation (crystal is grown along the c-plane {0001}), is widely used in LEDs, LDs, and High Electron Mobility Transistors (HEMTs) [21,22]; (ii) III-nitride heterostructures grown in the N-Polar orientation (crystal grown along the -c plane $\{000\bar{1}\}$) have shown record device performance in high power and RF regime [23-25]; (iii) it is observed that the polarization fields do not exist along the major axes in the c-plane, so when the crystal is grown along the a-plane $\{11\bar{2}0\}$, Non-polar III-nitrides are obtained, and these are valuable in light emitters without Stokes shift, and Fin technologies in transistors [26,27]; and (iv) non-polar material is also obtained by growing the III-nitride crystal along the m-plane $\{10\bar{1}0\}$ and these are used in novel LD technologies [28,29].

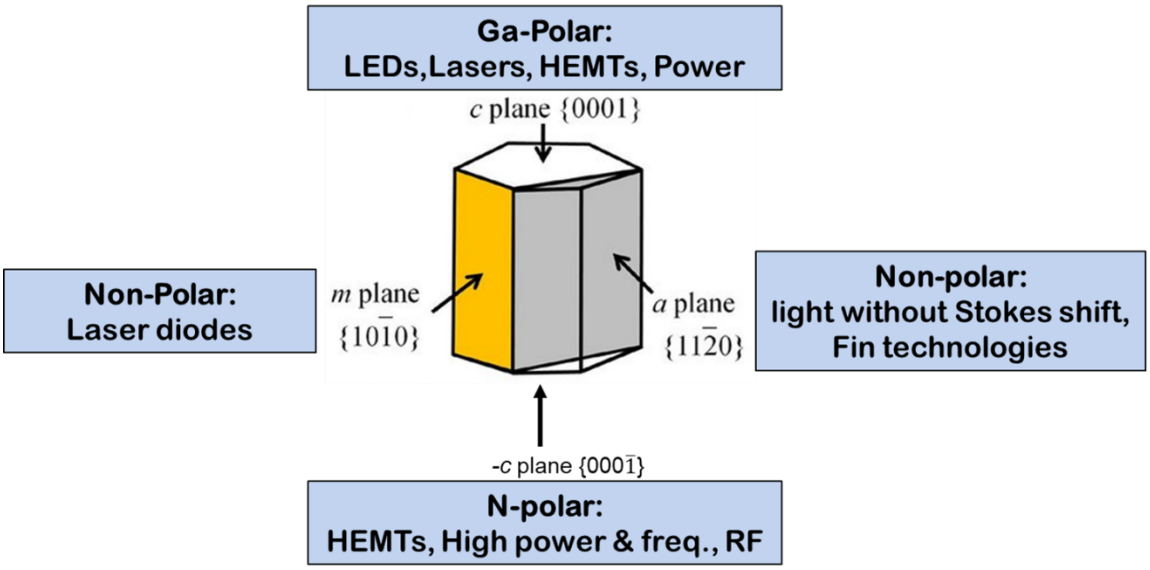

Figure 1.1 III-nitride Wurtzite semiconductor crystal indicating the different polarities when the crystal orientation is varied, with an application for each of those polarities.

(b) Tunability across a wide band gap range: As shown in Figure 1.2, III-nitrides, and their alloys (ternary and quaternary) can be tuned over an extremely wide bandgap range – 0.7eV (InN) to 6.2eV (AlN) − within the same material family [30]. This allows their

application in light emitters over a large wavelength all the way from infrared (IR) to ultraviolet (UV) [31-33].

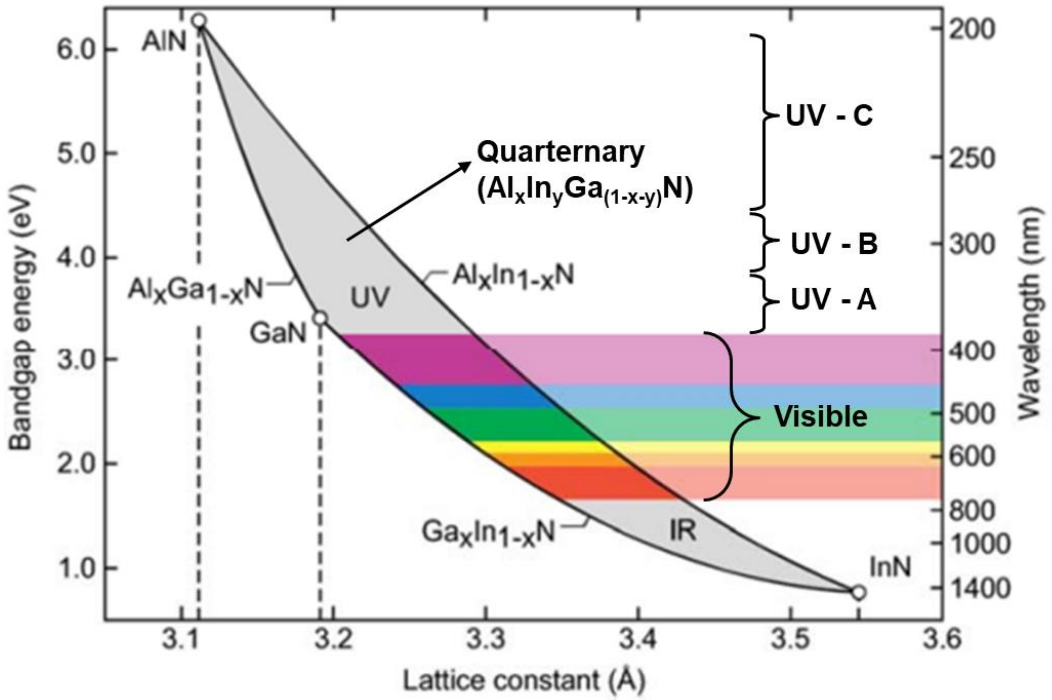

Figure 1.2 Room temperature Bandgap energy (in eV) as a function of the lattice constant for the III-nitride semiconductors (and their alloys). The y-axis on the right indicates the wavelength of light emission for the corresponding bandgap energy[30].

(c) Well established epitaxial growth techniques: Epitaxial growth refers to the growth of thin-films of semiconductor over a substrate (crystalline), replicating the group symmetry of the substrate in the grown epitaxial layer. Extremely complicated III-nitride heterostructures (referring to ranges of precise thickness and compositions) are required to realize state-of-the-art sophisticated electronic and optoelectronic devices. While there are various established epitaxial growth methods, two of the more widely used are Molecular Beam Epitaxy (MBE) and Metal-Organic Vapor Phase Epitaxy (MOVPE). All the studies reported in this dissertation are grown using MOVPE technique.

Moreover, the exceptional fundamental properties of electrons in III-nitrides have enabled the widespread use of these materials for reliable high power and high frequency electronics. In AlGaN/GaN heterostructures, the discontinuity in polarization leads to the formation of a two-dimensional electron gas (2DEG) with a very high electron mobility ($\mu \geq$ 1500 cm^2/Vs) and sheet charge density ($n_s \sim 10^{13}$ cm^{-2}) – and these 2DEGs have applications as channel layers in HEMTs [34]. In addition to this, Figure 1.3 details how the properties of electrons in the III-nitrides lead to improved performance in power electronic devices [35].

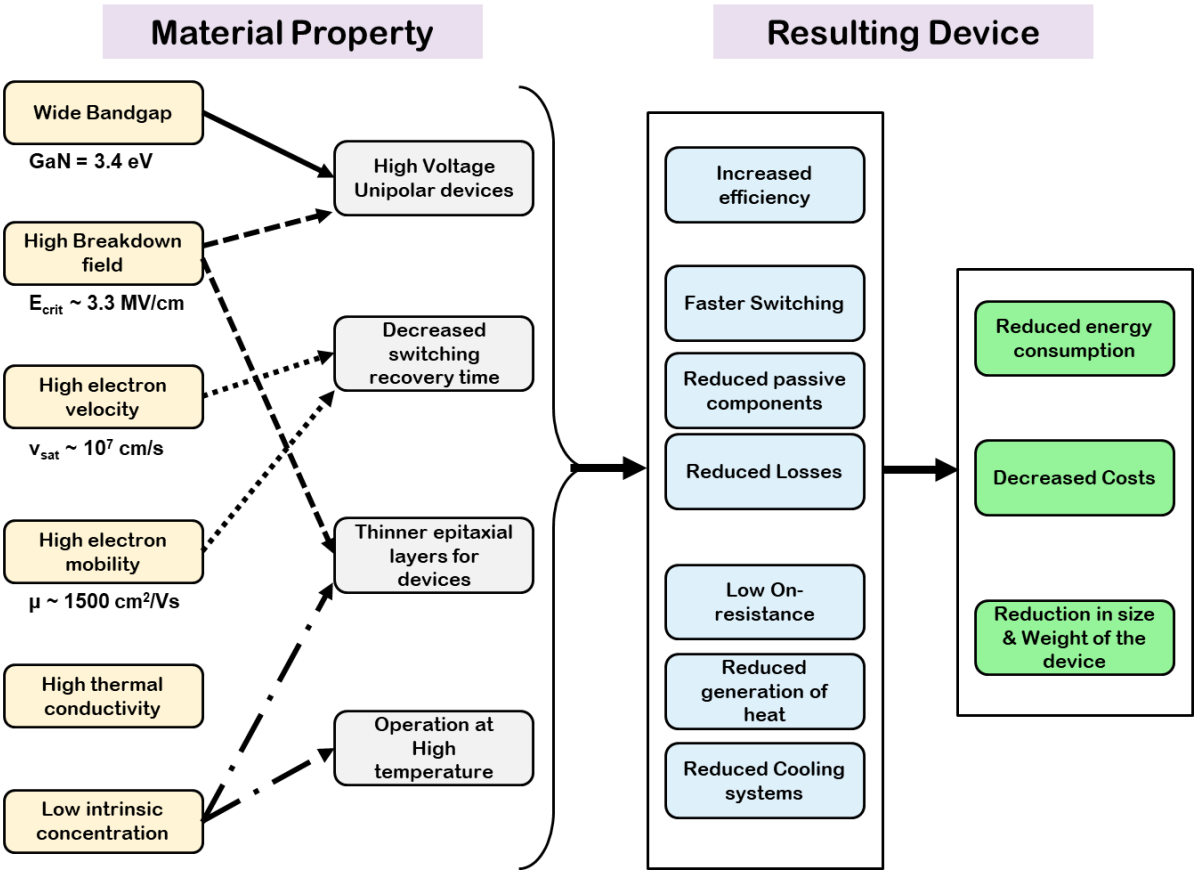

Figure 1.3 Summary of the material properties of GaN and the resulting device characteristics highlighting the advantages of this materials system for reliable use in n-type transistors for high power and high frequency applications.

All is good with the electrons and the n-type III-nitrides. But, what about holes and the p-type material?

B. p-type doped III-nitrides

To tap into the full potential of the III-nitride material system, the fabrication of p-type GaN based devices is desired. Early developments in the p-type doping of GaN, and the consequent methodologies towards its understanding, have played a major role in fast-tracking the development of III-nitride research in recent years. As can be seen in the case of LEDs in particular, the immense progress made since p-type GaN was first achieved in 1989 has already led to commercialized products that presently occupy a large share in the solid-state lighting markets [36,37]. Despite this initial success, the difficulties associated with p-type doping of GaN continue to be a major hurdle in realizing novel III-nitride device architectures – an example being III-nitride based Complementary Metal-Oxide-Semiconductor (CMOS) technology.

GaN CMOS technology is needed to realize monolithic GaN power integrated circuits (ICs) either integrating high-voltage GaN transistors with low-voltage n-channel and p-channel GaN Field effect transistors (FETs) on the same chip or using power CMOS devices directly for power conversion. The III-nitride based devices that are used in systems are at times limited by the parasitic losses arising from integrating and driving these chips using the CMOS circuitry based on silicon for complex control logic. Therefore, a CMOS integrated technology based wholly on the wide bandgap III-nitrides are desired to engineer around the parasitic losses. CMOS based on GaN has the potential to adopt Si-based CMOS topologies and can be used to realize very efficient gate drivers and high-voltage direct current DC-to-DC converters.

In addition to this, an increasing number of applications in power electronics, sensor signal conditioning, and RF communication that are desired to operate at temperatures greater than 200˚C can also benefit from GaN based CMOS. Advancements in p-GaN FETs and ultimately the GaN CMOS technology can help build high efficiency and high-speed single-stage 48V to 1V DC-DC converters.

Unfortunately, like in most wide-bandgap materials, the properties of holes in GaN have limited the implementation of p-channel devices. The main challenges with p-type GaN are the following:

(a) In the p-type III-nitride material grown using MOVPE, Mg dopants are passivated by hydrogen in the as-grown state and the sample needs annealing at a high temperature for activation of the dopants[1]. This thermal annealing step to reduce the H_2 passivation of the Mg acceptor by Nakamura, et. al., in 1992, paved the way for efficient GaN-based LEDs [38].

(b) Mg, which is the commonly preferred p-type dopant, is a deep acceptor in GaN and AlGaN (170–230 meV). This results in lower doping efficiency of Mg, and hence leads to enhanced resistance in the devices. Table 1.1 (data from Ref [39]) shows the other potential elements that could act as acceptors in GaN, along with their estimated binding energy.

Table 1.1 Possible acceptor dopants in GaN along with their binding/activation energies. [Ref 39]

Dopant	ΔE_A
Mg	170 – 230 meV
Zn	340 meV
Be	210 – 700 meV
Hg	410 meV
Cd	550 meV

[1] p-type III-nitrides grown using MBE technique do not suffer from this issue as they are grown in hydrogen-free environments.

Li	750 meV
C	860 meV

(c) The high effective mass of holes in GaN results in a very low hole mobility (μ), with the maximum observed value being 43 cm^2/Vs at a low hole concentration of 2×10^{12} cm^{-2} (sheet resistance, R_{sh} ~90 kΩ/sq) in a two-dimensional hole gas (2DHG), and μ ~ 20 cm^2/Vs reported in bulk GaN with hole concentration of 1×10^{17} cm^{-3} [40,41].

(d) The high p-GaN work function at typical doping levels results in challenges to making good ohmic contacts to p-type GaN [42].

All of these factors lead to reduction in On-current (I_{on}), switching frequencies and current modulation (I_{on}/I_{off}), and hence device performance in p-channel FETs (pFETs). In view of these challenges, III-nitride-based pFETs have received significantly less attention compared with GaN-HEMTs. Following are some of the pFET efforts demonstrated:

(a) **Effort:** University of South Carolina (M. Shatalov et.al) - 2002 [43]

Platform: AlGaN/GaN

[Normally-on device] I_{on}: 4 mA/mm; $I_{on}/I_{off} = 10^2$

(b) **Effort:** University of Notredame (G. Li et.al) - 2013 [44]

Platform: p-/uid (unintentionally doped)-GaN/AlN/ Al_2O_3 MOS Gate

[Normally-on device] I_{on}: 100 mA/mm;

[Normally-off device] I_{on}: 3.87 mA/mm; $I_{on}/I_{off} = 10^3$

(c) **Effort:** RWTH, Aachen (H. Hahn, B. Reuters et.al) - 2014 [45,46]

Platform: p-/uid-GaN/AlInGaN/GaN/AlN Schottky Gate

[Normally-on device] I_{on}: 40 mA/mm; $I_{on}/I_{off} = 10^4$

[Normally-off device] I_{on}: 10 mA/mm; $I_{on}/I_{off} = 10^6$

(d) **Effort:** Hughes Research Labs (R. Chu et.al) - 2016 [47]

Platform: p-/uid-GaN/AlGaN/GaN/AlN/SiN_x MIS Gate

[Normally-off device] I_{on}: 1.5 mA/mm; $I_{on}/I_{off} = 10^6$

(e) **Effort:** Cornell University (S. Bader et.al) – 2018 - Present [48-50]

Platform: AlN/GaN

[Normally-on device] I_{on}: 400 mA/mm; $I_{on}/I_{off} = 10^3$

[Normally-off device] I_{on}: 10 mA/mm; $I_{on}/I_{off} = 10^4$

(f) **Effort:** MIT (N. Chowdhury et.al) – 2019 - Present [51-53]

Platform: p-GaN/AlGaN/GaN/Al_2O_3 MOS Gate

[Normally-off device] I_{on}: 40 mA/mm; $I_{on}/I_{off} = 10^4$

[Normally-off device] I_{on}: 4 mA/mm; $I_{on}/I_{off} = 10^6$

(g) **Effort:** HKUST (Z. Zheng et.al) - 2019 [54]

Platform: p-GaN/AlGaN/GaN/Al_2O_3 MOS Gate

[Normally-off device] I_{on}: 3.38 mA/mm; $I_{on}/I_{off} = 10^7$

(h) **Effort:** UCSB (A. Raj et.al) – 2019 - Present [55,56]

Platform: p-(AlGaN/GaN) superlattice (SL) FinFET

[Normally-on device] I_{on}: 80 mA/mm; $I_{on}/I_{off} = 10^5$

[Normally-off device] I_{on}: 80 mA/mm; $I_{on}/I_{off} = 10^7$

C. Synopsis of the Dissertation

Chapter 2 of the dissertation introduces the development of the Ga-Polar Uniformly doped p-type AlGaN/GaN SL for use in III-nitride pFETs. MOVPE growth conditions are discussed in detail along with Room-Temperature (RT) Hall measurement results.

Optimization of Mg dopant activation conditions is also presented. Fabrication process flow and electrical characterization of the first p-type SL based III-nitride FET is then detailed.

Chapter 3 of the dissertation introduces the Modulation doping scheme, and the development of the N-Polar Uniformly doped p-type AlGaN/GaN SL for use in III-nitride pFETs. MOVPE growth conditions are discussed in detail along with Room-Temperature (RT) Hall measurement results. These results are benchmarked against all reported p-type III-nitride systems, and MOVPE record mobility and Rsh are presented. A test planar pFET and a FinFET are also presented in this chapter.

Chapter 4 starts with the design of N-polar modulation doped p-type GaN/AlN/AlGaN SL. RT Hall measurements are carried out to measure the total hole sheet charge and the mobility. The existence of novel acceptor-like traps at positive polarization interfaces in III-nitride systems is introduced using experimental data, and theoretical calculations using STR-FETIS and Silvaco software packages. The trends in total sheet charge and mobility are explained using these acceptor-like trap levels. Chapter 4 ends with demonstration of p-type modulation doped GaN/AlGaN SL with varying Al composition, to show the existence of acceptor traps in systems without AlN interlayers.

Chapter 5 seeks to demonstrate the universality of these acceptor traps introduced in the previous chapter. Design and MOVPE growth of Ga-polar uniformly doped p-type AlGaN/AlN/GaN SL is carried out followed by RT Hall measurements to measure the total hole sheet charge and the mobility. The trends in total sheet charge and mobility are explained using these acceptor-like trap level at positive polarization interfaces and are corroborated with theoretical calculations using STR-FETIS. The chapter ends with benchmarking of all reported 2DHG in semiconductor systems and shows how the

AlGaN/AlN/GaN SL with the acceptor-like traps helps achieve the record lowest sheet resistance (Rsh ~ 2kΩ/sq).

Chapter 6 details our efforts towards tackling the challenges to making good ohmic contacts to p-type GaN using the development of MOVPE p+ GaN selective area contact regrowth. Pre-regrowth sample treatment (ex-situ and in-situ), MOVPE growth conditions, and fabrication of TLM structures are detailed. Electrical characterization is then carried out, and the use of this p+ GaN regrowth to achieve record pFET device performance is presented.

Chapter 7 deals with potential future applications of this work using acceptor-like traps to design an epitaxial structure with the lowest R_{sh}, high sheet charge, and high mobility values for applications in pFETs.

It is important to note that the experiments and calculations described in this dissertation were not performed in the order in which they are presented—instead the flow of the content presented has been chosen for maximum clarity. For example, the development of p+ regrowth of ohmic contacts presented in Chapter 6 were carried out in parallel with the work presented in Chapters 4. But, since it tackles a different issue related to the holes in III-nitrides, it has been presented as a separate chapter after the discussions related to achieving the lowest p-type R_{sh}.

Chapter 2

Ga-Polar p-type Uniformly Doped AlGaN/GaN Superlattice

A. Incentive for the use of SL

Previously mentioned in Chapter 1, one of the main challenges that has hindered the development p-type III-nitride devices is the deep nature of suitable acceptor dopants, here Mg, which leads to low concentration of holes in the bulk III-nitride material. Low temperature (and even room temperature) operation of bulk p-type III-nitrides are difficult due to the temperature dependence of these holes. Deep acceptors lead to low doping efficiency, and this is another major issue that needs to be tackled in this case. In view of these challenges, III-nitride-based pFETs have received significantly less attention compared with GaN-based high electron mobility transistors. Following the work by Peter Kozodoy et. al., at UC Santa Barbara [57-61], from 1999, in this report, we present the development of Ga-polar uniformly p-type doped AlGaN/GaN SL, and the first p-type GaN/AlGaN superlattice (SL) pFET.

As reported in the AlGaN/GaN p-MOS [62], the on-resistance (R_{ON}) of the device can be modeled according to Equation (1):

$$R_{ON} = (2 \times R_{contact}) + R_{channel} + R_{access\text{-}source} + R_{access\text{-}drain} \qquad Eq(1)$$

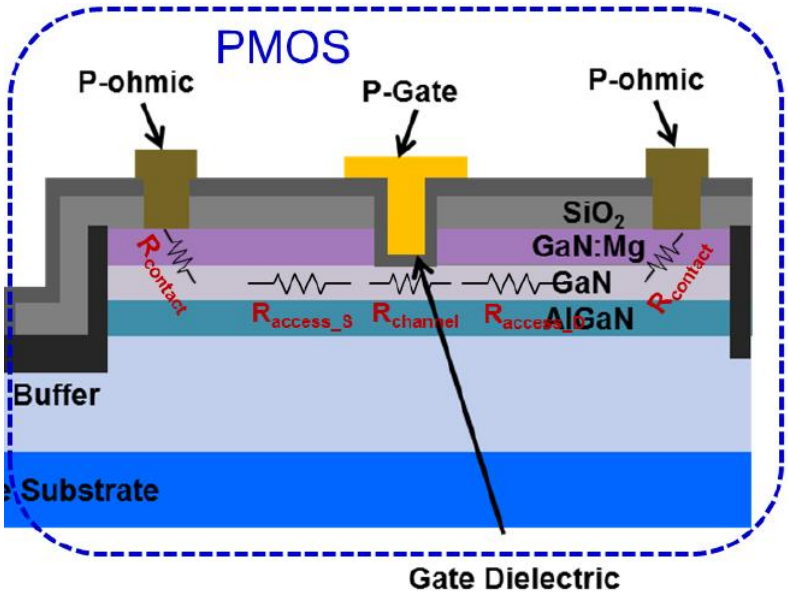

Figure 2.1 Reported pMOS from Ref. 62, with all the components of the on-resistance indicated.

Figure 2.1 can help visualize the placement of these resistances. Depending on the design of the device structure, the use of AlGaN/GaN SL can help reduce the R_{access} of the device. Application of periodic oscillations to the valence band edge can help increase the doping efficiency of acceptors in p-type III-nitride materials. With polarization effects aiding the process, SLs lead to the necessary valence band edge oscillations. As demonstrated by Kozodoy et al., (reproduced in Figure 2.2) the use of AlGaN/GaN SLs leads to an increased overall hole concentration as it facilitates the ionization of deep acceptors in the barriers into the valence band of the narrower bandgap material (here, GaN). SLs also give rise to 2DHG formation at the GaN/AlGaN interfaces, thus leading to improved mobility values in the channel and reduced resistances ($\mu_{2DHG} > \mu_{Bulk}$ for holes).

While the advantages of the SL layout are best utilized in FinFETs, where the trigate allows the modulation of each of the parallel p-channels, in this Chapter, planar recess gate pFETs with a single channel are investigated to develop the first process modules.

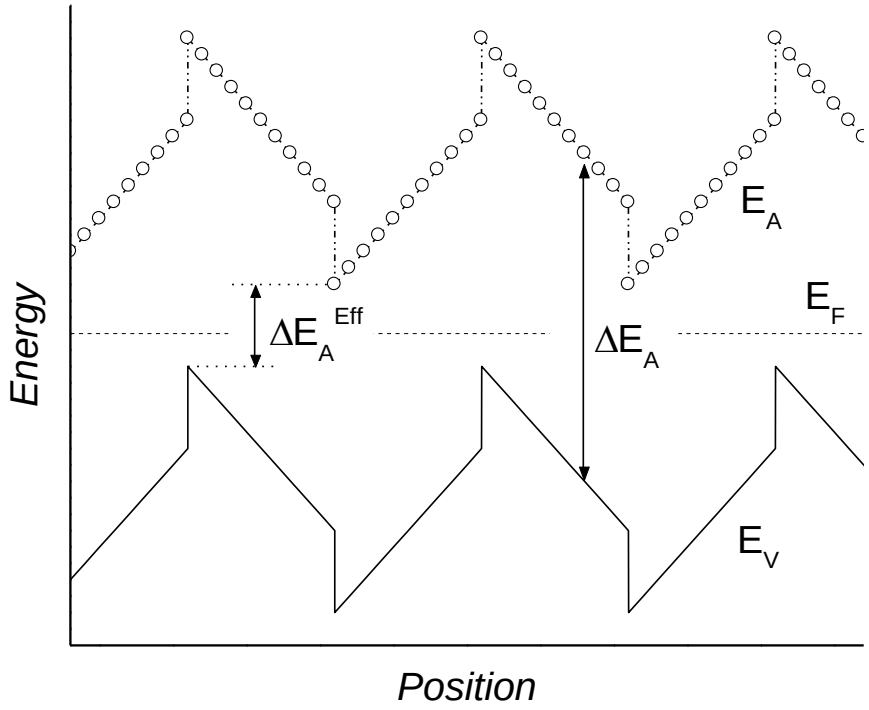

Figure 2.2 Schematic diagram of effective acceptor activation energy reduction through polarization effects in AlGaN/GaN superlattices. The solid line represents the valence band edge, the open circles represent the acceptor energy. The dashed line is the Fermi energy. [Modified from Ref. 60]

B. Epitaxial Design, MOVPE Growth & Material Characterization

Metalorganic Vapor Phase epitaxy (MOVPE) is one of the more popular techniques for epitaxial growth of III-nitride semiconductors or deposition of thin films in both academic, and industrial settings. In MOVPE, metalorganic precursors and their associated carrier gases are used to transport the vapors of liquid and solid sources into the reaction chamber. Hydrides containing nitrogen are used for nitrides (in this case, ammonia), and they react on the surface of the heated substrate where the thin film growth occurs. For group-III element,

the commonly used precursors include trimethylaluminium (TMAl), trimethylgallium (TMGa), triethylgallium (TEGa), trimethylindium (TMIn) etc. The usual growth (substrate) temperature for III-nitride thin films ranges from 1160°C to 800°C. The common n-type dopant source is a Si-containing hydride gas like disilane and p-type dopant source is metalorganic bis-(cyclopentadienyl) magnesium (Cp_2Mg). Optoelectronic and electronic devices made from III-nitrides have multiple layers of nitrides (GaN, AlN, InN) and their alloys, and as such have different amount of strain. Choice of substrate is an important consideration since GaN substrates are expensive, and other foreign substrates of choice are cheaper, and have larger lattice mismatch like SiC, sapphire (13.9%) and Si [63]. This hetero epitaxy is highly sensitive to strain, one-dimensional (dislocations) and two-dimensional (stacking faults, anti-phase boundaries, etc.) defects, and unintentionally induced impurities.

Extensive studies on growth mechanisms of {0001}-oriented or Metal polar III-nitrides layers have been performed previously as they have a relatively large growth window (pressure, temperature, precursor flow) compared to other N-polar, semi-polar and non-polar orientations of GaN. Because of better (wider) growth window, {0001}-GaN is still the preferred orientation of growth [64]. But, as mentioned in Chapter 1, {0001}-oriented GaN (and other III-nitrides with their alloys) has large piezoelectric strain and associated internal electric field which can play a detrimental role in reducing radiative efficiency, and consequently the performance of optoelectronic devices.

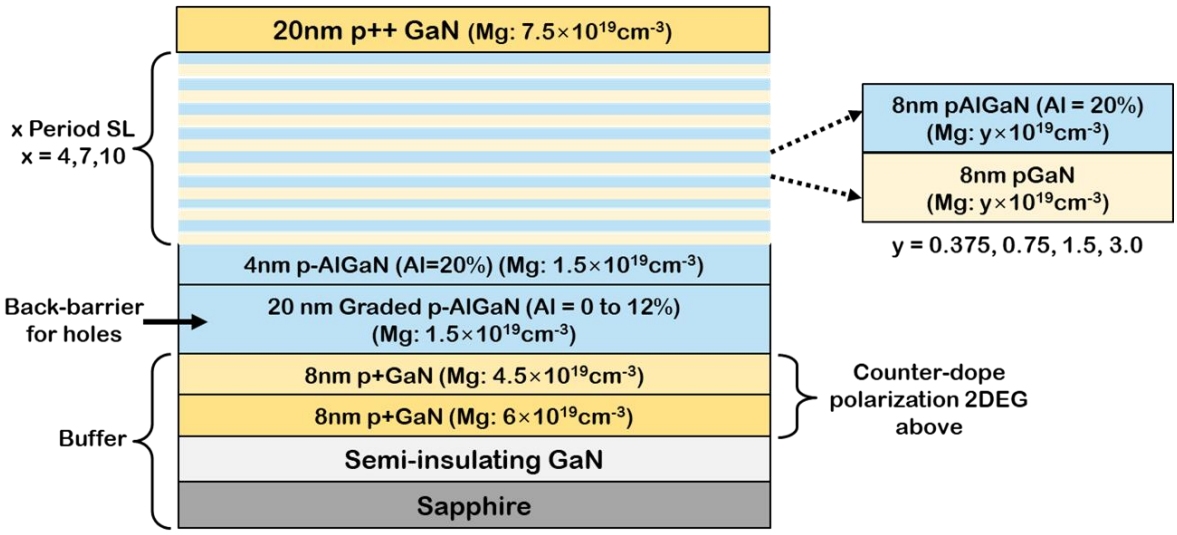

Figure 2.3 Design of the epitaxial structure for the SL p-(GaN/AlGaN) FET. SL series with 4,7, and 10 SL periods was grown. Mg doping series was also grown for 7-SL samples with Mg = 3.75 × 10^{18} cm^{-3}, 7.5 × 10^{18} cm^{-3}, 1.5 × 10^{19} cm^{-3} and 3.0 × 10^{19} cm^{-3}.

Figure 2.3 shows the p-(GaN/AlGaN) SL epitaxial structure reported in this chapter. The MOVPE epitaxial growth technique was used to grow the epitaxial structures on c-plane sapphire substrates at a temperature of 1155˚C and pressure of 100 torr. First, 1.5 μm of semi-insulating GaN was deposited, followed by 16 nm of uniformly doped p-type GaN:Mg with 8nm of [Mg] = 6 × 10^{19} cm^{-3} and 8nm of [Mg] = 4.5 × 10^{19} cm^{-3}. This layer was used to counter dope the polarization-related 2DEG formed during $Al_xGa_{(1-x)}N$ deposition. Moreover, 20 nm $Al_xGa_{(1-x)}N$:Mg was grown where the composition was graded from x = 0 to 12% followed by 4 nm $Al_{0.2}Ga_{0.8}N$ to be used as the back barrier for hole transport. The next layers consisted of the SL stack with 4, 7, and 10 SL periods of 8 nm p-GaN/8 nm p-$Al_{0.2}Ga_{0.8}N$ uniformly doped with 1.5 × 10^{19} cm^{-3} of Mg. Finally, a 20 nm p-GaN cap was grown, which was doped with 7.5 × 10^{19} cm^{-3} of Mg, to act as the contact layer. For the 7-period SL sample, a Mg doping series was also grown with Mg doping = 3.75 × 10^{18} cm^{-3}, 7.5 × 10^{18} cm^{-3}, 1.5 × 10^{19} cm^{-3} and 3.0 × 10^{19} cm^{-3}. Figure 2.4 shows a representative

valence band energy diagram for a grown structure and provides a visualization for the 2DHG formation and where the charges exist in the grown structure.

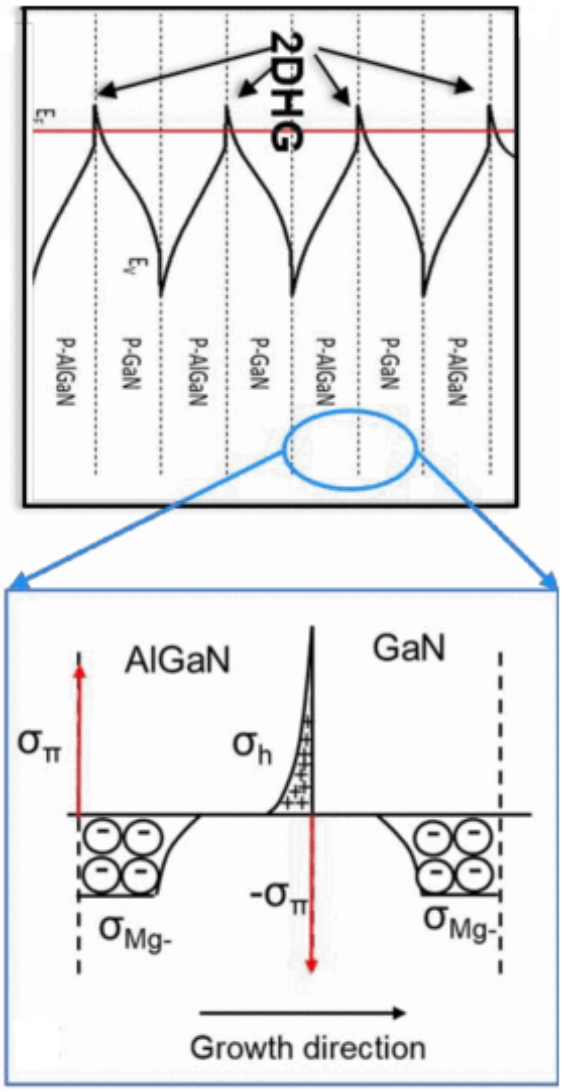

Figure 2.4 Representative valence band energy diagram for an AlGaN/GaN SL with the visualization of the 2DHG and charges in the structure

Mg doping in the individual layers was determined via secondary ion mass spectroscopy (SIMS) performed on GaN:Mg SIMS calibration samples (SIMS measurements and analysis were carried out with the help of Dr. Tom Mates). Details of the SIMS structures used to calibrate the Mg doping are provided in the Appendix. The as-grown material was characterized using X-ray diffraction (XRD) and atomic force microscopy (AFM). The

XRD ω-2θ scans showed distinct SL fringes indicating good layer periodicity, as shown in Figure 2.5, displaying the scan of a representative 7-period AlGaN/GaN SL sample with doping of 1.5×10^{19} cm^{-3} in the SL. An AFM image of the same sample is shown as an inset, and this exhibits good morphology with a rms (root mean square) roughness of ~ 0.2nm.

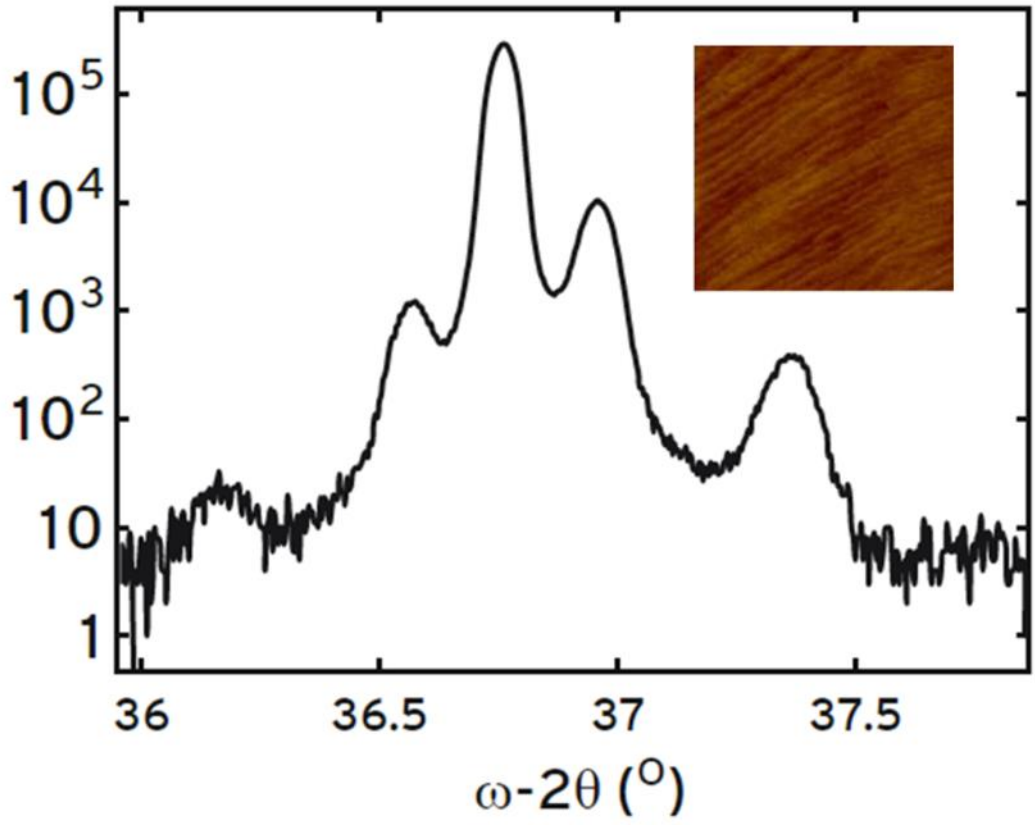

Figure 2.5 XRD (ω-2θ) scan of a 7-period p-type uniformly doped AlGaN/GaN SL sample. Inset: 2 µm × 2 µm AFM scan of the sample with z range~ 2 nm and rms roughness of 0.2nm [65].

C. Room temperature Hall-effect measurements

The electrical properties of the planar samples were investigated by room temperature Hall effect measurements (RT-Hall) and transmission line measurements (TLMs). The latter were conducted with device isolation.

As Mg acceptors were passivated in the as-grown material, optimization of the post-growth activation annealing was first conducted. 100 nm SiO_2 was deposited using plasma enhanced chemical vapor deposition (PECVD) on the as-grown samples to protect their surface. A 3 min rapid thermal annealing (RTA) was carried out for Mg dopant activation at temperatures in the range of 675 ℃ to 900 ℃ in nitrogen and nitrogen/oxygen ambient. Figure 2.6 shows the sheet resistance as a function of activation temperature. The optimum activation temperature was found to be 825 ℃ and was used for all the samples processed and reported in this work.

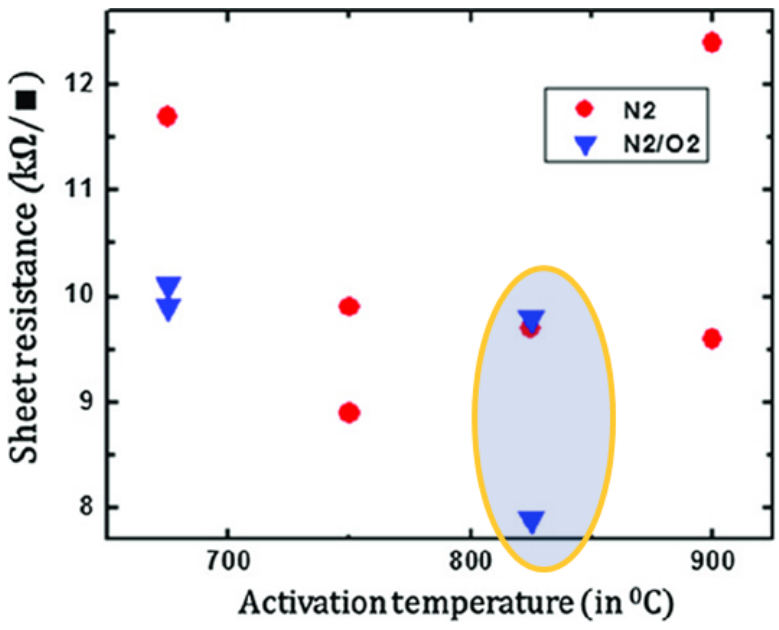

Figure 2.6 Sheet resistance as a function of activation temperature from the TLMs on non - isolated device samples.

Pd-Au metal stack contacts were deposited on the samples and prepared for RT Hall measurements. Four-probe RT-Hall measurements were carried out (with the magnetic field strengths ranging from -6T to 6T) and the total sheet charge, and mobility were measured for each of the samples. Two series were classified for the measurements: (a) superlattice period series of 4, 7 and 10 SL, with a uniform Mg doping of 1.5×10^{19} cm^{-3}, and (b) Mg doping series for a 7-period SL with Mg doping varied from 3.75×10^{18} cm^{-3}, to 3.0×10^{19} cm^{-3}.

(a) Superlattice Period series: Holding the Mg doping constant at 1.5×10^{19} cm^{-3}, Figure 2.7 shows the measured total sheet charge concentration (p_s) and mobility as a function of the number of superlattice periods of 4, 7 and 10 p-type uniformly doped AlGaN/GaN SL.

    Measured hole mobility (μ_p) remains steady as the SL periods are varied, as expected. p_s increases linearly from 4 to 7 SL periods, but we do not observe the increase when going from 7 to 10 SL periods. This is because of the RT-Hall measurements carried out as the contacts are only deposited on top of the structure, and we are not making contacts to all the 10 SL channels in the sample. Therefore, for all further measurements, we went ahead with 7 SL samples as reliable RT-Hall measurements could be carried out.

(b) Mg doping series: Holding the SL period constant at 7 periods, Figure 2.8 shows the measured total sheet charge concentration (p_s) and mobility as a function of the Mg doping in the sample - 3.75×10^{18} cm^{-3}, 7.5×10^{18} cm^{-3}, 1.5×10^{19} cm^{-3} and 3.0×10^{19} cm^{-3} .

While the measured hole mobility (μ_p) remained steady until Mg: 1.5×10^{19} cm^{-3}, it decreased for the highest Mg doping (Mg: 3.0×10^{19} cm^{-3}) – possibly due to the formation of clusters at very high Mg doping.

Figure 2.9 shows the sheet resistance of the same samples determined using the TLMs. The data confirm the observation of the Hall measurements, and the sheet resistance increased as Mg doping was raised. The lowest sheet resistance of 11.6 kΩ/sq was obtained for the samples with the lowest Mg doping of 1.5×10^{19} cm^{-3} in the SL. The best sample had a MOVPE hole μ of ~ 10 cm^2/Vs in uniformly doped Ga-polar p-type SL with a sheet charge of ~ 6×10^{13} cm^{-2}.

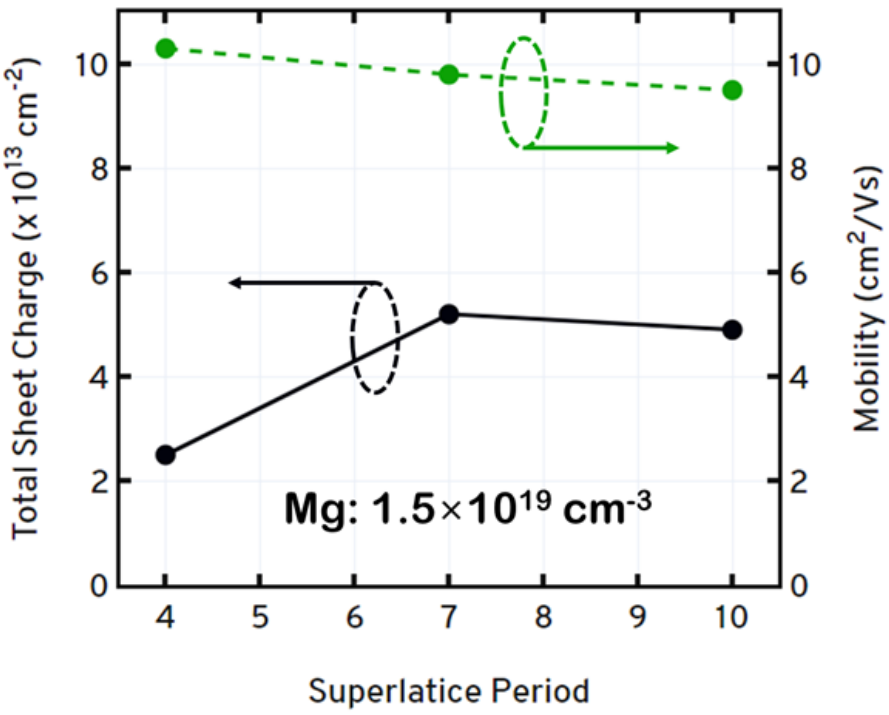

Figure 2.7 Room temperature Hall effect measurements yielding total sheet charge density and mobility of holes as a function of p-(GaN/AlGaN) SL periods.

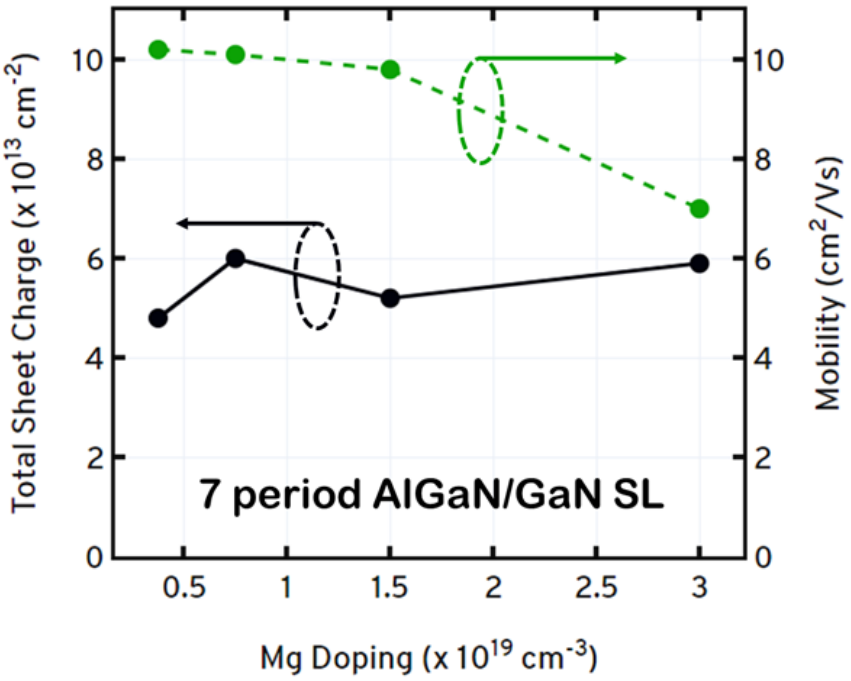

Figure 2.8 Room temperature Hall effect measurements yielding total sheet charge density and mobility of holes as a function of Mg doping in the p-(GaN/AlGaN) SL.

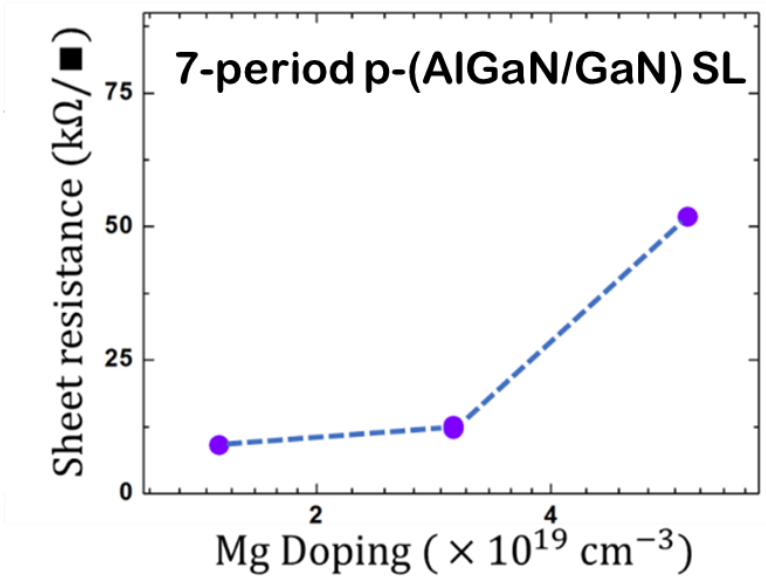

Figure 2.9 Sheet resistance as a function of Mg doping derived from the TLMs.

D. Test-Device: Fully-recessed gate p-channel FET

Post RT-Hall measurements, a fully-recessed gate p-channel FET was fabricated. For device fabrication, a 4 period SL sample with a Mg doping of 1.5×10^{19} cm^{-3} was chosen. The design used for device fabrication was a 3-period SL gate recess, as shown in the process flow in Figure 2.10. It is to be noted that to get the full benefits of a SL, fabrication of a Tri-gate or a FinFET is necessary, but since this is a preliminary test effort for material optimization, only the planar device is reported in this chapter. The resulting single channel pFET is shown in Figure 2.11. All the FET processing from Chapters 2 & 3 were carried out by Aditya Raj.

The fabrication steps were as follows:

1. PECVD SiO_2 was deposited on the as-grown sample followed by 3-minute RTA activation at 825℃;
2. SiO_2 was removed followed by ohmic metal deposition for source and drain contacts. A palladium (20nm)/ gold (200nm) metal stack was used for the ohmic contacts;
3. A low power etch was carried out for the mesa etch to isolate the devices;
4. A low power etch was also used for the 3-period SL gate recess etch to leave one conductive channel under the gate;
5. Atomic layer deposition (ALD) technique was used to deposit 10nm of aluminum oxide (Al_2O_3), to be used as the gate dielectric;
6. A gate metal stack of titanium/gold was deposited.

The fabricated device had a gate length (L_g) of 0.5μm, a gate-source spacing (L_{gs}) of 1.0μm, and a gate-drain spacing (L_{gd}) of 2.0μm.

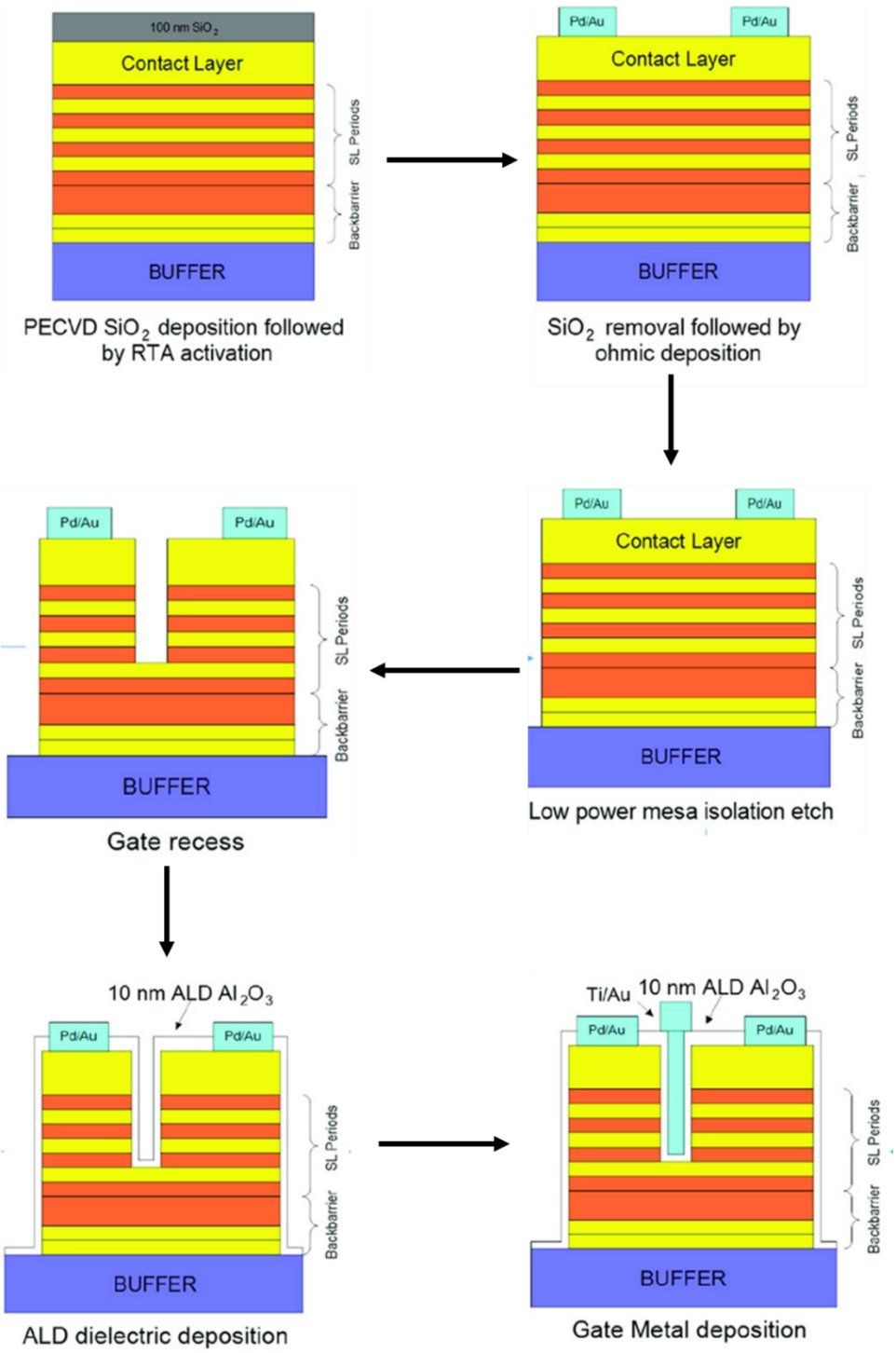

Figure 2.10 Device fabrication process flow for the p-(GaN/AlGaN) SL single channel pFET

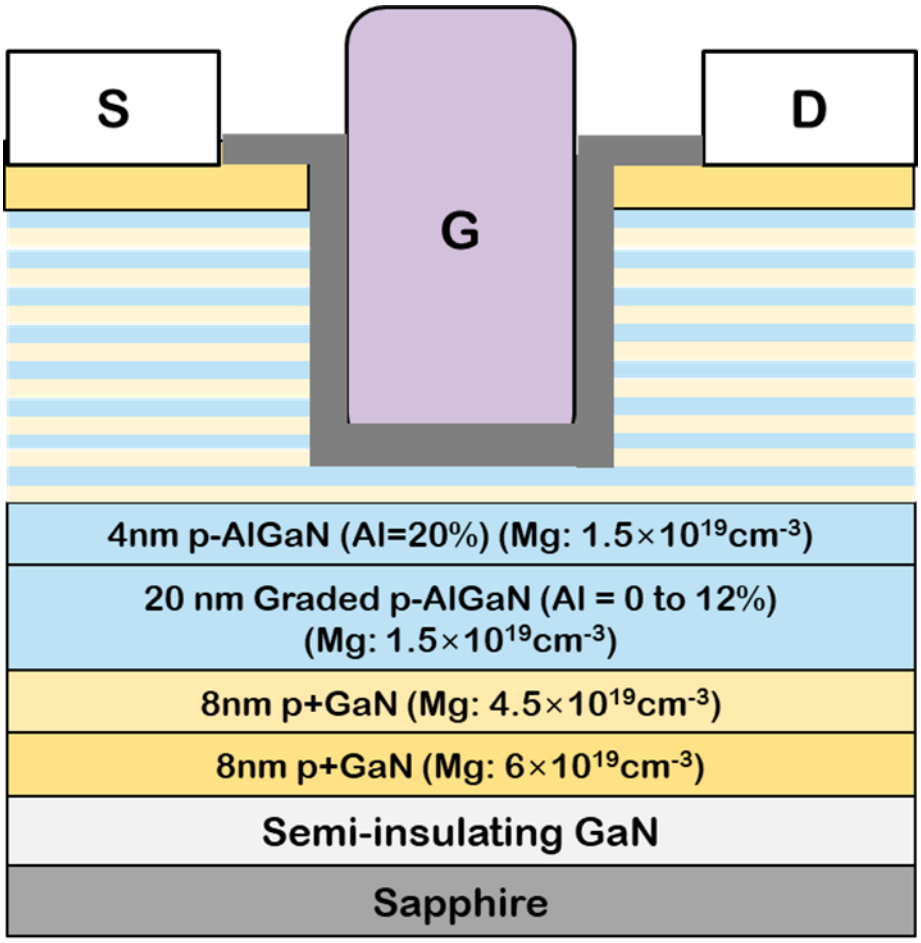

Figure 2.11 Resulting single channel p-(AlGaN/GaN) SL pFET with fully recessed gate

Figure 2.12 shows the output characteristics of the fabricated pFET devices. The device exhibited a maximum drain-source current (I_{DS}) = 3 mA/mm and an on-resistance (R_{ON}) = 3.48 kΩ.mm. Figure 2.13 shows the transfer characteristics of the device. Only one order of current modulation was observed ($I_{on}/I_{off} = 10^1$). The device did not pinch off due to gate leakage, and R_{ON} was dominated by contact resistance and valence band discontinuities for vertical transport.

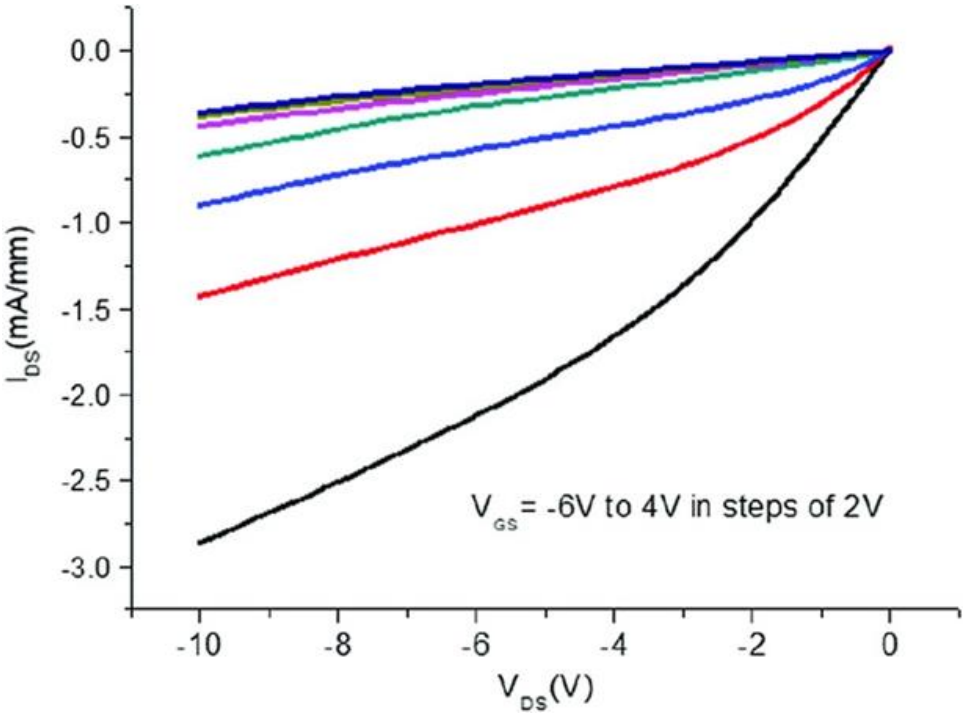

Figure 2.12 Output characteristics (I_{DS} as a function of V_{DS} for varying V_{GS}) of the AlGaN/GaN SL single channel pFET

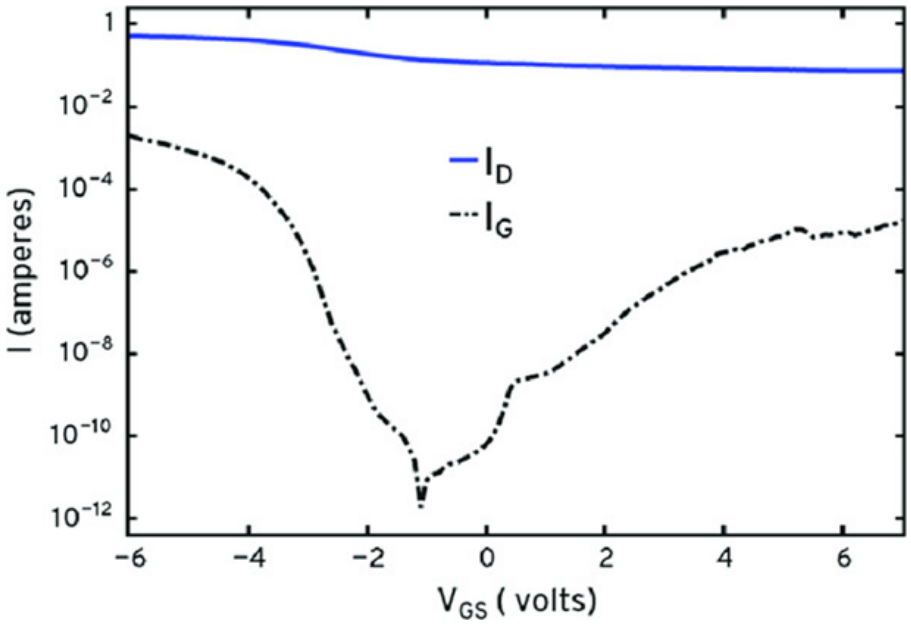

Figure 2.13 Transfer characteristics (I_{DS} and I_{GS} as a function of V_{GS}) of the AlGaN/GaN SL single channel pFET

Plasma etch damage of GaN under gate and sidewalls can lead to gate leakage, hampering the current modulation by the gate. It has been reported that tetramethylammonium hydroxide (TMAH) treatment at an elevated temperature removes the damaged region from the sidewall and makes it smooth [66]. So, the next set of planar SL pFET test devices were fabricated by incorporating a TMAH treatment. For devices fabricated with TMAH treatment, a 7-period AlGaN/GaN SL sample was chosen, taking advantage of its better electrical properties → $p_s = 6 \times 10^{13}$ cm^{-2} and $\mu_p = 10$ cm^2/Vs. While the required six-SL gate recess was deeper, the potential etch damage was mitigated by the subsequent TMAH etch. In the process flow described in the previous section, the TMAH treatment was performed at 80 ℃ for 30 min after gate etch (step 4 in Figure 2.10), to remove any material which was damaged during the gate dry etch from the sidewalls. The etch depth was = 103 nm, and the etching conditions were 5W BCl_3/Cl_2 etch in reactive ion etching (RIE).

Figure 2.14 shows the scanning electron microscopy (SEM) images before and after TMAH treatment on the sample. TMAH treatment was used here to remove the etch-damaged region from the sidewall. For the device with TMAH treatment, 10 nm SiO_2 was deposited by ALD to serve as a dielectric. SiO_2 was chosen as the dielectric over Al_2O_3 because of its higher band offset to mitigate gate leakage. The fabricated device had a gate length of 0.5μm, a gate-source spacing of 1.0μm, and a gate-drain spacing of 2.0μm.

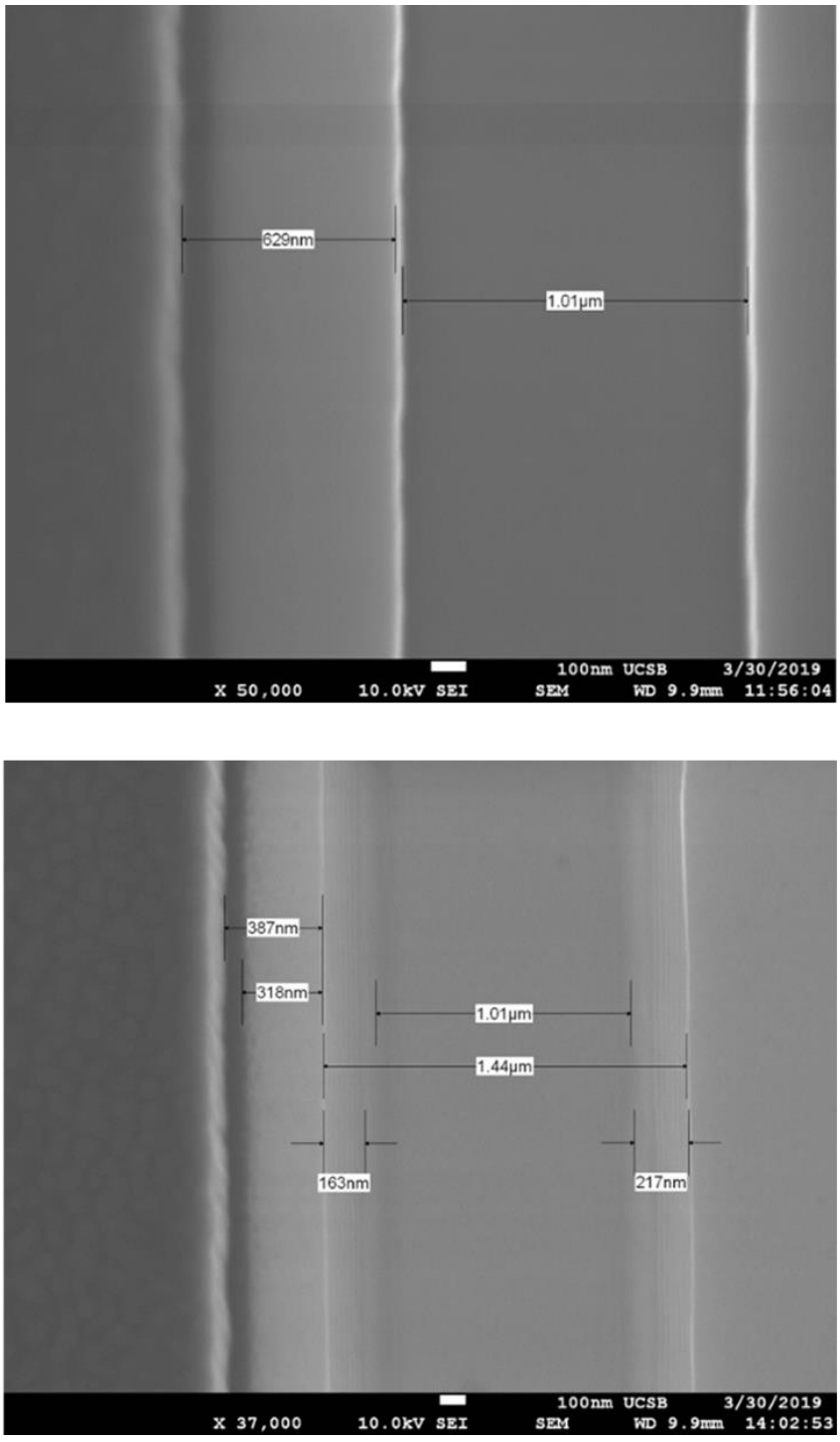

Figure 2.14 SEM images before (above) and after (below) TMAH treatment at 80℃ for 30 min.

As described earlier, TMAH treatment was implemented after the gate etch to remove any damaged material and hence reduce the gate leakage and subsequently pinch off the device. Using TLMs, a sheet resistance (Rsh) of 11.6 kΩ/sq and a contact resistance (Rc) of 14.9 Ω-mm were obtained, as shown in Figure 2.15. Post the TLM measurement, devices were fabricated incorporating the TMAH treatment, with the same dimensions as that of the device without TMAH treatment, reported earlier in the chapter.

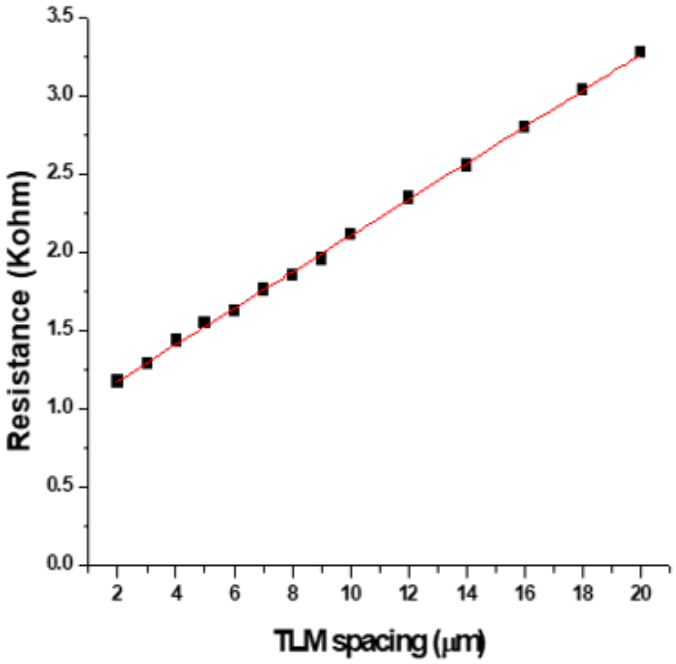

Figure 2.15 Resistance as a function of TLM spacing. An Rsh = 11.6 kΩ/sq and Rc = 14.9 Ω-mm were obtained

The transistors fabricated with TMAH treatment and with same dimensions as the device without the TMAH treatment exhibited a maximum current of 2.1 mA/mm for V_{GS} = -8V and V_{DS} = -10V. Figure 2.16 shows the output characteristics for this device. Log-scale transfer characteristics of this device are shown in Figure 2.17 with five orders of current modulation. Figure 2.17 also shows drain current (I_D) of the device without TMAH treatment, for comparison. Figure 2.18 shows linear-scale transfer characteristics as a

function of V_{DS} and Figure 2.19 shows the transconductance (g_m) as a function of V_{DS} with Maximum g_m = 0.24 mS/mm.

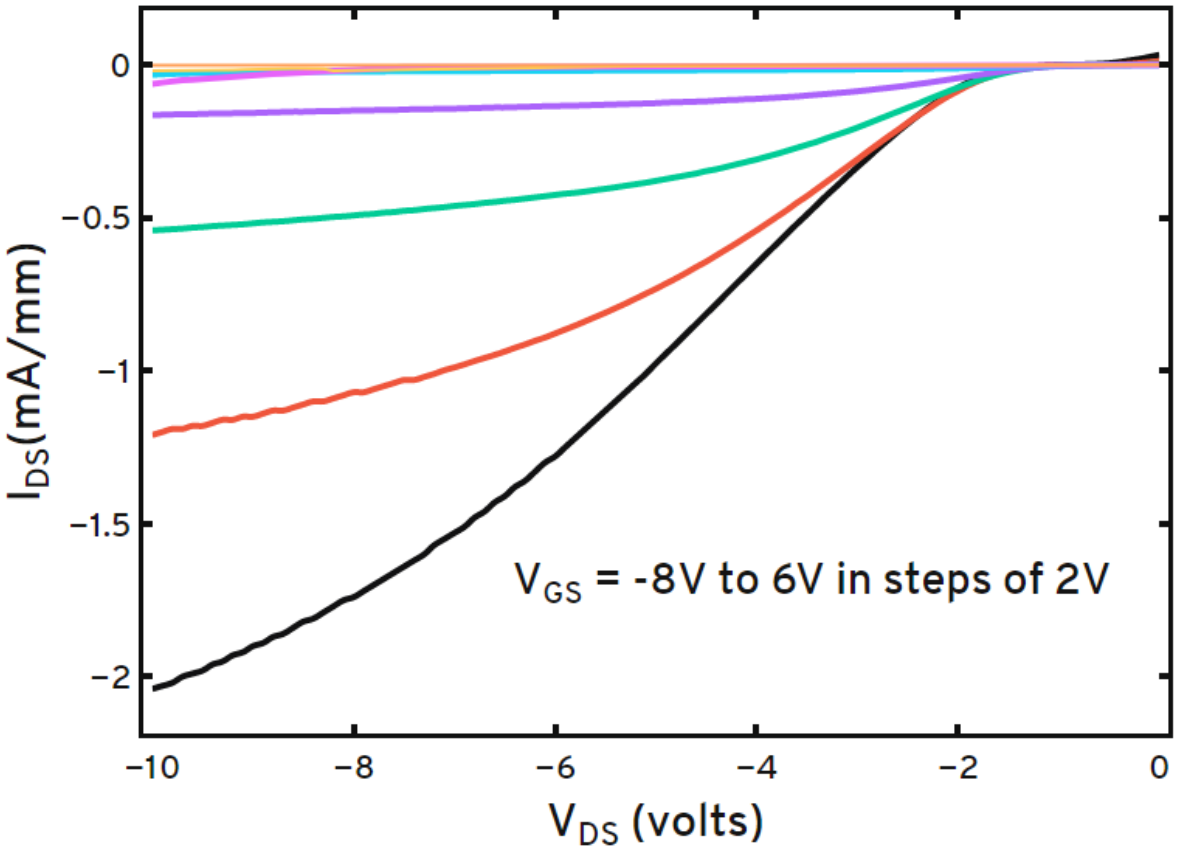

Figure 2.16 Output characteristics of the pFET fabricated with TMAH treatment (and with dimensions same as the device without TMAH treatment).

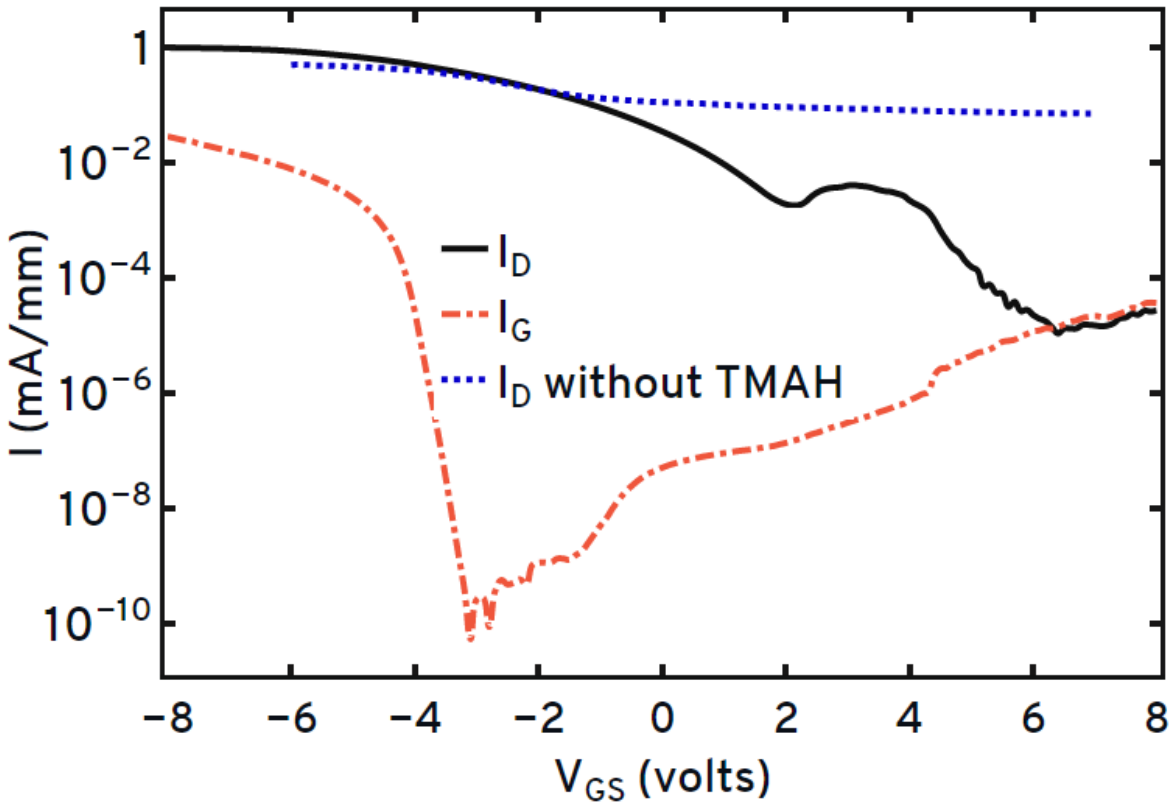

Figure 2.17 Log-scale transfer characteristics of the pFET fabricated with TMAH treatment, showing five orders of current modulation. I_D for device without TMAH treatment is shown for comparison.

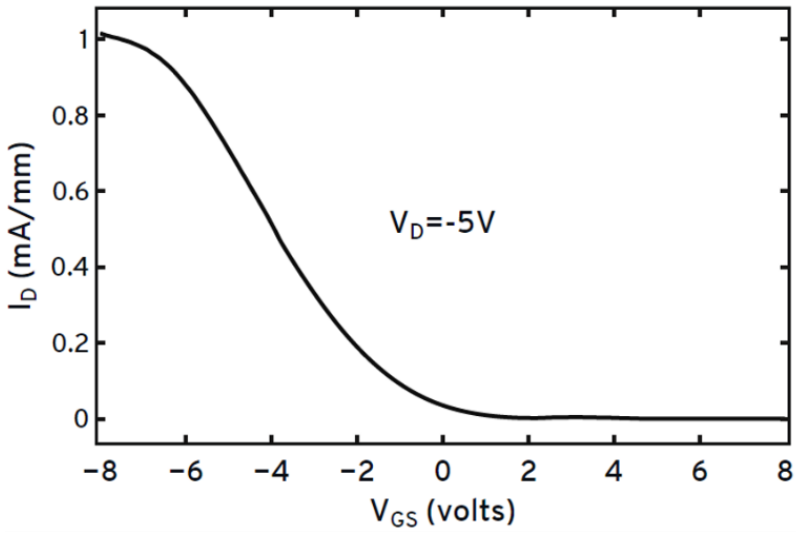

Figure 2.18 Linear-scale transfer characteristics as a function of V_{DS} of the pFET fabricated with TMAH treatment.

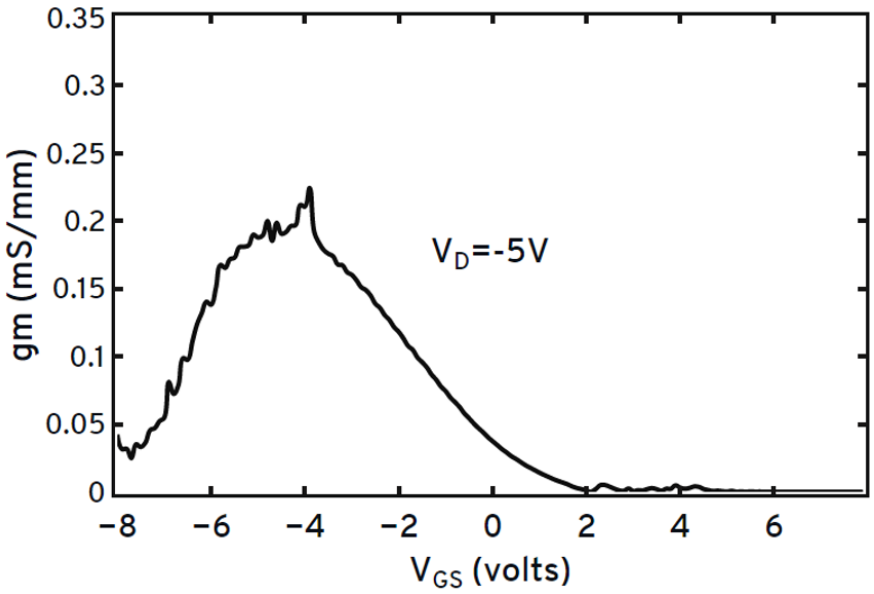

Figure 2.19 Transconductance as a function of V_{DS} of the pFET fabricated with TMAH treatment.

To improve the on-current of the device, the device with TMAH treatment was scaled further with the fabricated scaled device having a gate length (L_g) = 0.6 μm, a gate-source spacing (L_{gs}) = 0.4 μm, and a gate-drain spacing (L_{gd}) =0.7 μm. The scaled transistors with TMAH treatment exhibited a maximum current of 4.5 mA/mm for V_{GS} = -9 V and V_{DS} = -10V. The output characteristics are shown in Figure 2.20. The I_{DS} as a function of V_{DS} plot in Figure 2.20 showed a clear current saturation and effective gate control, whereas I_{DS} as a function of V_{GS} curve in Figure 2.21 showed five orders of modulation—$I_{on}/I_{off} = 10^5$. Linear scale transfer characteristics showed a pinch-off voltage of 2V and Maximum transconductance, g_m = 0.35 mS/mm, as seen in Figure 2.22. The output characteristics also depicted a slight turn-on voltage, which was due to the non-ohmic nature of metal contacts.

The reasons for the poorer contacts when applying an TMAH etch are still under investigation. The devices are limited by leakage in the forward and reverse bias, which manifest as a difference in device performance with and without TMAH treatment. While

there was no evidence of TMAH improving the on-current of the device, TMAH treatment significantly improved the current modulation of the devices (higher I_{on}/I_{off}) and ensured that the devices could be turned off.

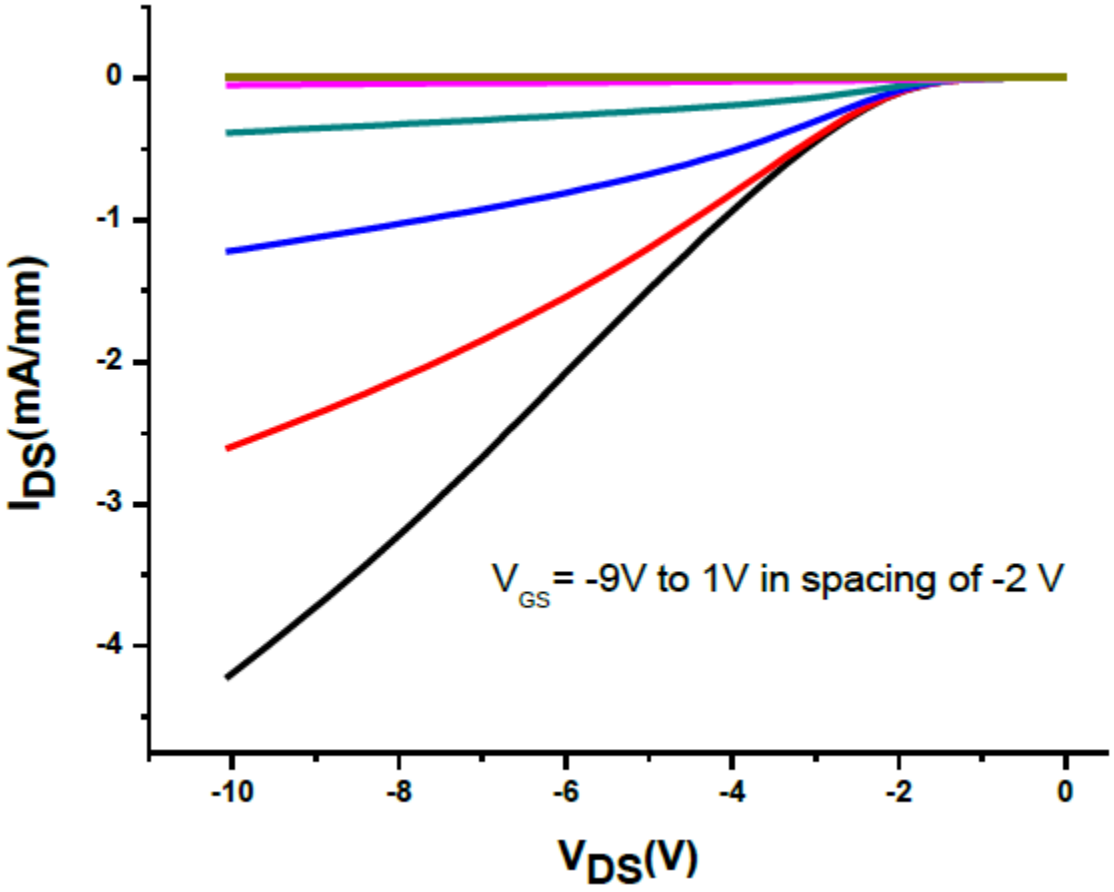

Figure 2.20 Output characteristics of the scaled pFET fabricated with TMAH treatment.

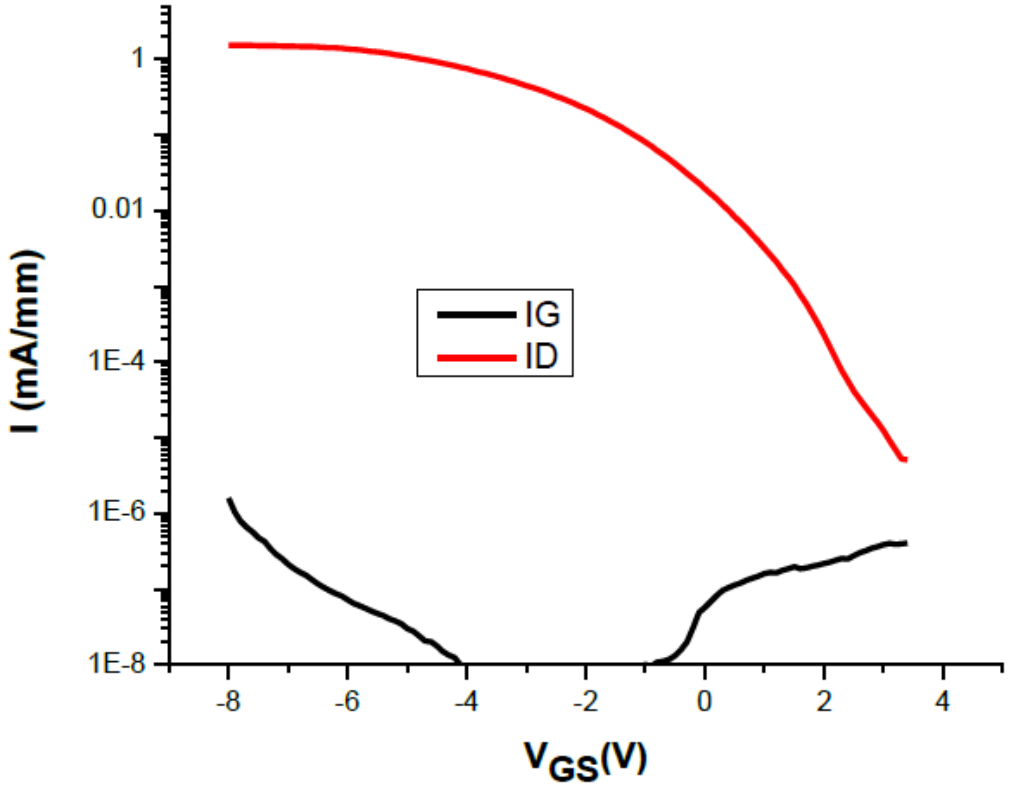

Figure 2.21 Log-scale transfer characteristics of the scaled pFET fabricated with TMAH treatment, showing five orders of current modulation.

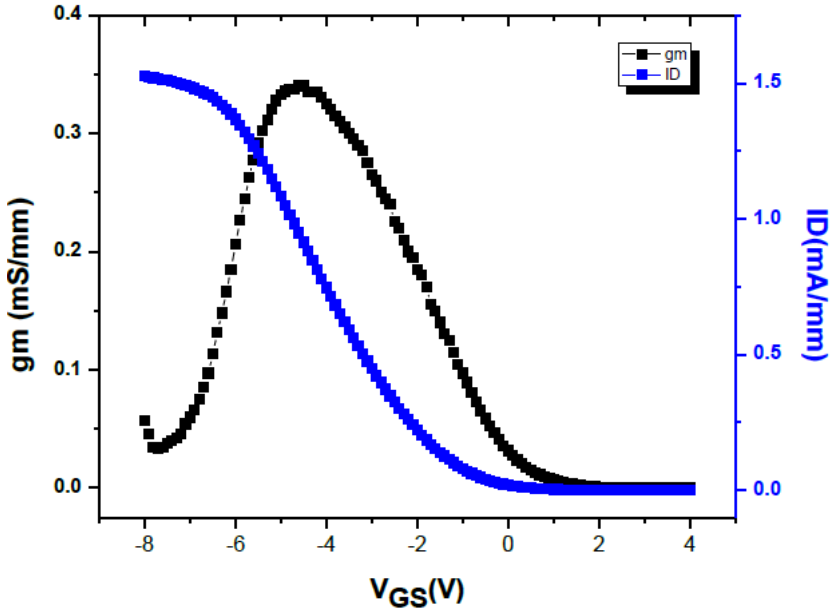

Figure 2.22 Linear-scale transfer characteristics of the scaled pFET fabricated with TMAH treatment, showing a pinch-off voltage of 2V and Max g_m = 0.35 mS/mm.

Planar pFETs fabricated from GaN/AlGaN SLs with a maximum I_{DS}= 4.5mA/mm were demonstrated. Devices with TMAH etch during fabrication exhibited high current modulation among the reported p-channel FETs based on AlGaN/GaN material system. Improvements in the device performance are expected through further optimization of a) contacts and gate dielectric and b) the composition, number of periods, and doping in the p-(GaN/AlGaN) SL.

The complete benefits of the SL structure can be obtained by design and fabrication of trigate or FinFETs with gates wrapping around an SL fin and modulating all the channels of the SL. In this study, first process modules toward the fabrication of trigate structures were developed. The FinFET structures will not be reported in this dissertation.

Using Ga-Polar uniformly doped p-type AlGaN/GaN SL, we achieved Rsh as low as 10kΩ/sq (with $p_s \sim 4$ to 6×10^{13} cm^{-2} and $\mu \sim 10$ cm^2/Vs). The next chapter deals with how the hole mobility could be improved further by modifying the Mg doping scheme, using MOVPE.

Chapter 3

N-Polar p-type Modulation Doped GaN/AlGaN Superlattice

A. Motivation for modulation doping

As holes in GaN intrinsically suffer from a low mobility (~10 $cm^2/V\ s$) compared to electrons (1000–1500 cm^2/Vs), a much larger number of holes are required to achieve similar currents in p-type as in n-type FETs [67]. GaN/AlGaN superlattices (SLs) are an attractive approach toward this goal. The use of Mg doped GaN/ AlGaN SL is a pathway to obtain a high hole concentration and mobility simultaneously. In a GaN/AlGaN SL, polarization effects create a periodic oscillation of energy bands, enhancing the ionization of deep acceptors. Free carriers are separated into parallel sheets, but their spatially averaged density is much higher than that in a bulk film. The mobility of holes in the 2DHG is greater than that in the bulk.

Modulation doping of the SL structure involves doping in such a way that the Mg doping is only provided away from the regions where 2DHG forms, and hole mobilities as high as 19 $cm^2/V\ s$ at a hole concentration of $1.9\times10^{18}\ cm^{-3}$ were measured for Ga-Polar SL samples

grown by molecular beam epitaxy [68]. The modulation doping scheme can be explained using Figure 3.1. If the samples were uniformly doped, Region A has high ionization rate, but low hole concentration, and Region B has low ionization rate but high hole concentration. In modulation doping, only Region A, which is away from the 2DHG is doped with Mg. This results in less impurity scattering for holes, and thus leads to a higher mobility. Figure 3.1 also shows the location of the 2DHG and the charge distribution in the superlattice. All the above observations were made for Ga-polar materials grown in the typical c or (0001) growth direction. The hole mobility in similar samples grown by MOCVD, however, was only about 10 cm^2/Vs (almost half of that observed using MBE) because of the well-known Mg surface riding effect (and Mg Memory effect) in MOVPE, preventing the formation of an abrupt doping profile.

Mg Memory effect: It has been observed that there are significant delay times between Cp_2Mg precursor injection to the MOVPE reactor and incorporation in the thin-films and between ceasing Cp_2Mg precursor flow into the reactor and decrease in Mg incorporation in GaN films [69]. Figure 3.2 from work carried out by N. Fichtenbaum et. al., shows the SIMS measurements for Ga-polar Mg-doped GaN MOVPE stack [70]. GaN:Mg/GaN:Si multilayer stacks show non-abrupt Mg doping in the samples. Figure 3.3 from the same work shows the SIMS measurements for N-polar Mg-doped GaN MOVPE stack, and Mg SIMS profile in N-polar GaN:Mg/GaN:Si multilayer stacks showed abrupt Mg profiles.

N-Polar GaN/AlGaN p-type SL growth therefore enables the accurate placement and control of Mg doping within the structure, and N-polar modulation doped p-type GaN/AlGaN SL promises higher mobility than uniformly doped Ga-polar sample for same doping levels.

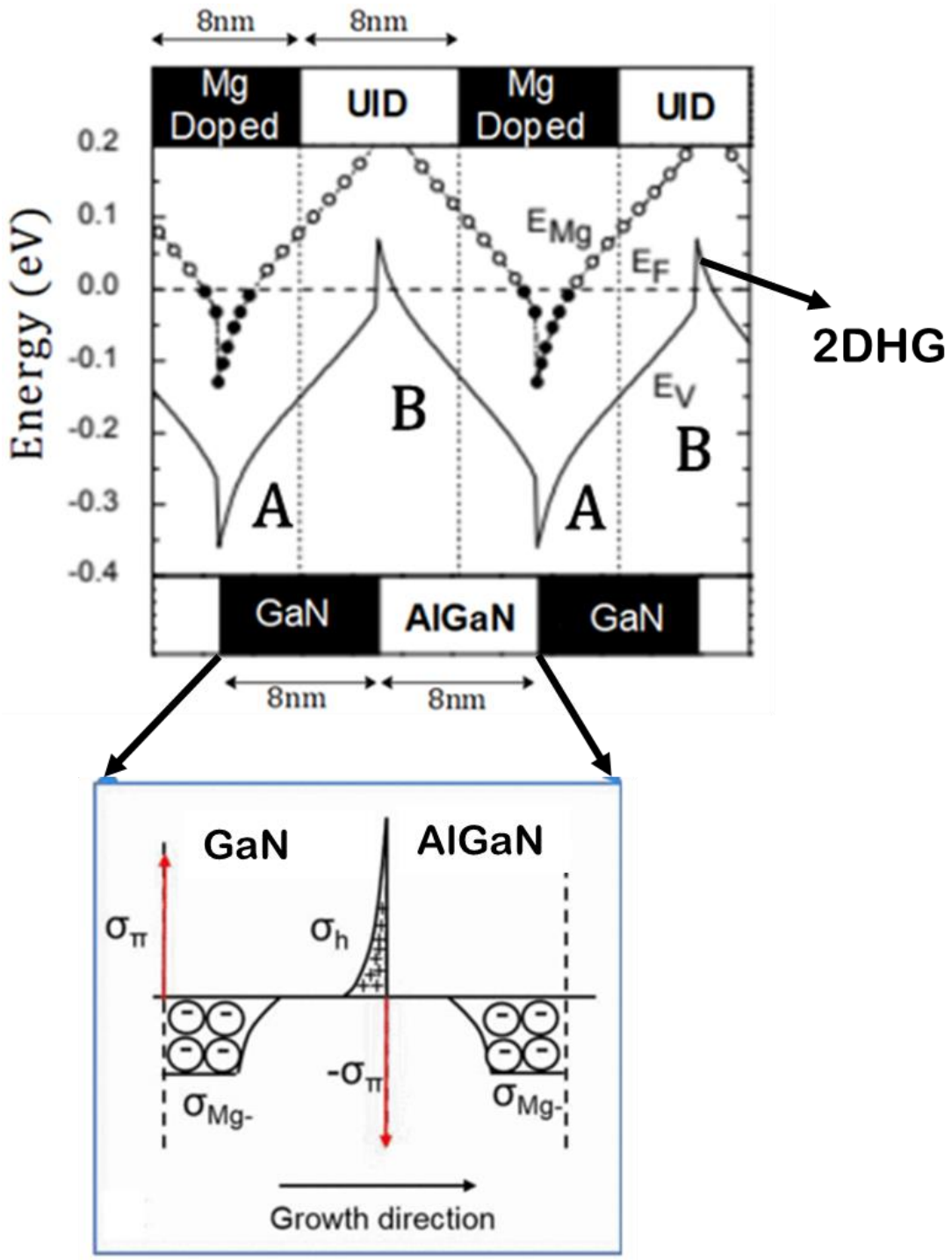

Figure 3.1 Valence Band and acceptor level in the modulation doped AlGaN/GaN SL structure along with the indication of the 2DHG formation, and charge distribution in the samples

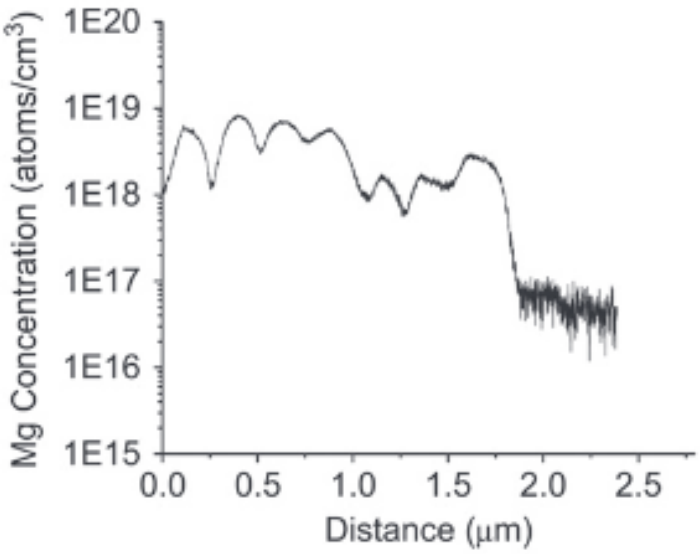

Figure 3.2 SIMS profile of Mg concentration in Ga-face GaN:Mg/GaN:Si multilayer stacks grown using MOVPE

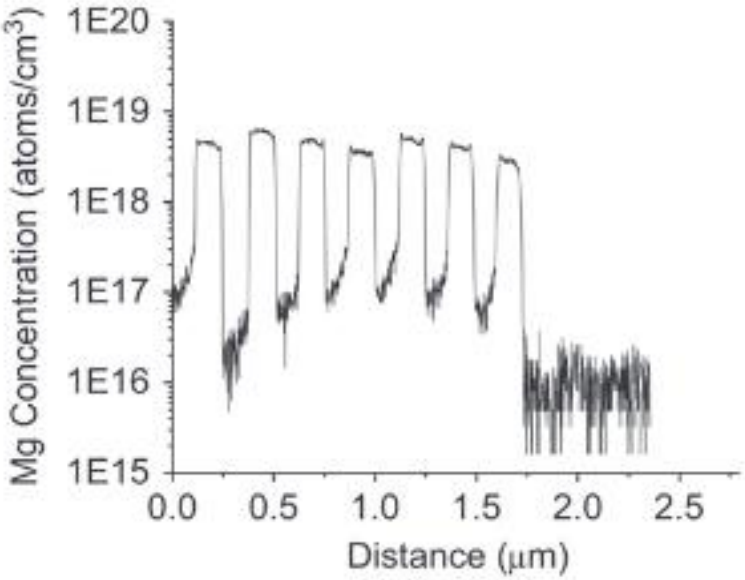

Figure 3.3 SIMS profile of Mg concentration in N-face GaN:Mg/GaN:Si multilayer stacks grown using MOVPE

[Figure 3.2 & Figure 3.3 Reprinted from Journal of Crystal Growth, "Impurity incorporation in heteroepitaxial N-face and Ga-face GaN films grown by metalorganic chemical vapor deposition", Vol 310, Issue 6, Pg 1124-1131, Authors: N.A. Fichtenbaum, T.E. Mates, S. Keller, S.P. DenBaars, U.K.Mishra Copyright 2008, with permission from Elsevier]

B. Epitaxial Design, MOCVD Growth & Material Characterization

The opposite direction of the internal electric field in N-polar compared to Ga-polar group-III nitride heterostructures and their different surface properties are attractive for enhancement mode and highly scaled transistors as well as solar cells and sensors. All samples reported in this chapter were grown by MOVPE using trimethylgallium, trimethylaluminum, cyclopentadienyl magnesium (Cp2Mg), and NH3 as precursors. The SL was grown on semi-insulating (SI) N-polar GaN base layers deposited on c-plane sapphire substrates with a misorientation of 4º from the a-plane, for a robust growth window [71].

Figure 3.4 shows the epitaxial structure of the grown N-polar modulation doped GaN/AlGaN superlattice. Samples with different numbers of superlattice periods and Mg doping were grown. The first 8 nm thick p+ GaN layer (GaN:Mg = 6×10^{19} cm^{-3}) above the SI-buffer was grown to stabilize Mg flow and to achieve a sharp Mg doping profile in the epitaxial structure. The modulation doped SLs were composed of 4–10 periods, with each period being composed of 4 nm u.i.d. (unintentionally doped) $Al_{0.2}Ga_{0.8}N$/ 4 nm p-$Al_{0.2}Ga_{0.8}N$ /4 nm p-GaN/ 4 nm u.i.d. GaN. The 20nm thick p+ GaN contact layer was doped with Mg=7.5×10^{19} cm^{-3} to facilitate fabrication of good contacts to the p-type SL and was derived from the work of C. Lund et al at UCSB [72].

Selected samples with uniform continuous Mg doping in the SL were also grown for comparison. The p-type SL stacks were grown at a temperature of 1155℃ and a pressure of 100 Torr. The samples were characterized using atomic force microscopy (AFM), secondary ion mass spectroscopy (SIMS), and X-Ray diffraction (XRD). The 2θ-ω scan of the 7 period SL sample taken around the (0004) GaN diffraction peak depicted in Figure 3.5 illustrates the good crystal quality and periodicity of the p-AlGaN/GaN SL [73].

Figure 3.4 Epitaxial structure of the grown N-polar modulation doped GaN/AlGaN superlattice. Samples with different numbers of superlattice periods and Mg doping were grown.

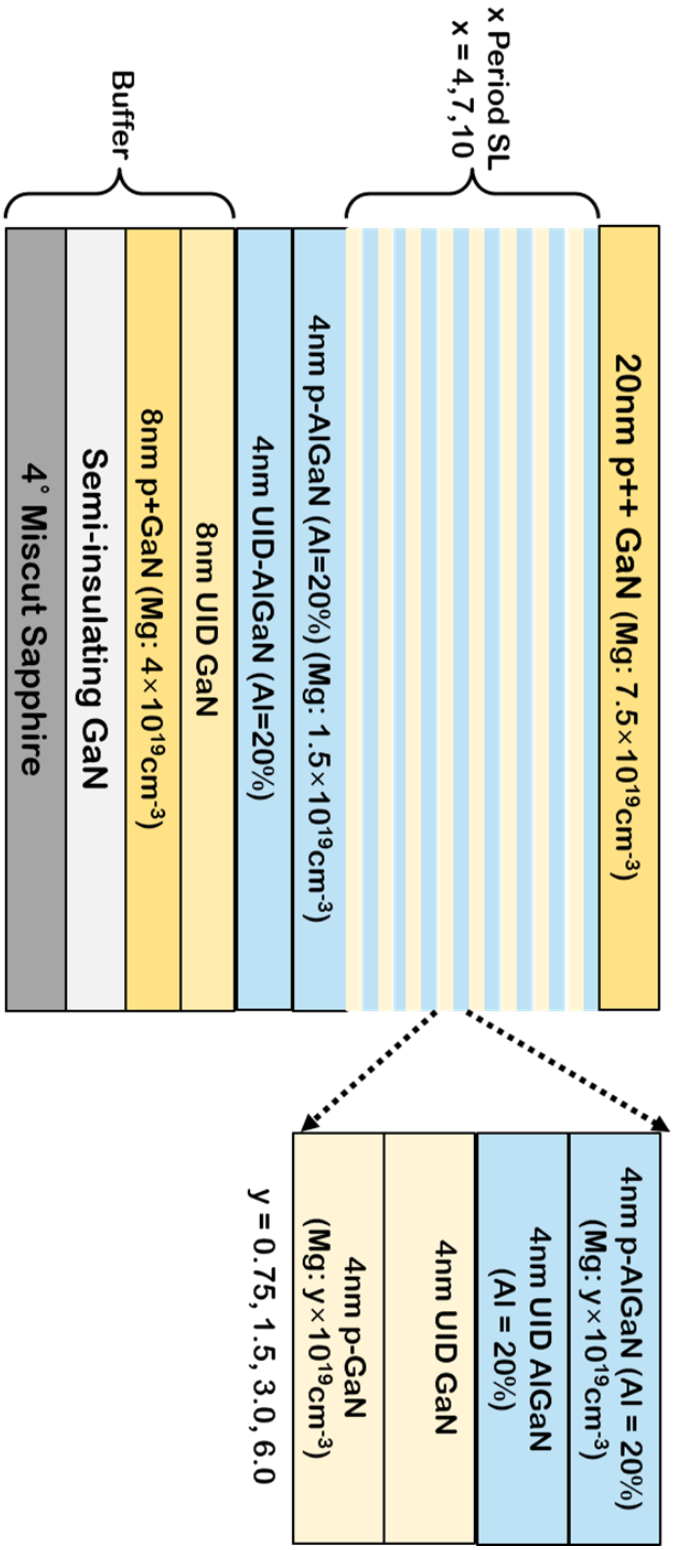

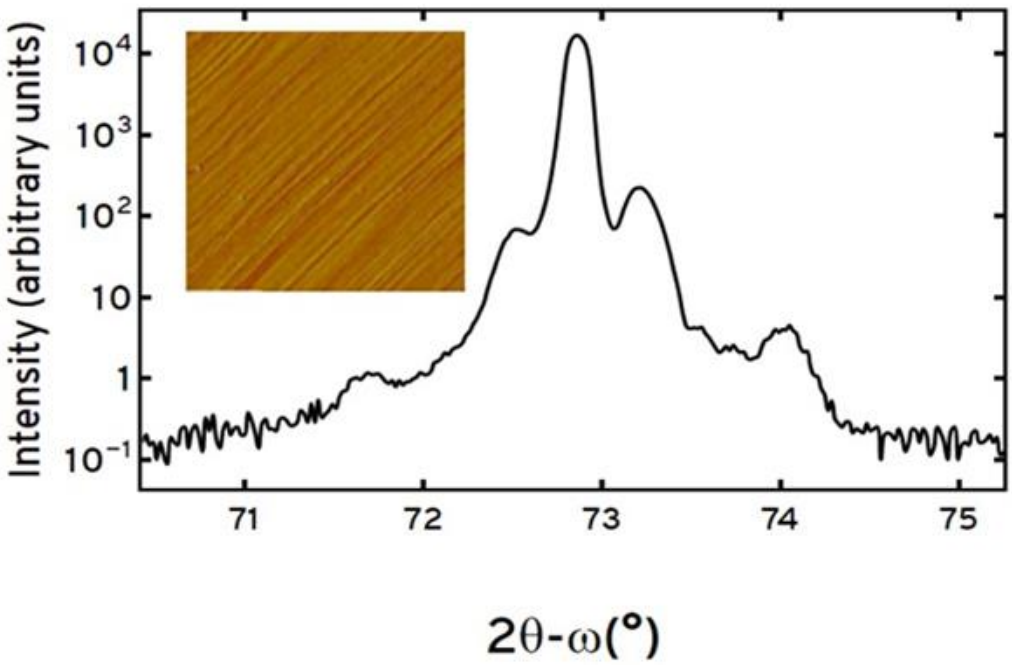

Figure 3.5 2θ-ω scan of a 7 period SL sample taken around the (0004) GaN diffraction peak. The inset displays the 10μm×10 μm AFM scan of the same sample (z-range = 2nm).

Figure 3.1 shows the SL valence band for the structures reported in this chapter. The 8nm GaN/8nm AlGaN thickness was chosen as the optimum thickness from previous work performed by Kozodoy et al. The electrical properties of the planar samples were investigated by room temperature Hall effect measurements (RT-Hall). MOVPE growths resulted in two series: (a) superlattice period series of 4, 7 and 10 SLs with a Mg modulation doping = 1.5×10^{19} cm^{-3} held constant, and (b) Mg doping series for a 7-period SL sample with Mg modulation doping of: 7.5×10^{18} cm^{-3}, 1.5×10^{19} cm^{-3}, 3.0×10^{19} cm^{-3} and $6.0\times10^{19}cm^{-3}$.

Ni-Au metal stack contacts were deposited on the 1.5cm × 1.5cm samples and prepared for RT Hall measurements. Mg dopant activation was carried out using RTA treatment at 825°C in a N_2/H_2 environment for 5 min to drive the hydrogen out of the sample, with 100nm of SiO2 deposited using PECVD. Four-probe RT-Hall measurements were carried

out (with the magnetic field strengths ranging from -6T to 6T) and the total sheet charge, and mobility were measured for each of the samples. Two series were classified for the measurements: (a) superlattice period series of 4, 7 and 10 SL, with a uniform Mg doping of 1.5×10^{19} cm^{-3}, and (b) Mg doping series for a 7-period SL with Mg doping varied from 7.5×10^{18} cm^{-3}, to 6.0×10^{19} cm^{-3}.

(a) Superlattice Period series: Holding the Mg doping constant at 1.5×10^{19} cm^{-3}, Figure 3.6 shows the measured total sheet charge concentration (p_s) and mobility as a function of the number of superlattice periods of 4, 7 and 10 p-type uniformly doped AlGaN/GaN SL.

Measured hole mobility (μ_p) remains steady around 15 cm^2/Vs (average) as the SL periods are varied, as expected. p_s increases linearly from 4 to 7 SL periods, but we do not observe the same increase when going from 7 to 10 SL periods. The hole sheet charge increased from 3.0×10^{13} cm^{-2} to 6.0×10^{13} cm^{-2} as the number of superlattice periods was increased from 4 to 10. The reduced increase in sheet charge when increasing the number SL periods from 7 to 10 was most likely associated with contacts leading to an error in measurement. While vertical hole transport in p-SLs was reported previously, the SLs in this study were designed for lateral not vertical transport, possibly limiting the number of SL periods which could be contacted. Note that a similar trend was observed for the complementary Ga-polar uniformly doped p-AlGaN/GaN samples reported in Chapter 2 of this dissertation. Therefore, for all further measurements, we went ahead with 7 SL samples as reliable RT-Hall measurements could be carried out.

(b) Mg doping series: Holding the SL period constant at 7 periods, Figure 3.7 shows the measured total sheet charge concentration (p_s) and mobility as a function of the Mg doping in the sample - 7.5×10^{18} cm^{-3}, 1.5×10^{19} cm^{-3}, 3.0×10^{19} cm^{-3} and $6.0\times10^{19}cm^{-3}$. The hole mobility decreased from 19 cm^2/Vs to 5 cm^2/Vs as the doping was increased from 7.5×10^{18} cm^{-3} to $6.0\times10^{19}cm^{-3}$. For a high sheet charge of 6.0×10^{13} cm^{-2}, a hole mobility of over 19 cm^2/Vs was achieved. These values are comparable to the values of mobility achieved in modulation doped p-type AlGaN/GaN SL samples grown using the MBE growth technique.

As can be seen in Figure 3.7, a corresponding uniformly doped N-polar sample was also grown for comparison, Mg=1.5×10^{19} cm^{-3}. The hole sheet charge in this sample was 4.5×10^{13} cm^{-2} with a mobility of 6.5 cm^2/Vs. The reduced sheet charge compared to the modulation doped sample corresponded to an overall higher Mg dopant concentration in the sample, and it was observed that the higher Mg content resulted in a reduced charge for all samples in this study.

The significantly lower hole mobility was a result of the increased scattering due to the presence of Mg dopants throughout the SL (even in the region where the 2DHG forms). Similarly, the hole mobility of the best N-polar modulation doped SL sample is twice as high as the mobility of Ga-polar modulation doped SL samples of similar doping levels. Note that for Ga-polar samples, no difference in the mobility between uniformly doped and modulation doped samples was observed due to the Mg riding effect discussed before, which prevents abrupt placement of Mg dopant. Effectively Ga-polar “modulation” doped sample is a uniformly doped sample with half the dopant concentration, as the Mg dopants are spread out in the SL.

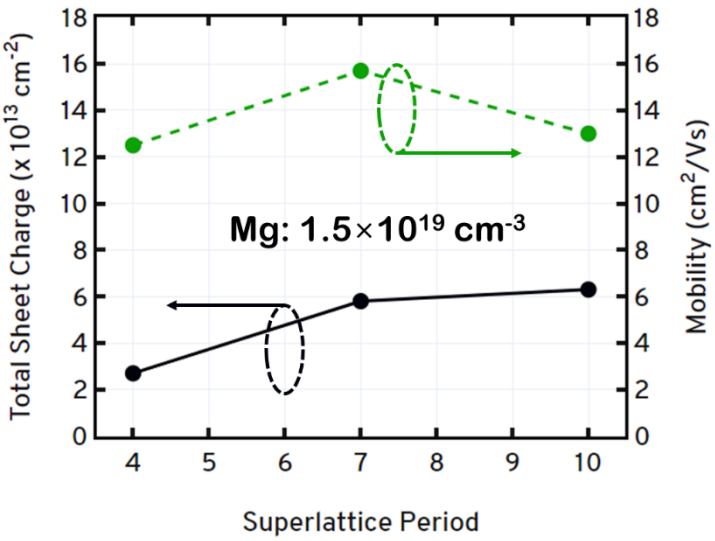

Figure 3.6 Total sheet charge density and hole mobility in the grown structure as a function of the SL periods in samples with a Mg doping of 1.5×10^{19} cm^{-3}.

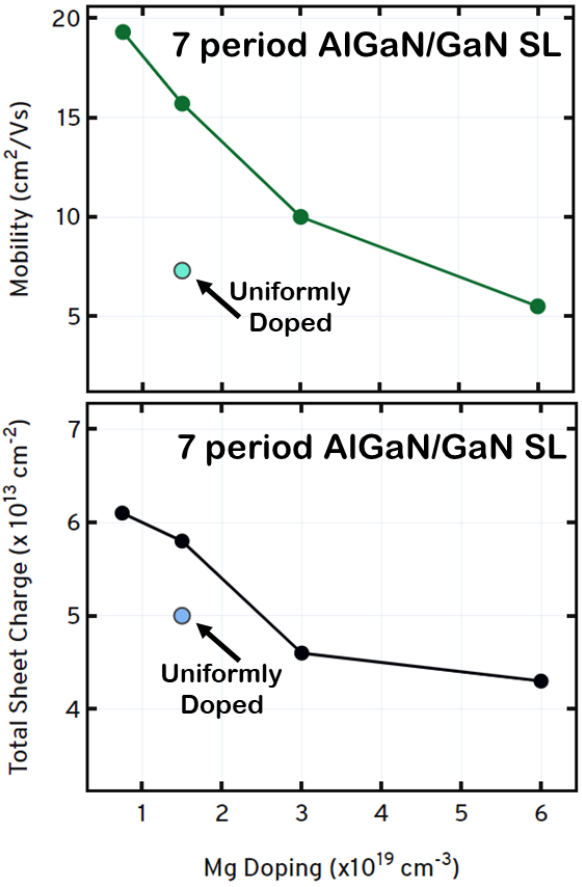

Figure 3.7 Hole mobility (above) and Total sheet charge density in the grown structure as a function of the Mg doping in samples with 7-period modulation doped SL.

D. Test device p-channel FETs

Two preliminary test devices were fabricated from the SL samples: (a) a N-polar planar p-FET with recessed SL with one p-channel and (b) N-polar SL FinFET, to investigate the applicability of the grown SL samples for field effect transistors (FETs).

(a) N-polar planar p-FET with recessed SL with one p-channel: Figure 3.8 shows the structure of the fabricated pFET. The fabrication process flow is the same as the Ga-Polar planar pFET mentioned in Chapter 2.D, except that a Ni/Au stack was used for the source and drain contacts (instead of the Pd/Au contacts in the case of Ga-polar devices), a Ti/Au stack was used for the gate contacts, and SiO_2 was used as the gate dielectric for the planar device.

The planar recessed p-FET was fabricated from a 7 period SL sample with a Mg doping of 1.5×10^{19} cm^{-3}. The fabricated device had the following dimensions: Gate length (L_g) =0.7µm; Gate-Source spacing (L_{gs}) =0.4µm; and Gate-Drain spacing (L_{gd}) =0.4µm.

The planar device exhibited a maximum drain-source current (I_{DS}) = 5.5 mA/mm and an On-resistance (R_{ON}) = 1.82 kΩ.mm. The device had a turn-on voltage of 2.5 V due to the lack of Ohmic contacts with all SL channels. Figure 3.9 shows the output characteristics (I_{DS} as a function of V_{DS} with varying V_{GS}) of the N-polar recessed SL single channel pFET. TMAH was used in the Ga-Polar case to solve the issue of leakage due to etch damage, but due to the high chemical reactivity of the N-Polar material, TMAH treatment cannot be carried out to either remove the etch damage, or to scale the device.

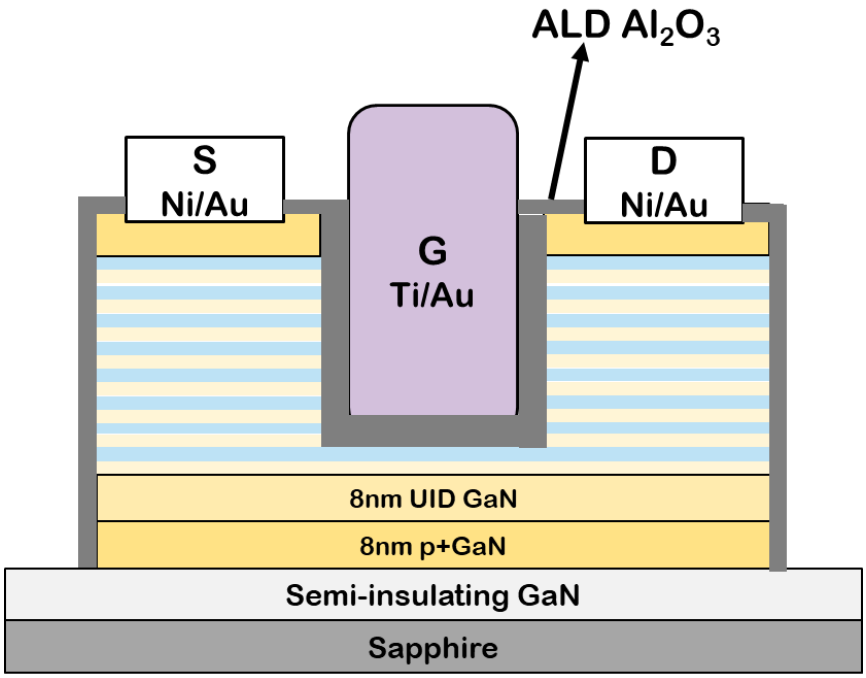

Figure 3.8 Schematic of N-polar modulation doped planar, SL recessed single channel pFET

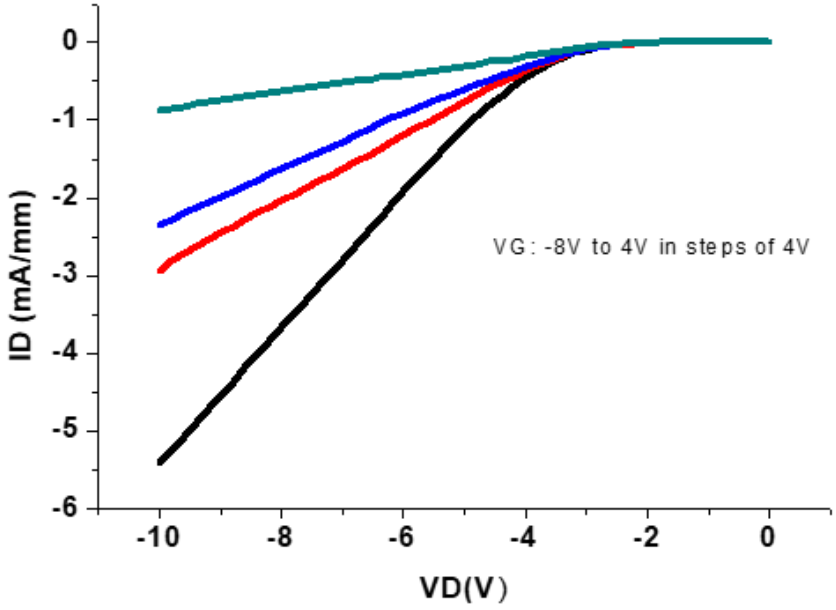

Figure 3.9 Output characteristics of N-polar modulation doped planar, SL recessed single channel pFET

(b) N-polar SL p-FinFET: To use all the SL channels, the trigate or FinFET was fabricated with the gate wrapped around all the 10 SL channels in a sample with a Mg doping of 7.5×10^{18} cm^{-3}. Figure 3.10 shows the fabricated FinFET along with an SEM (scanning electron microscopy) image of the device. Figure 3.11 shows the process flow of the pFinFET.

The fabricated device had the following dimensions: Gate length (L_g) =1.0µm; Gate-Source spacing (L_{gs}) =3.0µm; and Gate-Drain spacing (L_{gd}) =4.0µm. This device resulted in the maximum drain-source current of 120 mA/mm with the fin-width being 300 nm. Figure 3.12 shows the Output characteristics of the N-polar pFinFET. Both the fabricated devices do not turn-off. Further improvements in the device performance are expected with further process optimization including scaling of the fins in the FinFET, as well as N-polar processing optimization.

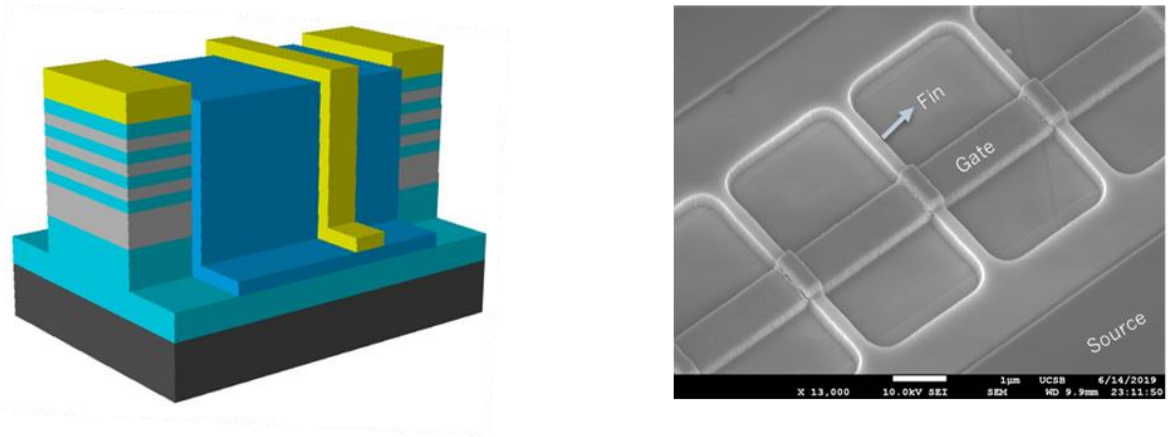

Figure 3.10 Fabricated N-polar p-FinFET along with an image of the device

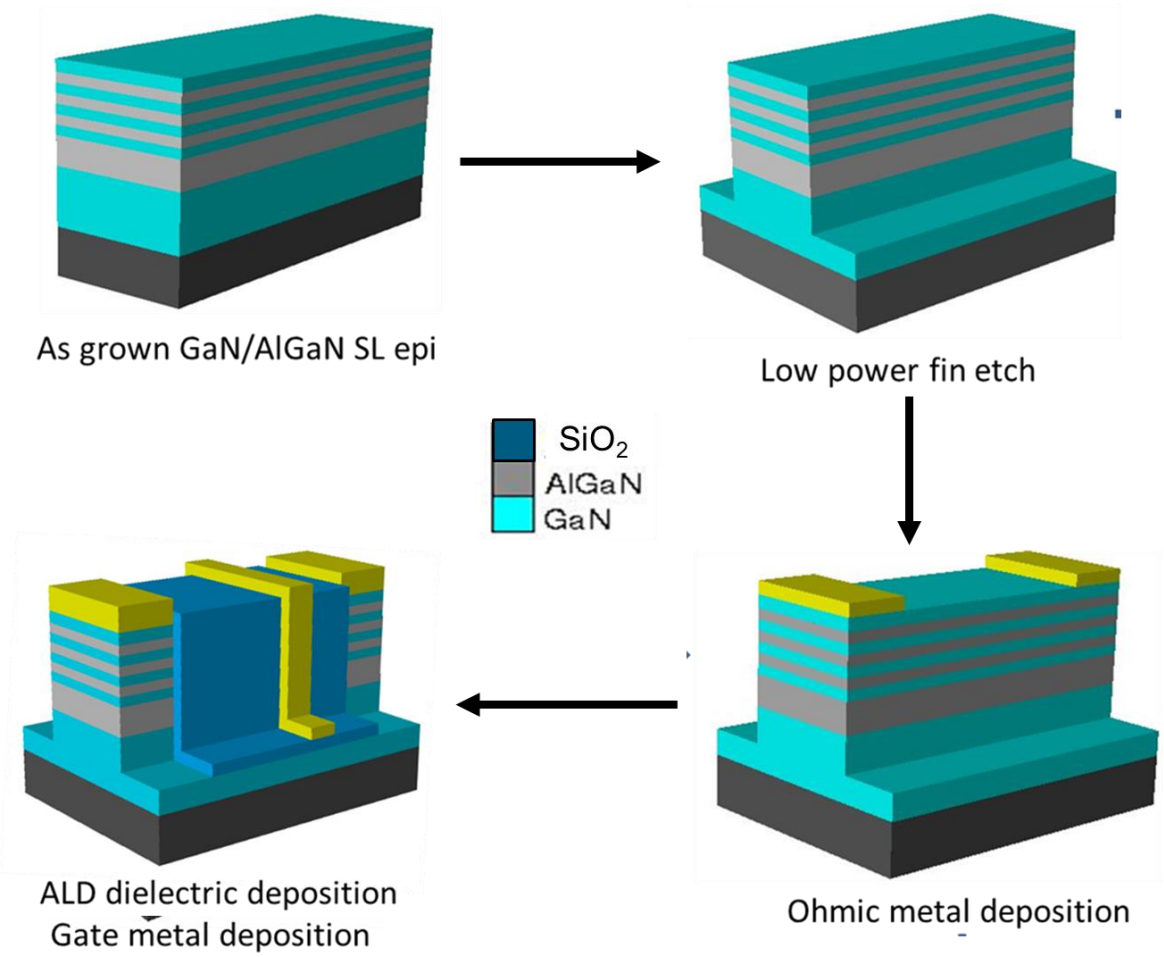

Figure 3.11 Device fabrication process flow for the p-type modulation doped (GaN/AlGaN) SL pFinFET

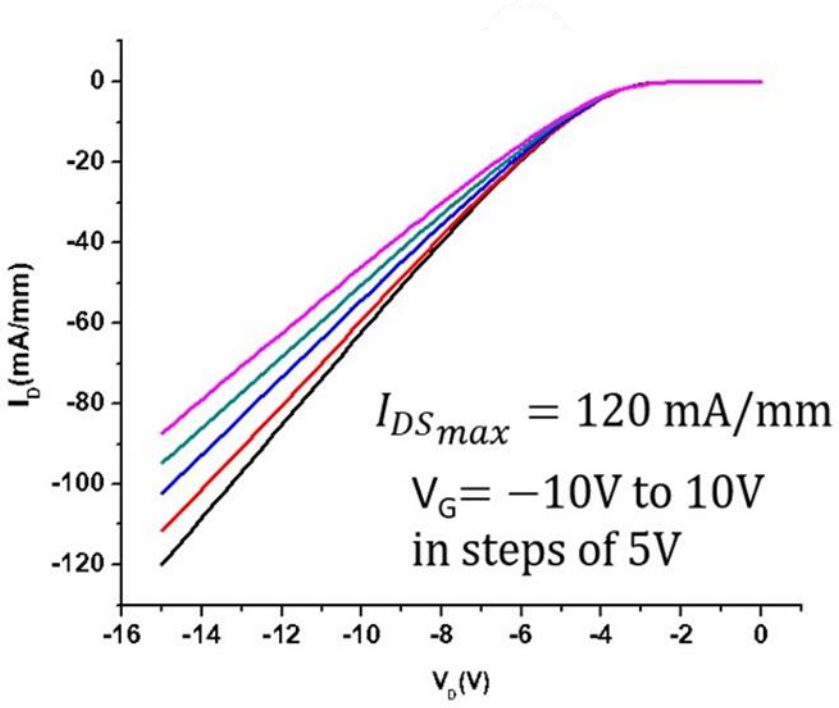

Figure 3.12 Output characteristics of N-polar modulation doped SL pFinFET

E. Benchmarking the material properties

N-polar modulation doped GaN/AlGaN SLs were grown with a high sheet charge of 6×10^{13} cm^{-2} and mobility of over 19 cm^2/Vs, resulting in a sheet resistance of ~ 5kΩ/sq, lowest among all p-type III-nitride systems reported for transistor applications. The reported mobility of 19 cm^2/Vs is an MOVPE record, and is comparable to MBE values for hole mobility, at comparable hole concentrations. In comparison, the Ga-polar samples (reported from Chapter 2) had a sheet charge of 4 to 6×10^{13} cm^{-2} and a mobility of 10 cm^2/Vs, resulting in a sheet resistance of ~ 10kΩ/sq.

Figure 3.13 benchmarks sheet resistance of all reported platforms used for III-nitride pFETs, with the N-polar modulation doped GaN/AlGaN SL reported in this chapter showing the lowest Rsh [73].

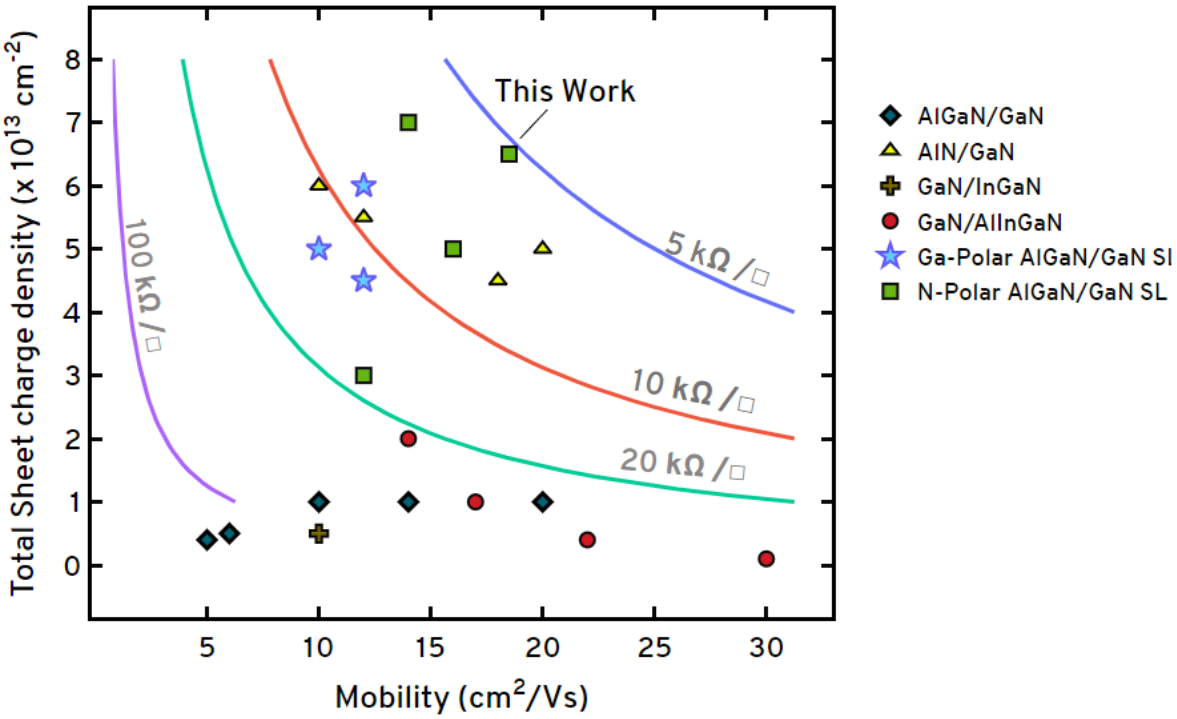

Figure 3.13 Sheet charge density and mobility data for the reported p-channel III-nitride systems in the literature, which were utilized for transistor applications. N-polar modulation doped AlGaN/GaN SL from the present chapter has the lowest sheet resistance reported using the MOCVD growth technique

Chapter 4

Acceptor-like traps at Positive Polarization interfaces in p-type doped III-nitrides

A. Addition of AlN IL in N-polar GaN/AlGaN SL

Previously in Chapters 2 and 3, we have investigated both p-type uniformly doped and modulation-doped AlGaN/ GaN superlattices. While the more common Ga-polar SL grown in the typical c or (0001) growth direction was used in Chapter 2, Chapter 3 used N-polar p-type SL grown in the -c or $(000\bar{1})$ direction, as significantly sharper Mg doping profiles were previously observed in this case [70]. It, therefore, enables the accurate placement and control of Mg doping within the structure, achieving higher mobilities via modulation doping. These samples resulted in p-type sheet resistances as low as 5kΩ/sq.

The next question to answer was if we can reduce this sheet resistance even further. Going back to the basics, sheet resistance is defined by Equation (2), where $q = 1.6\times10^{-19}$ C, p is the total sheet charge of holes in the sample, and μ is the hole mobility [74].

$$\mathbf{R_{Sheet}} = {}^{\mathbf{1}}/_{\boldsymbol{qp\mu}} \qquad \mathbf{Eq(2)}$$

Since q is a constant, we have two main knobs, p and μ, which when increased would lead to a decrease in R_{sheet}. One method to increase p right away is by increasing the Al mole fraction in the AlGaN layers of the SL. But this would potentially result in the reduction of the already low hole mobility in III-nitrides for higher Al mole fractions, so this approach was tabled. Another main concern is the excess strain caused by increasing the Al mole fraction in the multi-layer SL stacks.

Previous studies have shown that AlN interlayers in AlGaN/GaN high electron mobility transistors (HEMTs) result in higher charge and mobilities in the two-dimensional electron gas (2DEG) channels [75, 76]. In particular, the use of AlN at the interface where 2DEG was formed would remove the effect of alloy scattering and hence result in higher electron mobilities. Using the same train of thought, we studied p-type modulation doped GaN/AlN/AlGaN superlattices to investigate the impact, if any, of the AlN interlayer on the total hole sheet charge and mobility.

All samples reported here were grown by metal organic vapor phase epitaxy (MOVPE) using trimethylgallium, trimethylaluminum, cyclopentadienyl magnesium (Cp_2Mg), and NH_3 as precursors. The p-type epitaxial layers were grown on semi-insulating (SI) N-polar GaN base layers deposited on c-plane sapphire substrates with a misorientation of 4º from the a-plane. The background impurity concentrations were ~$8\times10^{17}cm^{-3}$ for oxygen and ~$2–3\times10^{17}cm^{-3}$ for carbon and hydrogen measured using secondary ion mass spectroscopy (SIMS). These values are typical for N-polar AlGaN grown by MOCVD [71].

The p-type SL stacks were grown at a temperature of 1155℃ and a pressure of 100 torr. Figure 4.1 shows the epitaxial structure of the SL samples grown for this AlN interlayer study. A 7-period SL stack was chosen for its reliability during Hall-effect measurements.

Each SL period consisted of 5 nm GaN:Mg/ 5nm UID GaN/ x nm UID AlN/ (5-x) nm UID $Al_{0.24}Ga_{0.76}N$ / 5nm $Al_{0.24}Ga_{0.76}N$:Mg, where the Mg doping was varied from 3.75×10^{18} cm^{-3} to 2.5×10^{19} cm^{-3}, and the AlN layer thickness was varied between 0nm to 1.6nm. Each SL period had a fixed total thickness of 20nm, with the total p-type doped layers (GaN:Mg & AlGaN:Mg) being 10nm. A 20nm p^{++} GaN contact layer, doped with 7.5×10^{19} cm^{-3} of Mg, was grown in situ on the SL stack to facilitate fabrication of good contacts to the p-type SL [72].

Figure 4.1 Schematic epitaxial structure of the grown 7-period N-polar modulation-doped GaN/ AlN/AlGaN superlattices. The schematic shows the thickness of the GaN, AlN and AlGaN layers for each period, as well as the AlGaN composition for the series. *x* indicates the AlN interlayer thickness, and *y* represents the Mg doping level.

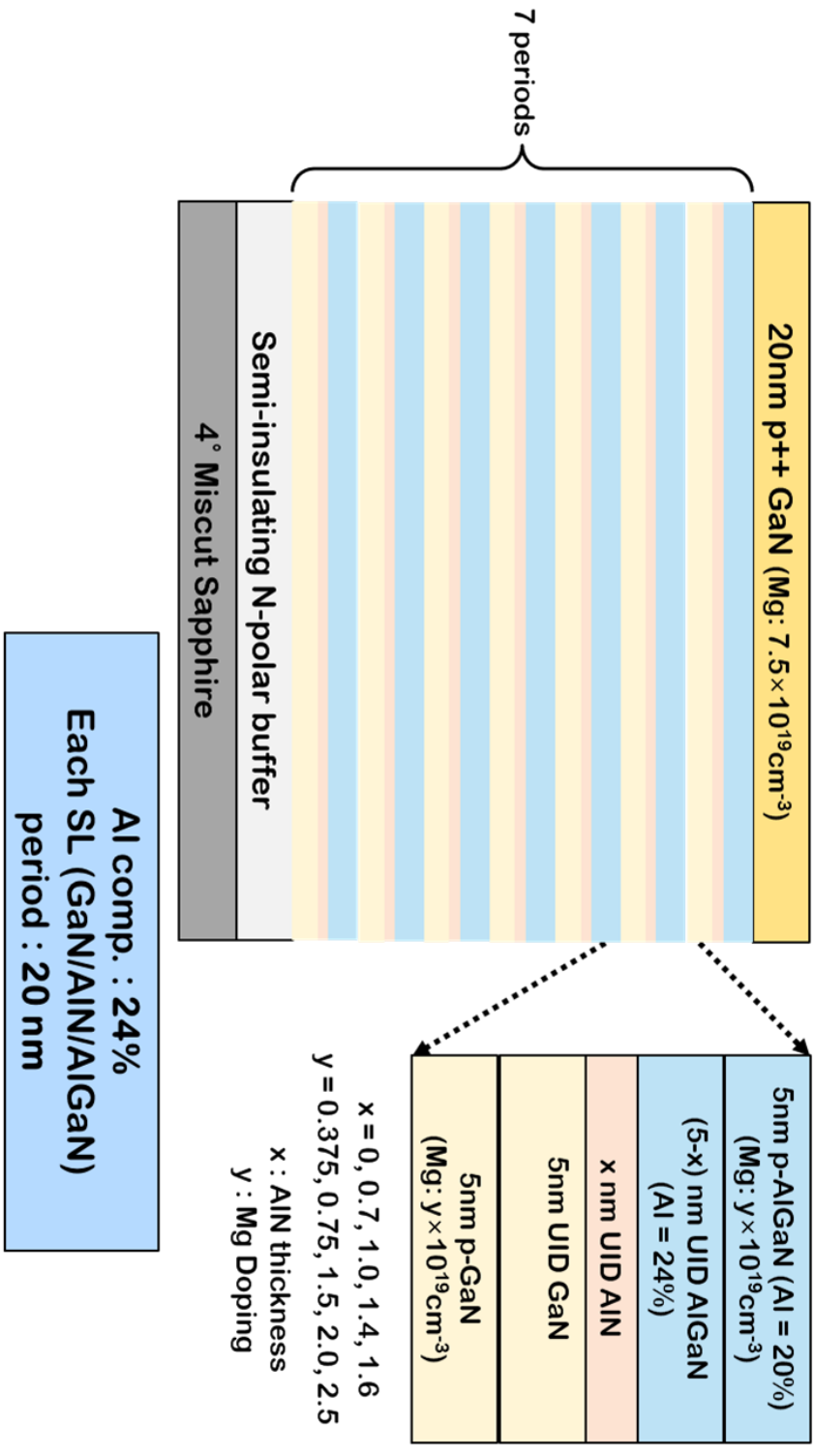

B. Material Charcterization & Hall Measurement

The samples were characterized using X-Ray Diffraction (XRD) (carried out by Dr. Islam Sayed) to measure the AlGaN composition and thickness of the GaN, AlN, and AlGaN layers. Figure 3.2 shows the 2θ-ω XRD spectra for a representative AlN thickness series presented in this chapter (Mg doping = 3.75×10^{18} cm^{-3}). The inset also shows an AFM image for a sample in this series with a smooth morphology (rms roughness~ 0.23nm).

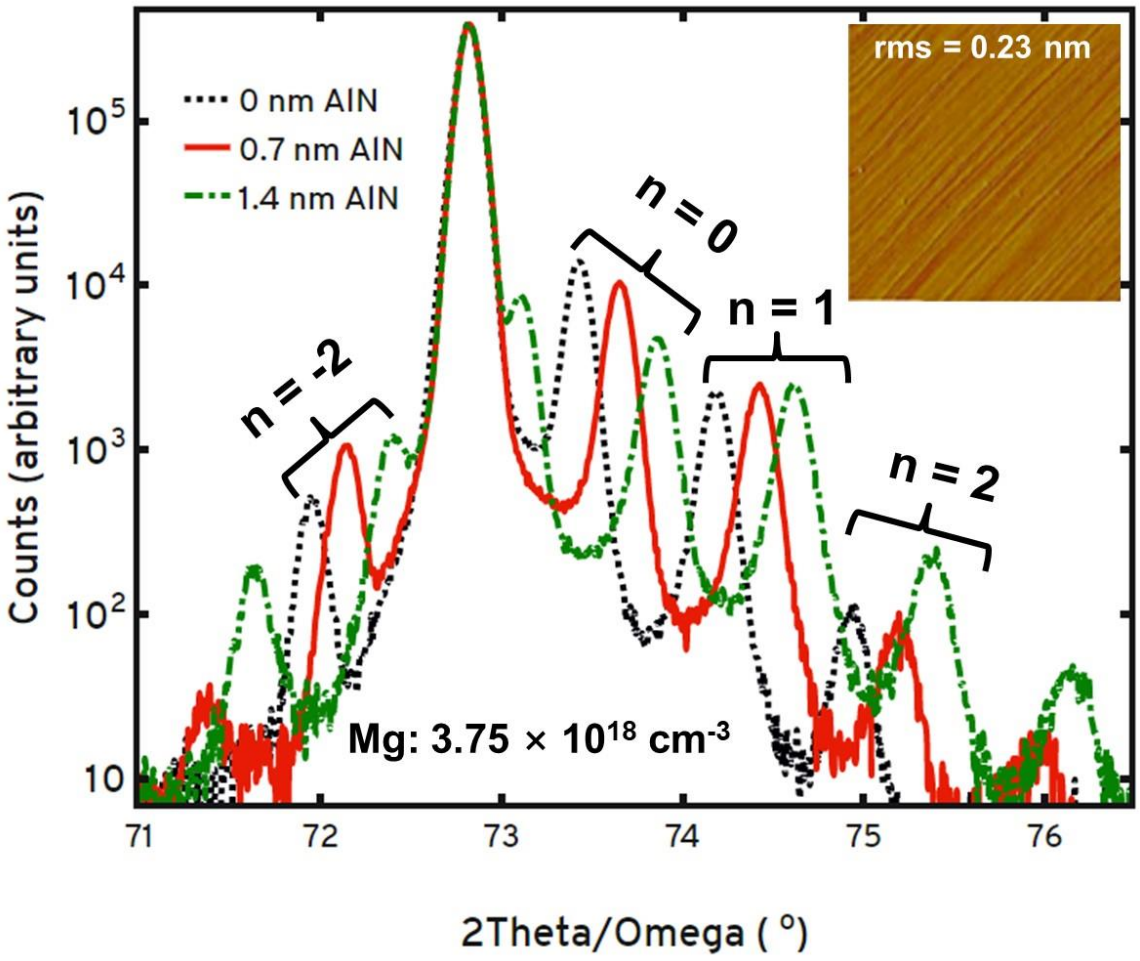

Figure 4.2 XRD 2θ-ω spectra for a representative AlN thickness series for the samples reported in this study with a Mg doping = 3.75×10^{18} cm^{-3}. Inset: 10×10 μm^2 AFM scan of the reported sample with rms roughness ~ 0.23 nm.

The samples were protected with 100 nm of SiO_2 deposited using PECVD following which Mg activation was carried out at 800°C using rapid thermal annealing (RTA), and Ni/Au contacts were deposited to prepare the 1.5 cm × 1.5 cm samples for room temperature Hall measurements. Energy band diagram calculations and total sheet charge simulations assuming the absence of any acceptor traps were carried out using STR-FETIS®. In addition, band diagram simulations were conducted using the Silvaco - Atlas software package. Please refer to **Appendix A** for complete details (and as a primer) on the band-diagram calculation model developed using STR-FETIS package, and the methodology used to calculate the Mg doping in the samples presented.

Figure 4.3 shows the total sheet charge of holes in the samples as a function of the AlN layer thickness, for varying Mg doping series. The figure presents a comparison between the experimentally measured data (solid lines), and the simulated/calculated data from STR-FETIS models (dotted lines). There is agreement between the experimentally measured values of total sheet charge and simulations for samples with higher Mg doping ($\geq 1.5\times10^{19} cm^{-3}$) and thinner (0.7nm) or no AlN interlayer. For the rest of the samples, the measured sheet charge is very high compared to the values obtained from simulations (in some cases even higher than the Mg dopants put into the sample during growth).

As an example, for the sample with a Mg doping of $7.5\times10^{18} cm^{-3}$ and AlN layer thickness = 1.6nm, the simulations give a total sheet charge of 7×10^{13} cm^{-2}, whereas the value obtained by the Hall measurements was as high as 1.4×10^{14} cm^{-2}. For such samples, we propose that the additional charge originates from the ionization of acceptor-like traps at the positive polarization interfaces in these samples, akin to the donor-like trap at the negative polarization interface recently identified as the N-vacancy [77,78].

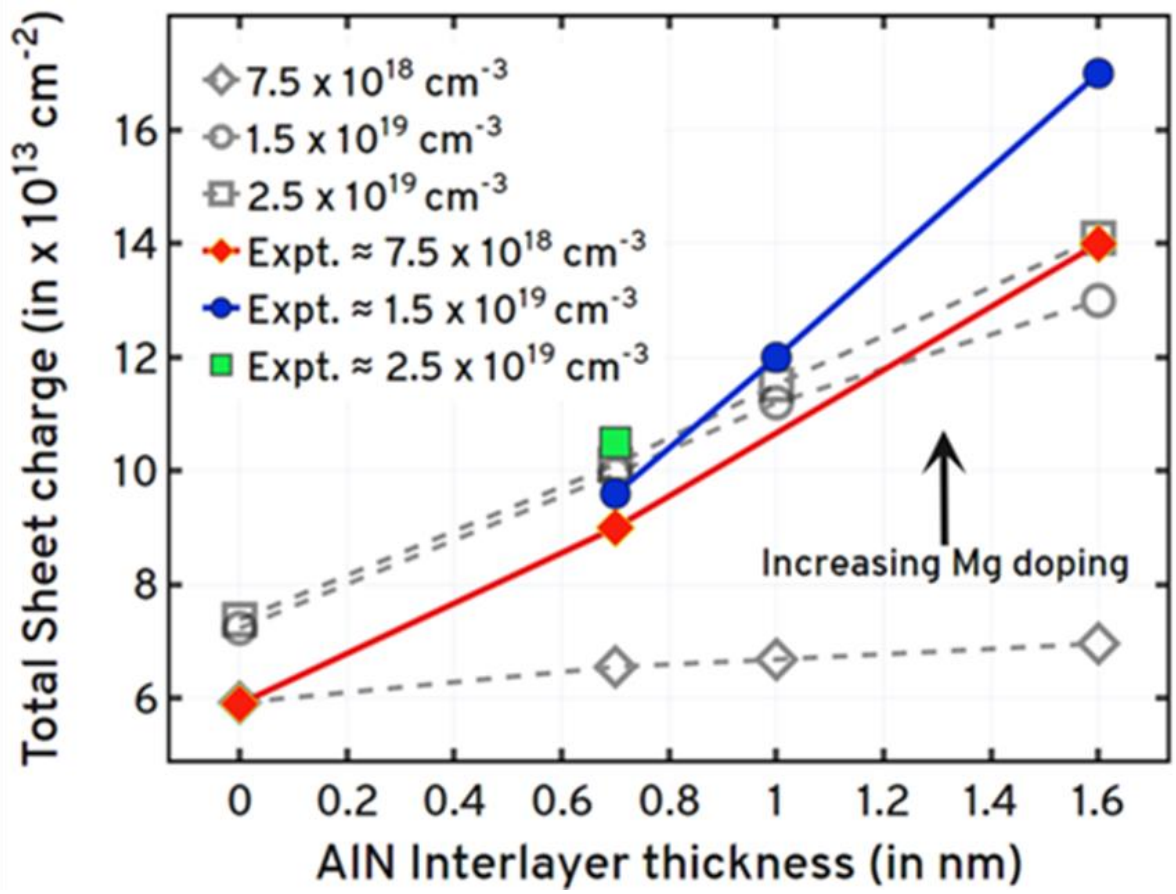

Figure 4.3 Total sheet charge as a function of AlN interlayer thickness for p-type modulation doped GaN/AlN/AlGaN SL samples presented in this chapter. This includes simulated values (in gray, dotted lines) and the experimental data (solid lines). When the samples have low Mg doping, or when the AlN interlayer thickness is high, the total sheet charge obtained via measurements is much higher than that obtained by simulations (in some cases even higher than Mg dopants in the samples).

C. Previous studies on traps at polarization interfaces

Before we delve into the details of the methodology used to hypothesize and prove the existence of the acceptor-like traps at the positive polarization interfaces in p-type III-nitrides, it is beneficial to look back at some prior studies where interface and surface traps in III-nitrides have been investigated for their impact on electronics, and to obtain charge balance in systems. Some of these studies include:

(i) Source of electrons in low-doped systems [79]:

Studies by J. Ibbetson, et. al., at UCSB in 2000 identified that the surface states centered around 1.65eV are the source of the electrons in the two-dimensional electron gas (2DEG) in AlGaN/GaN HEMT systems for an Al composition of 34%. And these formed only when the undoped AlGaN barrier thickness exceeded a certain critical thickness. Figure 4.4 illustrates the band-diagram for this surface donor model. Theoretical models were developed, and calculations were carried out to find the critical thickness of the AlGaN barrier layer where the Fermi level pinned at the donor-trap and these traps act as the source of electrons in the 2DEG. Experimental results for undoped $Al_{0.34}Ga_{0.66}N$/GaN HEMTs agreed well with theory assuming a polarization charge = 1.53×10^{13} cm^{-2} and a level 1.65 eV below the conduction band edge, with density at least 1.13×10^{13} cm^{-2} and the critical thickness of the AlGaN barrier that led to the formation of the 2DEG formations was measured to be ~3.5nm.

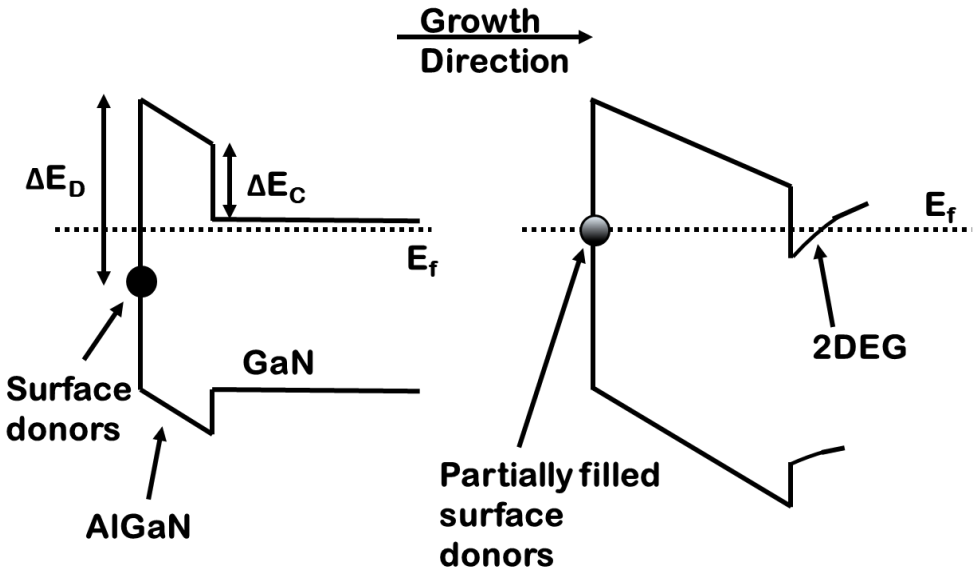

Figure 4.4 Schematic band-diagram illustrating the surface donor model with the undoped AlGaN barrier thickness less than (left) and greater than (right) the critical thickness for the formation of the 2DEG. E_f indicates the Fermi level, ΔE_C indicates the conduction band discontinuity, and ΔE_D indicates the location of the donor trap below the conduction band edge [79].

(b) Existence of donor trap at negative polarization interfaces in N-polar HEMTs:

Studies by Siddharth Rajan and A. Chini at UCSB showed the existence of a donor-like trap at the net negative polarization interfaces in N-polar HEMT structures [77]. These donor traps were then proposed as a mechanism for dispersion in these HEMTs.

Deep-level transient spectroscopy (DLTS) measurements on N-polar and Ga-polar HEMT structures showed a donor-like state approximately 60meV from the valence band at GaN/AlGaN interfaces with negative polarization charge. Figure 4.5 shows N-polar HEMT structure used to explain this, along with the charge distributions in the structure with the indicated positive polarization interfaces.

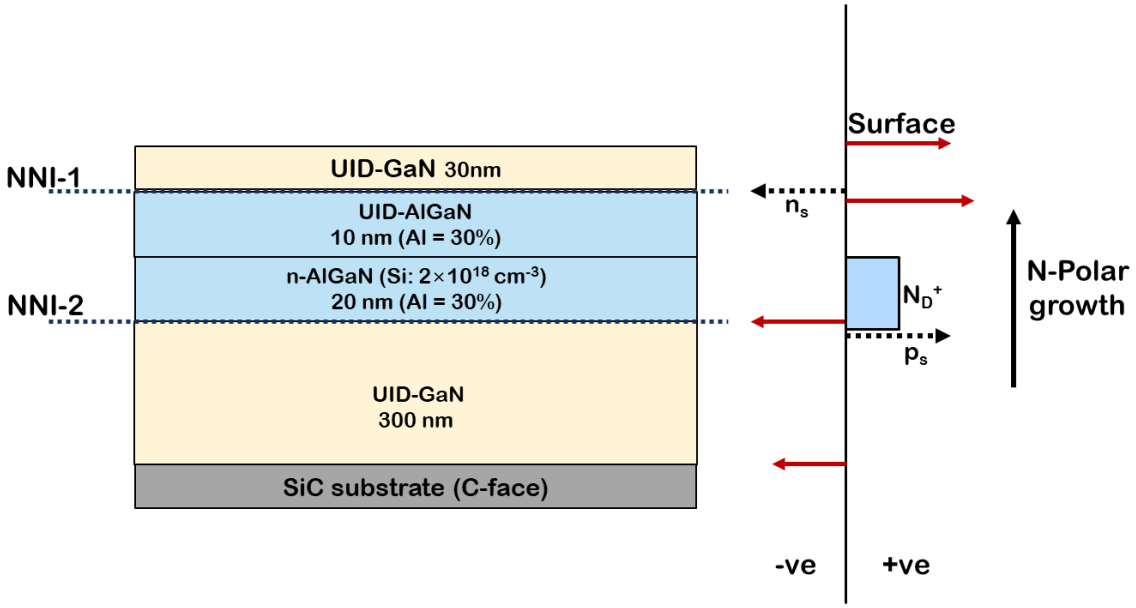

Figure 4.5 (left) Epitaxial layer structure of N-polar GaN/AlGaN/GaN HEMT grown on C-face SiC substrate. NNI-1 and NNI-2 indicate the net negative polarization interfaces in the structure. (right) Schematic of the various charges in the N-polar GaN/AlGaN/GaN HEMT used for the study.

Very recently, positron annihilation spectroscopy studies were used to investigate these structures, and the donor-like states were identified as nitrogen vacancies. Interfacial N vacancies with detrimental donor-like character were determined to be a universal feature in nitride semiconductor heterostructures at net-negative-polarization interfaces [78].

(c) Donor-like traps at net negative polarization interfaces in GaN/InGaN/GaN HEMTs:

Studies by Christopher Schaake, et. al, at UCSB showed similar donor trap states at the net-negative polarization interface of Ga-Polar GaN/InGaN/GaN heterostructures [80]. The energy level was found to have an activation energy of 0.071 eV in an undoped InGaN HEMT, extracted from DLTS measurements. The interface trap was proposed that it could act as a non-radiative recombination center in an InGaN LED by giving off energy from captured electrons as heat or phonons. Photo-assisted capacitance measurements were performed on InGaN diodes to calculate the density of this trap level. Using the density and energy level, a Schottky-Read-Hall (SRH) lifetime was estimated for varying electron densities. The lifetime was found to decrease at very high electron densities. Figure 4.6 shows the epitaxial structure, simulated band-diagram and the charge distribution for the sample used for that study [80].

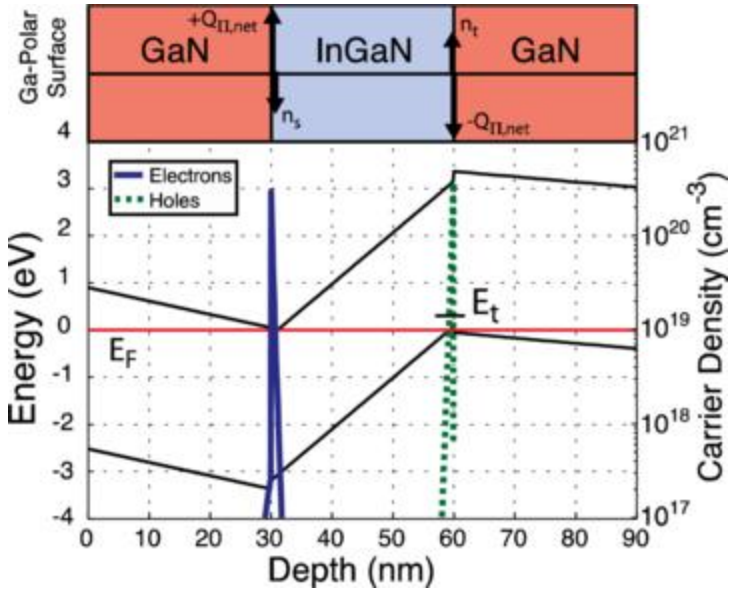

Figure 4.6 Simulated band diagram of an undoped InGaN HEMT showing a 2DEG at the top InGaN/GaN interface and 2DHG at the bottom InGaN/GaN interface with net negative polarization. The 2DHG was expected to be positively ionized traps. E_t indicates the donor-like trap level. [©2013 IOP Publishing. Reproduced with permission. All rights reserved]

D. Acceptor traps at positive polarization interfaces in p-type III-nitrides

Coming back to the N-polar p-type modulation doped GaN/AlN/AlGaN SL samples presented in this work, when the measured sheet charge density of holes matches the simulated/expected density, the acceptor-like traps present at the positive polarization interfaces are above the Fermi level and are, therefore, unoccupied, and neutral, and thus, they do not impact the electrostatics of the system. The enhanced charge, beyond what is provided by the Mg doping, is observed when the energy bands of the structure drive the acceptor trap down toward the Fermi level, ionizing the trap as is explained in the description of our methodology in this section.

Charge balance at polarization interfaces is provided by either mobile charges or ionized traps. In n-type AlGaN/GaN HEMTs, the charge balance at the positive polarization interface is provided by mobile electrons. In the case of the p-type N-polar GaN/AlN/AlGaN SLs investigated in this work, we propose that acceptor traps present at the positive polarization interfaces can provide the necessary charge balance. In the experiment described, acceptor traps were, therefore, assumed to exist at the AlGaN/GaN interfaces and the AlN/AlGaN interfaces and the purpose of the experiment was to verify their existence and extract the trap energy.

Figure 4.7 shows a representative valence band diagram for the structures described in this work where we assume no curvature in the bands (no or low Mg doping) for descriptive simplicity, and to develop the model. The two positive polarization interfaces— AlGaN/AlN and AlGaN/GaN—are also indicated in the figure. The accurate band diagrams for a representative series (calculated using Silvaco) are presented later in this section.

Figure 4.7 Schematic valence band-diagram of a p-type AlN/AlGaN/GaN SL to elucidate the existence of an acceptor trap. This valence band diagram is representative of a low-doped sample. E_t is the proposed interfacial acceptor-like trap level. The arrows from E_t indicate how the trap energy follows the band bending and are given as guide for the eye. $\Delta E_{(AlN)}$ refers to band bending in the AlN layer at the AlGaN/AlN interface, and $\Delta E_{(GaN)}$ refers to band bending in the GaN layer at the AlGaN/GaN interface. The dotted lines indicate the two positive polarization interfaces in this case – PPI-1 (AlN/AlGaN) and PPI-2 (AlGaN/GaN).

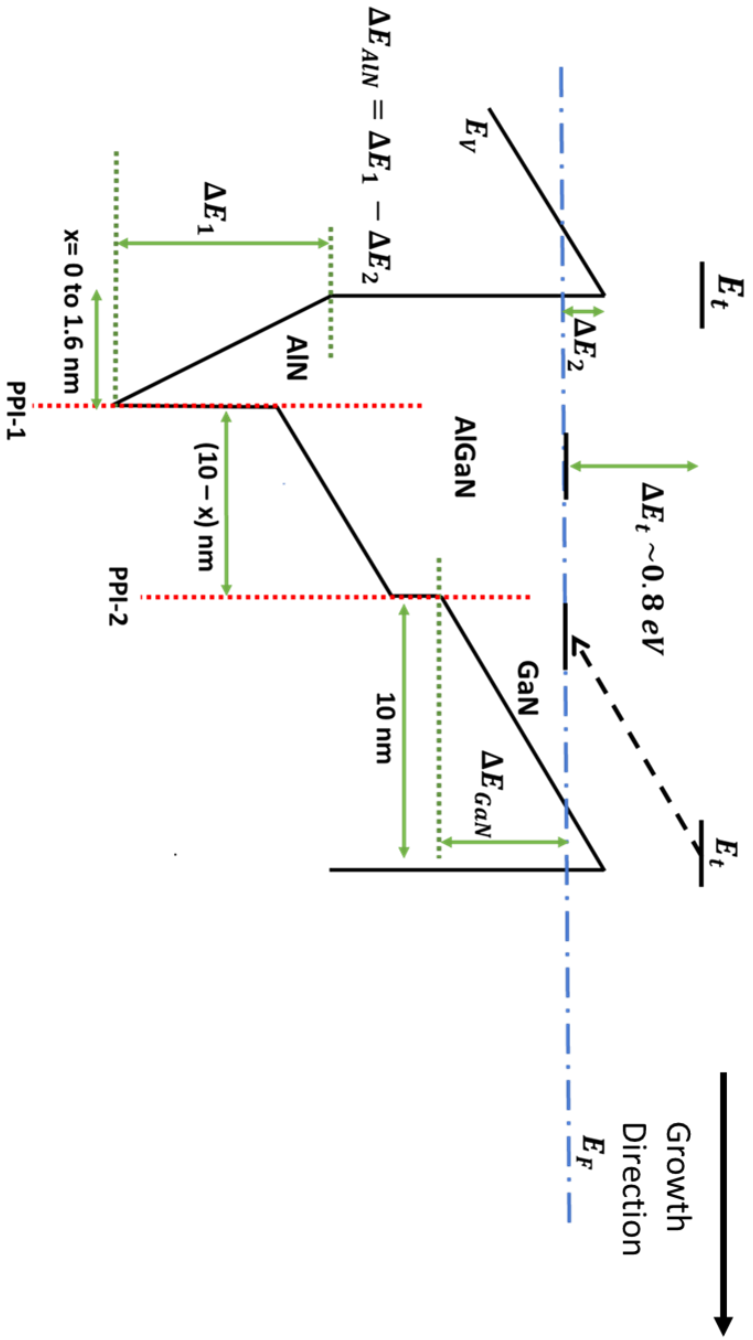

Acceptor traps are well known and documented in bulk GaN (an example being the yellow level). [81-86] The interfacial acceptor trap is placed at an energy level E_t above the GaN valence band as highlighted in Figure. 4.7, and at a level corresponding to the yellow-level in GaN. The trap being deep is referenced to the vacuum level, and its position at every interface is derived from the band bending in the structure. The dashed lines are given as guides for the eye to illustrate how the trap energy
follows the band bending. This is not meant to imply that the traps exist within the bulk of the component layers, at least not at the high concentration levels that they exist at the interfaces.

To explain our model, we choose two samples (from Figure 4.3), both with a Mg doping of 1.5×10^{19} cm^{-3} – and we call them, sample A—with an AlN interlayer thickness of 0.7 nm in each SL and—sample B—with an AlN interlayer thickness of 1 nm in each SL. These representative samples are chosen such that the measured hole concentration in sample A matches with the calculated and simulated values, whereas in sample B, the hole concentration is higher, but still close to the calculated values. According to our hypothesis, sample B is the structure where the trap level E_t drops in energy and just cuts the Fermi level, enabling it to be partly ionized, as illustrated in Fig. 4.7. The ionization fraction of the trap provides the small excess concentration of holes measured beyond the Mg concentration and the simulated value.

We next calculated the energy band diagrams for different Mg doping levels in the absence of traps using STR-FETIS . The band bending in AlN and GaN, $\Delta E_{(AlN)}$, and $\Delta E_{(GaN)}$, derived from the simulations as a function of the Mg doping level is illustrated in Figure. 4.8. The band bending for samples A and B is also shown in Figure 4.8. We

recognize that for sample B, the drop in E_t due to band bending is ~0.8 eV. In order for our hypothesis of the commencement of ionization of the trap in this sample to hold true, we place the trap level at ~0.8 eV above the valence band of GaN, at the AlN/AlGaN, and the AlGaN/GaN interface.

This is very close in energy to the yellow level in GaN [81-85], and we hypothesize that it may be of a similar nature, if not the same trap, enhanced in concentration at the heterojunction interface. While the yellow level in GaN has been attributed to carbon, the carbon concentrations in the N-polar GaN and $Al_{0.2}Ga_{0.8}N$ layers determined by SIMS were 1.2×10^{16} cm^{-3} and 2×10^{17} cm^{-3}, respectively, too low to account for the trap [70]. There are, however, studies that provide evidence of Ga-vacancies and vacancy-impurity complexes that form at energy levels close to 0.8 eV above the valence band [85,87-90].

Typically, Ga-vacancies do not form in p-type GaN, but polarization interfaces may allow their formation as opposed to bulk GaN. This is similar to studies on n-type GaN, where N-vacancies typically do not form, but exist in large concentrations forming a donor trap at the negative polarization interface (AlGaN/GaN) as has been shown using positron annihilation spectroscopy techniques [78]. Since ΔE_1 (from Figure 4.6) is calculated to be ~0.1 eV, it is much smaller than other energies of relevance in the band diagram and was, therefore, neglected for simplicity, and the purpose of the explanation. We assert that if this one acceptor-like trap successfully explains the higher charge obtained for a variety of structures, it is universally present at positive polarization interfaces in p-type nitride semiconductors. Experiments in later sections of this chapter and Chapter 5 were designed to prove the previously mentioned statement.

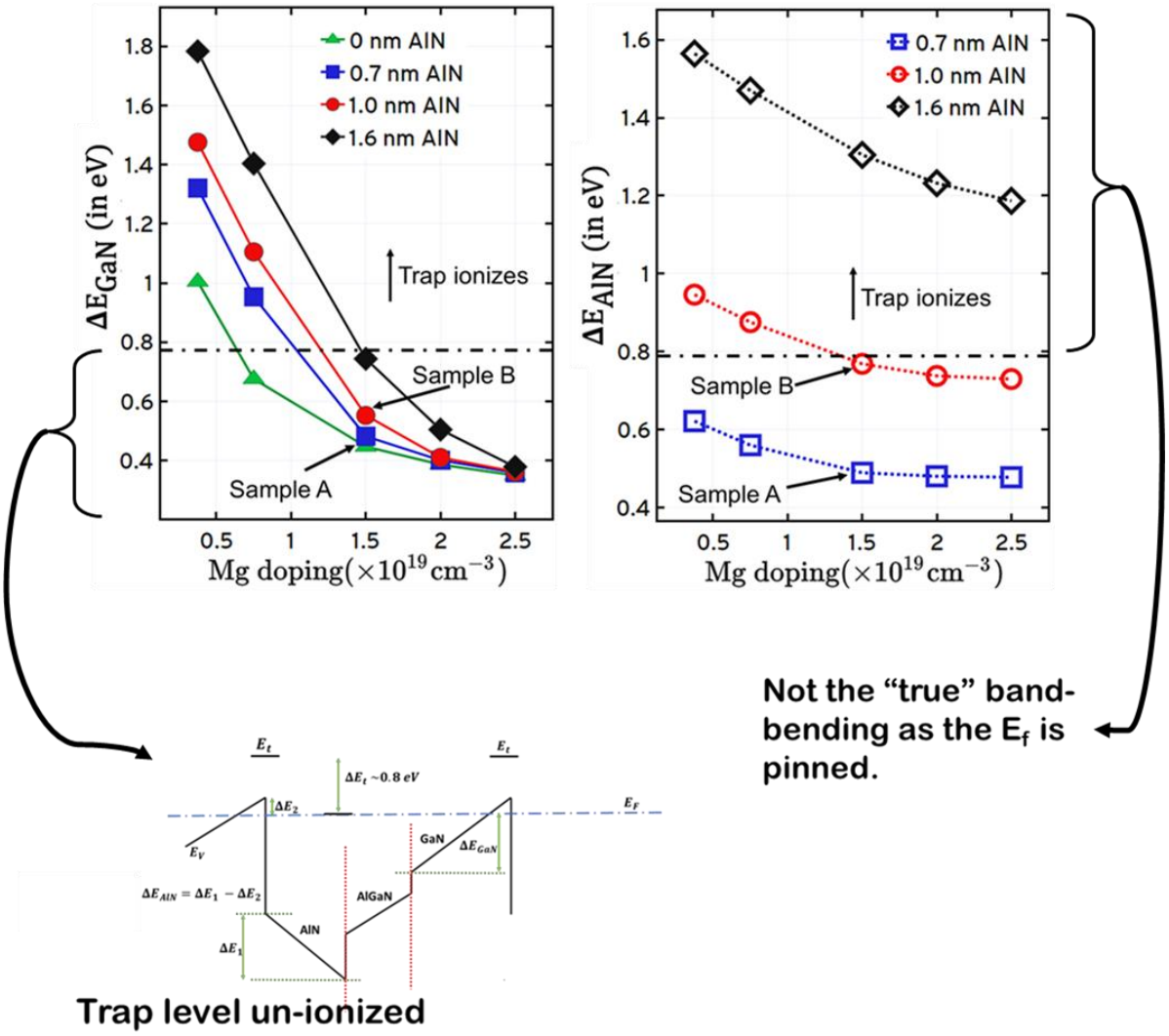

Figure 4.8 Energy band bending as a function of Mg doping in the samples for different AlN thicknesses, at both positive polarization interfaces. (left) The solid lines with filled symbols (triangle/square/circle/diamond) indicate band bending in GaN, $\Delta E_{(GaN)}$, and (right) the dotted lines with un-filled symbols indicate the band bending in AlN, $\Delta E_{(GaN)}$. The same symbols (square/circle/diamond) are used to indicate the two band bendings for the same sample. The legend indicates the AlN thickness used for each SL period, in the sample. Sample A (blue-filled square shape in the left figure) and sample B (red un-filled circle shape in the right figure) that have been chosen to explain our hypothesis are indicated in this figure. Refer to Fig. 4.7 for indications of the two positive polarization interfaces. The dotted horizontal line at 0.8 eV indicates the level of the proposed acceptor-like trap.

Figure 4.8 presents the simulated $\Delta E_{(AlN)}$ and $\Delta E_{(GaN)}$ values as a function of the Mg doping level for various AlN thicknesses in the SL for the samples in this study. The experimental results indicated that the samples, where either band-bending $\Delta E_{(AlN)}$ (band-bending in the AlN layer) or $\Delta E_{(GaN)}$ (band-bending in the GaN layer) was greater than 0.8 eV (highlighted by the dotted horizontal line), gave a higher measured total charge compared to simulations. We postulate that 0.8 eV is ΔE_t, the band bending that brings the acceptor trap at energy level E_t down to the Fermi level, enabling it to be ionized. Note that the values of ΔE provided by STR-FETIS are only valid below 0.8 eV. This model accurately shows us which samples will have more hole charges than predicted when E_f crosses E_t. Of course, once the traps ionize, the Fermi level is pinned at the trap and the band bending gets significantly modified. So, in reality, the band-bending is not >0.8eV, and the STR-FETIS model is just a method to pin-point which samples are predicted to have more holes measured than simulated, and hence have the acceptor-like traps at the positive polarization interfaces ionizing.

While Fig. 4.7 shows a representative valence band diagram for the structures described in this Chapter where we assumed no curvature in the bands (no or low Mg doping) for descriptive simplicity, more accurate simulations of the band diagram including traps at the interface were performed using the Silvaco software package (carried out by Aditya Raj). Figure 4.9 shows the calculated valence-band diagram for sample A, sample B, (and a third sample C with the same doping but a thicker AlN layer). For sample A, both the band bendings, $\Delta E_{(AlN)}$ and $\Delta E_{(GaN)}$, are less than 0.8 eV and the trap level E_t follows the band diagram and is 0.3 eV above the Fermi level at the positive polarization interfaces, and therefore, the acceptor-like trap does not ionize. In sample B, $\Delta E_{(GaN)} < 0.8$ eV, but $\Delta E_{(AlN)}$

~ 0.9 eV, and the trap level, Et, cuts the Fermi level and gets pinned. In sample C, both the band-bendings are greater than 0.8eV (from Figure 4.8 without accounting for traps), and hence in this case, the acceptor-like traps at both the positive polarization interfaces are ionized. The trap level, Et, cuts the Fermi level and gets pinned, in reality, as shown in Figure 4.9.

Figure 4.9 Actual simulated valence band diagram using Silvaco package, accounting for acceptor-like traps at positive polarization interfaces for (a) sample A, (b) sample B, and (c) sample with Mg doping of 1.5×10^{19} cm^{-3} and AlN layer thickness of 1.6 nm. In sample A, both band bendings, $\Delta E_{(AlN)}$ and $\Delta E_{(GaN)}$, are less than 0.8 eV. In sample B, $\Delta E_{(GaN)}$ is less than 0.8 eV, but $\Delta E_{(AlN)}$ is~0.9 eV, and so the acceptor-like trap ionizes. In (c), $\Delta E_{(AlN)}$ is ~1.3 eV (from STR-FETIS), and so the acceptor-like trap ionizes. This shows that the trap hypothesis mentioned in this chapter holds. The trap level, Et, is also indicated in the figure. (*figure continued onto next page*)

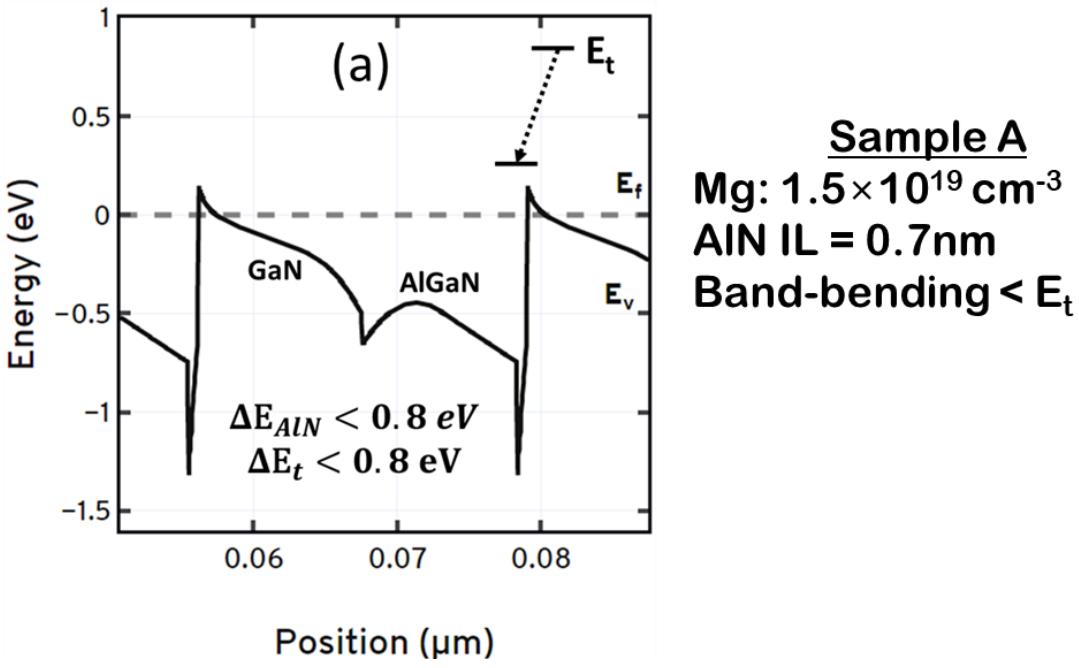

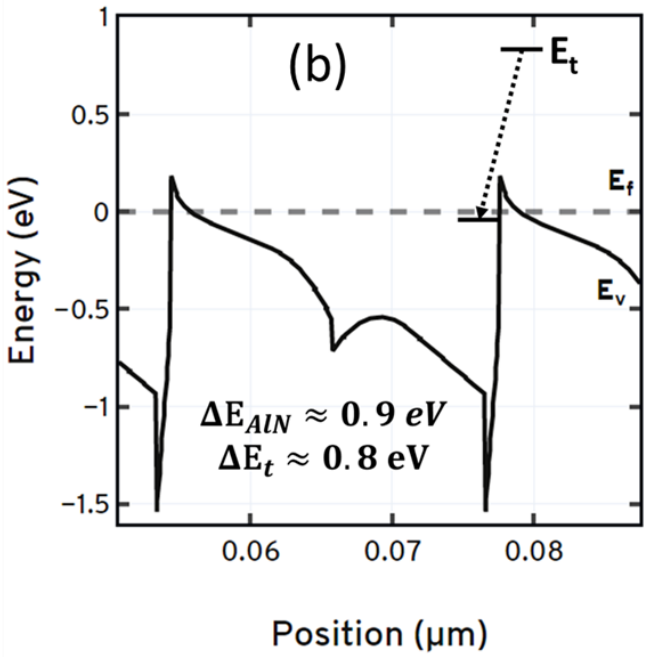

Sample B

Mg: 1.5×10^{19} cm^{-3}
AlN IL = 1.0nm
Band-bending ~ E_t

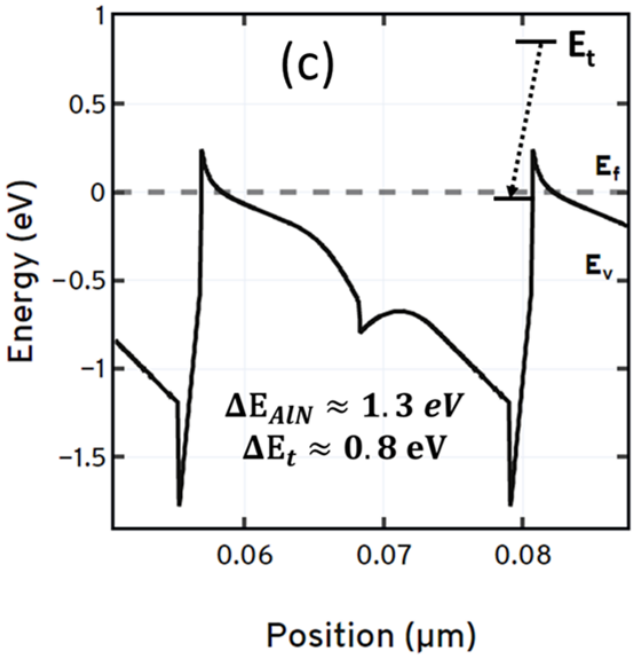

Sample C

Mg: 1.5×10^{19} cm^{-3}
AlN IL = 1.6nm
Band-bending >>E_t
(in the absence of traps) – but pinned, in actuality, by the trap

Figure 4.10 shows the difference between the simulated and the measured values of total sheet charge (in percentage) as a function of the AlN interlayer thickness for two cases. First case assumes that there were no acceptor-like traps, and the second case (simulated using Silvaco) places an acceptor-like trap with a density of 1×10^{13} cm^{-2} at each positive polarization interface (at 0.8 eV above the valence band of GaN). It is observed that when traps are introduced in the simulations, there is substantial agreement between simulations and experimental data. As shown in Figure 4.10, although the difference between the hole density and the Mg concentration for samples with 7.5×10^{18} cm^{-3} doping does not get fully resolved in our model, the difference is substantially reduced. The data point with 0.7nm AlN IL has the difference decrease from 30% to 16%, and the data point with 1.6nm AlN IL has the difference decrease from 50% to 18%. One other observation is that the ionization of traps increases with reduced Mg doping. In contrast, for samples where the band-bendings were less than 0.8 eV, there was good agreement between the measured and calculated values.

These simulations coupled with experimental measurements show evidence of acceptor-like traps of very high density existing at the positive polarization interfaces in p-type nitride semiconductors. While previous studies have shown the presence of donor-like traps at negative polarization interfaces, this work suggests the existence of a complementary acceptor-like trap at positive polarization interfaces in p-type III-nitrides, an important discovery. These traps serve as the source of charge balance in p-type nitride semiconductor samples with hole densities greater than the Mg doping [91]. For our model, we have used only one trap level at 0.8 eV, but in actuality, the trap may be a limited distribution or multiple levels around 0.8 eV. For this work, we used the one trap model for its simplicity as

it showed a very high degree of agreement between the experimental and simulation data. Further studies are needed to determine the nature of the acceptor-like trap, the variation of the magnitude and distribution of the acceptor-like traps at each individual positive polarization interface, and their contributions to the total excess charges measured.

Figure 4.10 Difference in the sheet charge between measured and simulated values (in percentage) as a function of AlN interlayer thickness for samples with different Mg doping values, without invoking the acceptor-like trap hypothesis (above) and invoking the acceptor-like trap hypothesis (below). Introducing acceptor-like traps of $1\times10^{13}cm^{-2}$ at the positive polarization interfaces allows for a substantial agreement of simulated and measured values. (*figure continues into the next page)*

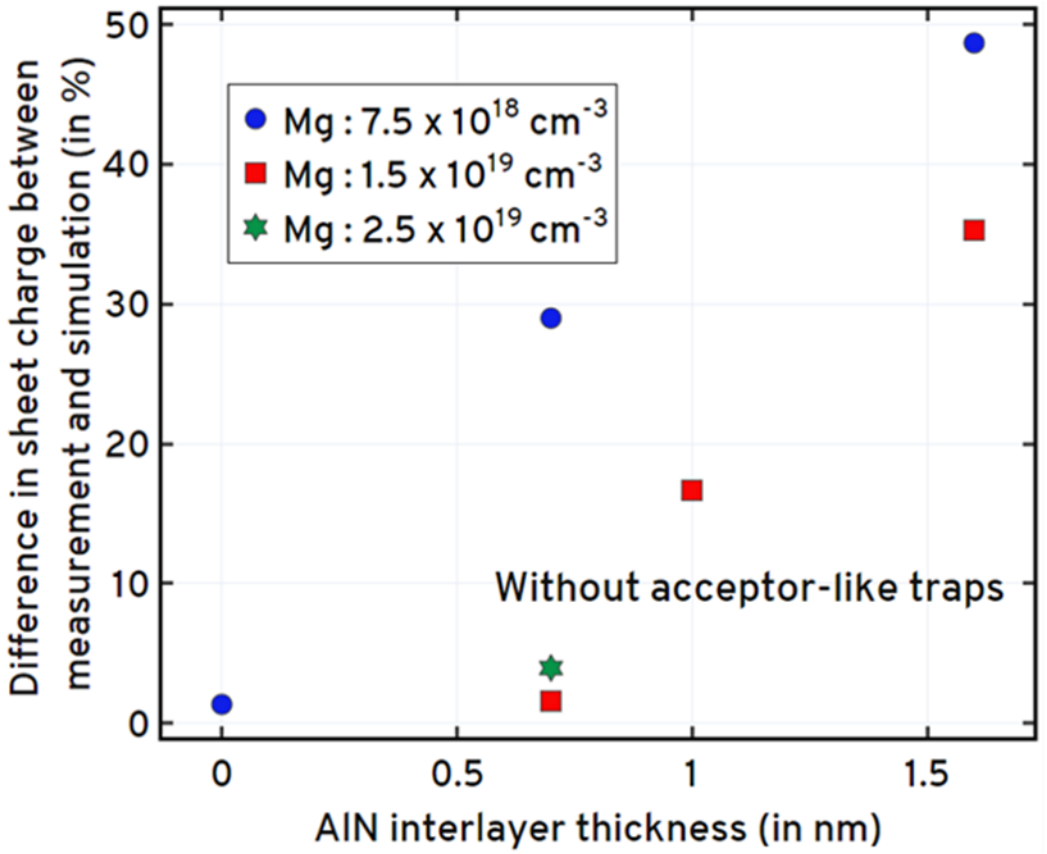

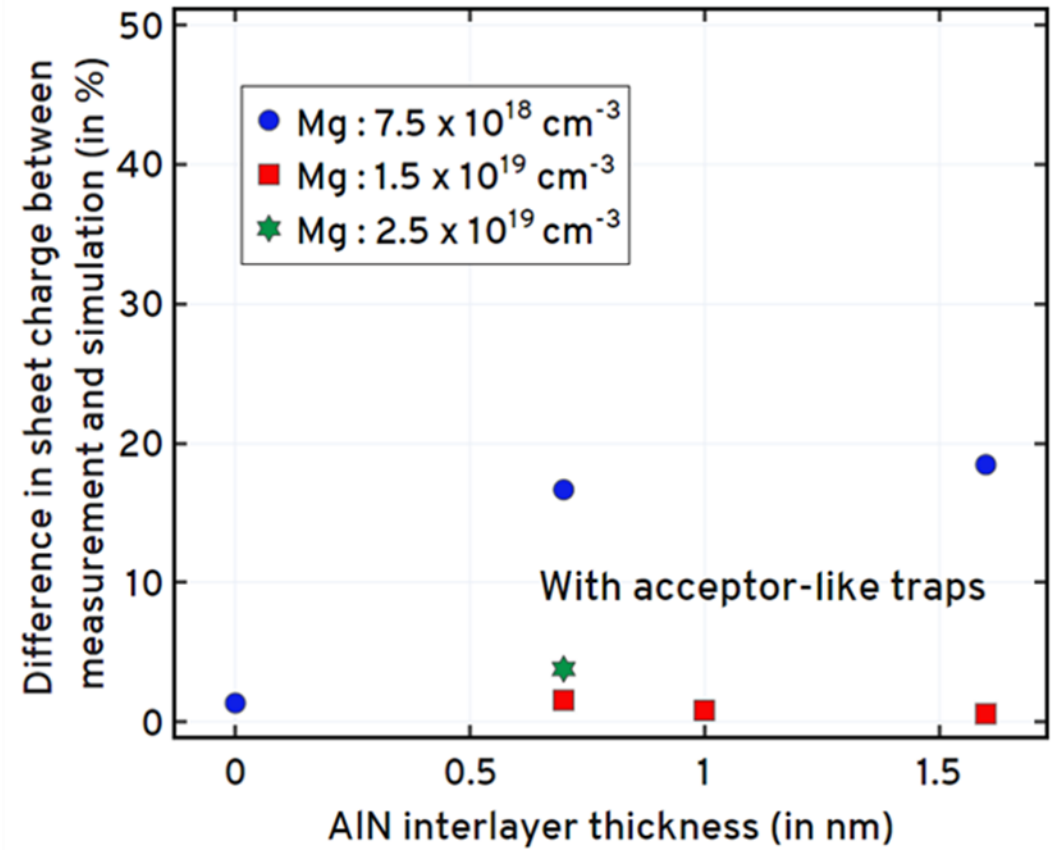

E. Explanation of trends in measured hole mobility

The hypothesis till now is that acceptor-like traps exist at 0.8eV above the valence band of GaN, at positive polarization interfaces, in p-type III-nitride systems. When either band-bending (AlN or GaN) hits 0.8eV, the acceptor traps ionize, and the Fermi level is pinned, thus explaining the high charge (more than the doping provided) in systems with low Mg doping, and/or thicker AlN IL. The use of AlN interlayer in the p-type N-Polar SL samples was to mitigate the effects of alloy scattering in the GaN/AlGaN SL and increase the mobility of holes. But it was observed that the effective mass of heavy-holes in III-nitrides is very high, and hence remains the dominating factor in the reduced mobility of holes in this materials system [92-94]. While we have explained the high hole charge, there is an

underlying trend in the measured hole mobility due to these acceptor-like traps, which we have not touched upon yet.

Referring back to Figure 4.7, The acceptor traps at the positive polarization interfaces, which we label as PPI-1 (AlN/AlGaN) – which is 0 to 1.6 nm away from the 2DHG and PPI-2 (AlGaN/GaN)- which is ~10nm away from the 2DHG are expected to be the major causes of scattering and mobility reduction in the samples. Acceptor traps at PPI-1 which is closer to the 2DHG is expected to cause higher degree of scattering and reduction of mobility compared to the traps at PPI-2. Figure 4.11 shows the measured total sheet charge concentration and mobility as a function of the AlN layer thickness for various Mg dopings used. A low sheet resistance (~1.5 kΩ/sq) was observed for N-polar modulation doped GaN/AlN/AlGaN SLs, where only one or both trap states were ionized [95]. Figure 4.12 and Table 4.1 indicate which of the samples in the series had acceptor traps at the PPI ionized along with the interface where the traps ionized.

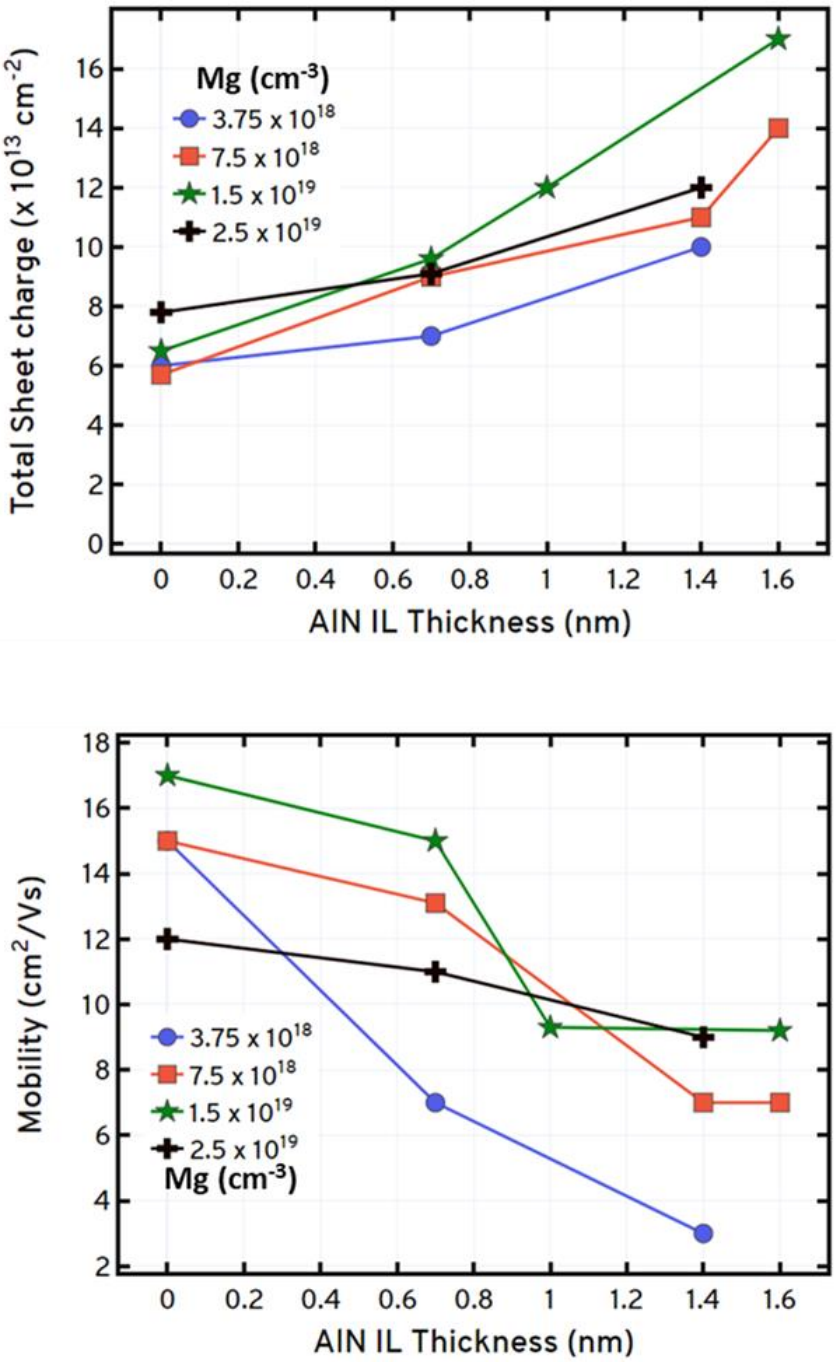

Figure 4.11 Room temperature Hall measurement results indicating the total hole sheet charge (above) and mobility (below) as a function of the AlN interlayer thickness for various Mg doping varying from 3.75×10^{18} to 2.5×10^{19} cm^{-3}.

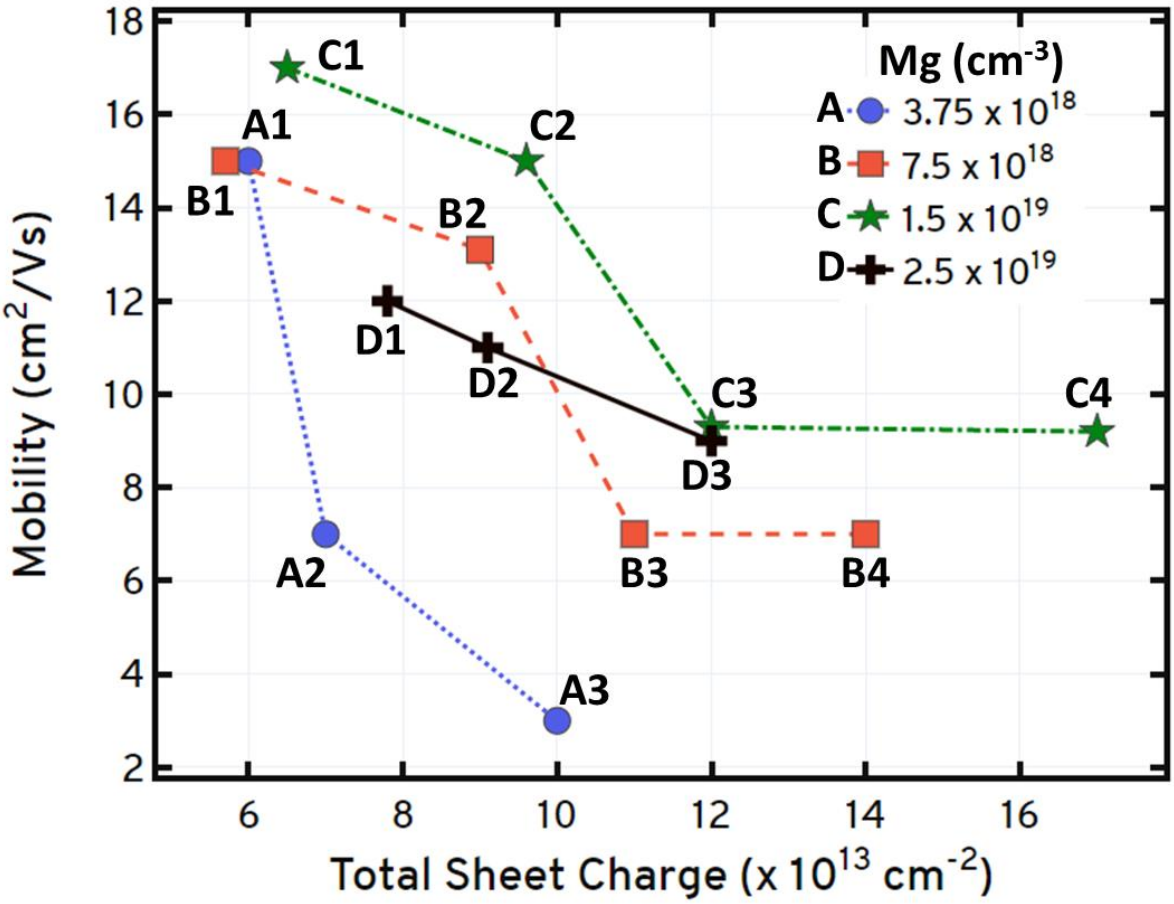

Figure 4.12 Measured mobility plotted as a function of the measured total sheet charge for various Mg doping varying from 3.75×10^{18} to 2.5×10^{19} cm^{-3}. The samples are labeled from A1 to D3, corresponding to Table I, which indicates the polarization interface at which the traps are ionized along with the effect of these traps on the measured mobility. This figure is a guide for the reader to see which samples' mobility drastically decreases when the traps at PPI-1 (the interface closer to the 2DHG) get ionized.

Table 4.1 Samples from the study labeled from A1 to D3 while the latter indicates the Mg doping series, and the number indicates the AlN thickness series within each doping series. The table indicates if the acceptor traps ionize at PPI-1 (AlN/AlGaN interface) or PPI-2 (AlGaN/GaN interface), or both. It also indicates if the mobility is affected (Δ >4cm^2/Vs) by the ionization of these traps. When both the traps are un-ionized, then "-" is indicated to show that the acceptor traps are un-ionized and, hence, do not affect the mobility.

S. No	Doping ($\times 10^{18}$ cm^{-3})	AlN layer (nm)	PPI-1 ionized?	PPI-2 ionized?	μ_p affected by traps?
A1	3.75	0	No	Yes	NO
A2	3.75	0.7	Yes	Yes	YES
A3	3.75	1.4	Yes	Yes	YES
B1	7.5	0	No	No	-
B2	7.5	0.7	No	Yes	NO
B3	7.5	1.4	Yes	Yes	YES
B4	7.5	1.6	Yes	Yes	YES
C1	15	0	No	No	-
C2	15	0.7	No	No	-
C3	15	1.0	Yes	No	YES
C4	15	1.6	Yes	Yes	YES
D1	25	0	No	No	-
D2	25	0.7	No	No	-
D3	25	1.4	Yes	No	YES

For the samples in this study, as shown in Figure 4.7, the 2DHG exists at the GaN/AlN interface or a GaN/AlGaN interface, if no AlN present (AlN thickness= 0nm in Table 4.1). It was observed for each of the AlN thickness series (with various Mg doping levels) the hole mobility, μ_p decreased in samples where the acceptor traps ionized. It was further observed within those set of samples that μ_p decreased to a great extent (>50% decrease) for those samples where AlN band-bending was ≥ 0.8eV independent of the GaN band-bending in the same sample. The 2DHG is closer to the AlN/AlGaN PPI (PPI-1) (0–1.6 nm) compared to the AlGaN/GaN PPI (PPI-2)(10 nm). Therefore, the more dominant source of scattering (and, hence, the cause of the decreased mobility) is the ionized acceptor traps, which exist at the AlN/AlGaN PPI, the interface closer to the 2DHG. While the ionized traps at the AlGaN/GaN interface also cause scattering, their effect is not as pronounced because they are far away from the 2DHG. This explains the higher mobility observed in samples, where only the GaN band-bending was ≥0.8 eV, and the AlN band-bending was <0.8 eV leading to the ionization of traps at only the remote AlGaN/GaN PPI (PPI-2).

We have four different series from our measurements A–D based on the Mg doping in the sample. Within each of those series, we have varied the AlN interlayer thickness from 0 to 1.6 nm. Going through each series of samples one by one, the main takeaway is that—PPI1 (and, hence, AlN Band-bending) determines if the ionization of a trap reduces the hole mobility drastically—because of its proximity to the 2DHG (<1.6nm away) compared to PP2 (10nm away).

In **series A**, all the grown samples have the traps ionizing, but PPI1 (and PPI2) is active in samples A2 and A3, and hence, the drastic reduction in mobility can be seen going from A1 to A2 and A3.

In **series B**, B1 does not have any traps ionized, but B2 has only PPI2 ionized—there is a very negligible reduction in mobility (Δ≈1.5), which is caused due to an increase in the charge. B3 and B4 have both PPI1 and PPI2 ionized, and thus, we can see a drastic reduction in mobility going from B1 and B2 to B3 and B4.

In **series C**, C1, and C2 do not have any traps ionizing, and we do not observe any reduction in mobility due to traps. C3 has PPI1 ionized, but not PPI2, and we see a drastic reduction in mobility, which confirms our initial statement. C4 has both PPI1 and PPI2 active, and there is a drastic reduction in mobility from C1 to C2, but C4 and C3 have similar mobilities, which reiterates the dominant effect of PPI1.

In **series D**, D1 and D2 do not have any traps ionizing, but D3 has PPI1 active, which reduces its mobility.

F. Ionizing the acceptor traps without AlN IL

Another set of experiments were then conducted to explore if the acceptor-like traps could be ionized without any AlN in the samples. Figure 4.13 shows the epitaxial structures grown for this study, and Figure 4.14 shows a representative band-diagram with the location of the 2DHG and the positive polarization interface (PPI) indicated. N-Polar modulation doped GaN/AlGaN seven-period SL stacks were grown. In this case, there is only one PPI—at the AlGaN/GaN interface 10 nm away from the 2DHG in the samples. The series we held the Mg doping constant (Mg:7.5×10^{18} cm^{-3}), Al% was varied from 15% to 45%, and then room-temperature Hall measurements were carried out on all the samples.

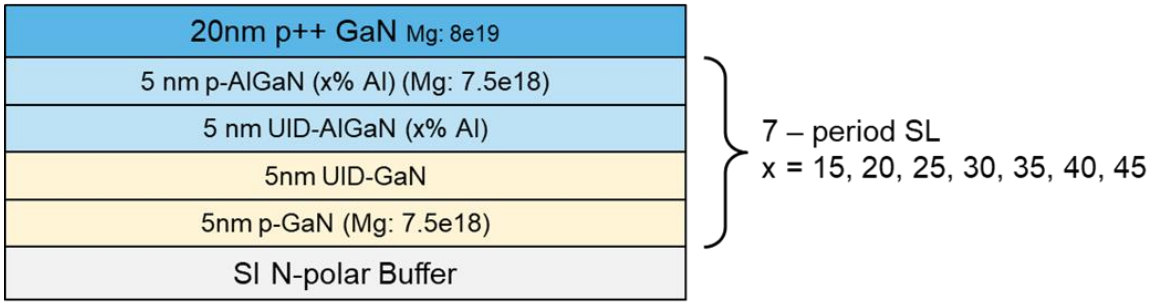

Figure 4.13 Schematic epitaxial structure of the grown N-polar modulation doped GaN/AlGaN superlattices with varied AlGaN % from 15% ≤ x ≤ 45%. The Mg doping was kept constant at 7.5×10^{18} cm^{-3}

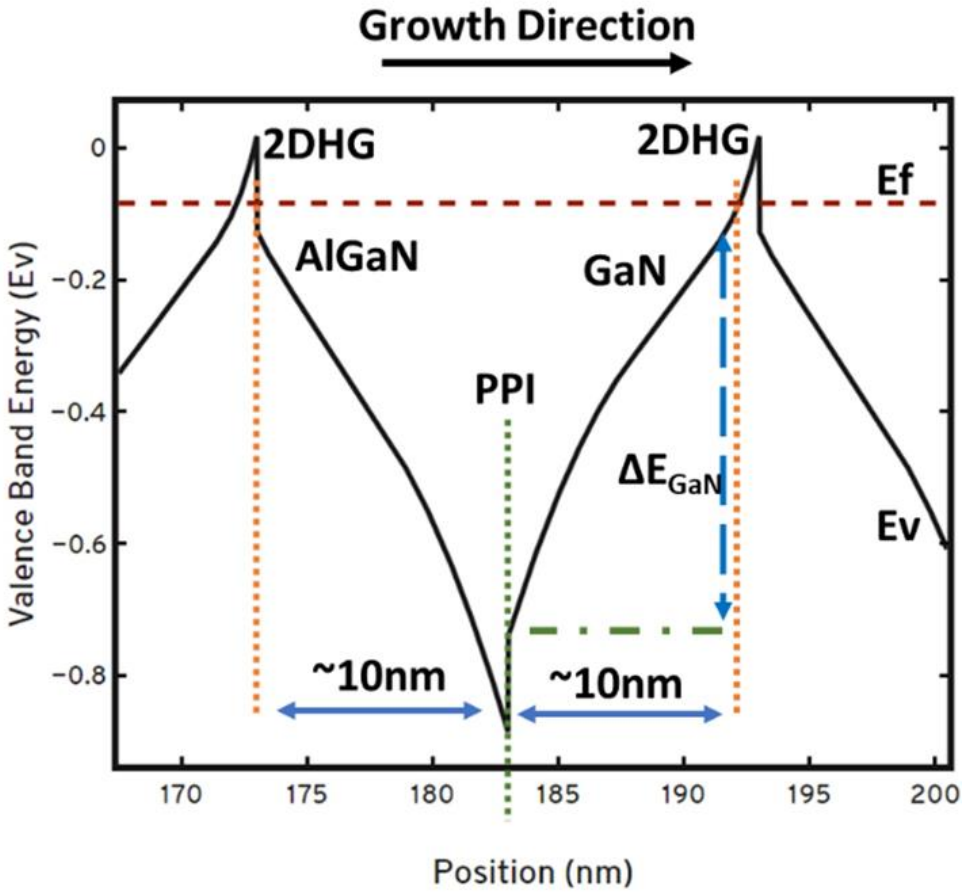

Figure 4.14 Representative schematic valence band energy diagram for a sample with Al%~25%. $\Delta E_{(GaN)}$ refers to band-bending in the GaN layer at the AlGaN/GaN interface. (In this representative valence band diagram, $\Delta E_{(GaN)}$ ~ 0.6 eV, and hence, the acceptor traps are not ionized for this sample.) PPI indicates the only positive polarization interface in the strucutre—AlGaN/GaN interface. The distance of PPI from the 2DHG is also indicated in the figure.

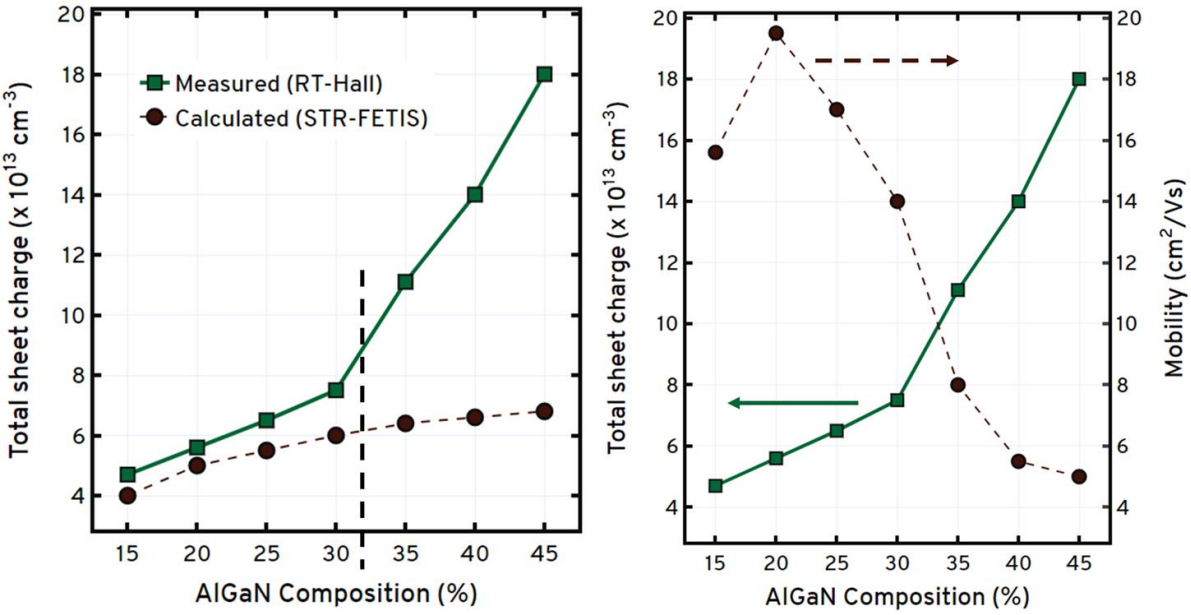

Figure 4.15 (left) Total sheet charge as a function of the Al% in the SL—measured from RT-Hall (in solid line) compared with calculated values (dotted line) from STR-FETIS simulations. The vertical dotted line indicates the Al% (32%) predicted from STR-FETIS where the acceptor traps will ionize at the positive polarization interface (PPI). Thus, we have all samples with Al%>32% showing a very high concentration of holes measured (even more than Mg put into the samples), and samples with Al% < 32% showing good agreement with the calculated values. (right) RT-Hall measurement results indicating the total sheet charge concentration of holes and the mobility as a function of the Al composition in the superlattice. Simulations are carried out without taking the effect of traps into account, and hence, we see that for Al% < 32 where the traps do not ionize at the PPI, there is agreement in the measured and calculated values and for samples with Al%>32%, since simulations are carried out without the existence of traps, and in reality, there is an ionization of traps, we see the discrepancy in the measured and calculated values.

A simulation study was first carried out using STR-FETIS to predict the Al composition when the acceptor traps would ionize (i.e., at what Al% would the GaN band bending ≥ 0.8eV), and it was determined to be Al% ≈ 32%. Figure 4.15 shows the room-temperature Hall measurements and compares the total sheet charge measured and calculated as a function of the Al% in the AlGaN layers. As predicted by the simulations, samples with Al% < 32% showed good agreement with the calculated total hole sheet charge, and samples with Al% > 32% showed more than double the calculated hole concentrations (even more

than the Mg dopants put into the samples). This can be attributed to the ionization of acceptor traps at the PPI, which act as the source of these excess holes.

Chapter 4 of this dissertation detailed the methodology behind the proposed acceptor-like traps at positive polarization interfaces in p-type III-nitride systems using the N-polar modulation doped GaN/AlN/AlGaN and GaN/AlGaN superlattices as the demonstration platform. The acceptor-traps were shown to be the major source of holes in p-type systems where they ionized, and they provided the required charge balance by helping reconcile the measured hole concentration with the calculated concentrations. Please refer to **Appendix A** for the complete details on the STR-FETIS model developed, and the methodology for counting the Mg dopants in the samples presented in this work. The acceptor traps also helped explain the measured mobility trends in the SL samples. The next chapter will detail a complementary Ga-Polar SL study to demonstrate the impact of these acceptor-like traps on the p-type III-nitride systems.

Chapter 5

Ga-Polar (AlGaN/AlN)/GaN SL - Universality of acceptor-like traps

---

A. Epitaxial Design, MOCVD Growth & Material Characterization

Chapter 4 introduced the existence of acceptor-like traps at the positive polarization interfaces (PPI), placed 0.8eV above the valence band of GaN, in N-polar p-type III-nitride systems. The ionization of this acceptor-like trap level was the main source of holes in systems which had insufficient or no Mg doping in them. This Chapter experimentally demonstrates the proposed presence and the effect of these acceptor traps on both the charge and the mobility of holes in the more conventional Ga-polar uniformly doped p-type (AlGaN/AlN)/GaN superlattices.

Ga-Polar uniformly doped SL samples were grown using Metalorganic Vapor Phase Epitaxy (MOVPE) technique at a temperature of 1155˚C and pressure of 100 torr on semi-insulating (SI) GaN buffer layer grown on c-plane sapphire with trimethylgallium (TMGa), trimethylaluminum (TMAl), cyclopentadienyl magnesium (Cp_2Mg), and NH_3 as precursors. Figure 1 shows the p-type uniformly doped Ga-polar (AlGaN/AlN)/GaN SL epitaxial

structure. Prior studies (described in Chapter 2 and 3) indicated that seven-period SL stacks resulted in reliable hall-effect measurements, and hence seven-period SL stacks were grown. As shown in Figure 5.1, each SL period in the stack was 20nm thick and was composed of (10-x) nm AlGaN:[Mg]/ x nm u.i.d. (unintentionally doped) AlN/ 10nm GaN:[Mg], where the AlN layer thickness, x, was varied from 0 nm $\leq$ x $\leq$ 1.6 nm. In addition, for each AlN thickness, the p-type Mg doping was varied from 3.75×10^{18} $cm^{-3} \leq [Mg] \leq 2.5\times10^{19}$ cm^{-3}. A 20nm p++ GaN contact layer, doped with 8×10^{19} cm^{-3} of Mg, was grown in-situ on the SL stack to facilitate fabrication of good contacts to the p-type SL. Before the growth of the SL layers, a 20 nm $Al_xGa_{(1-x)}N$:Mg was first grown on the SI buffer where the composition was graded from x = 0–12% to be used as the back barrier for hole transport (following the discussion in Chapter 2). From the study in N-polar systems described in Chapter 4, an Al composition in the AlGaN SL layers was chosen to be 24% for the present study as it was predicted to have a definitive signature of trap occupancy for the experimental series studied.

While the initial study used modulation doped N-polar SL samples grown in the -c or $(000\bar{1})$ direction, the present study uses the more widely used Ga-polar orientation for the samples reported. While N-polar orientation allows for modulation doping using MOVPE due to abrupt and sharper Mg doping profiles, Ga-polar orientation faces the problem of Mg diffusion during MOVPE growths (as detailed in Chapter 3) [69,70], and hence uniformly doped samples are presented in this Chapter.

Mg doping in the samples was calibrated using Secondary Ion Mass Spectroscopy (SIMS), and the composition and quality of the SL was determined using Atomic Force Microscopy (AFM) and X-Ray Diffraction (XRD). Figure 5.2 shows the 2θ-ω XRD spectra

for an AlN thickness series with Mg: 7.5×10^{18} cm^{-3}, and this also includes an inset with a representative AFM image of an as-grown sample used in the study. As Mg acceptors are passivated in the as-grown epitaxial material, Mg activation was carried out using rapid thermal annealing (RTA) for 3 mins at 825ºC and Pd/Au contacts were deposited to pre-pare the samples for room temperature Hall measurements (RT-Hall). Total sheet charge concentration of holes, and hole mobility were derived from RT-Hall, and these were compared with calculated values derived from STR-FETIS® software package.

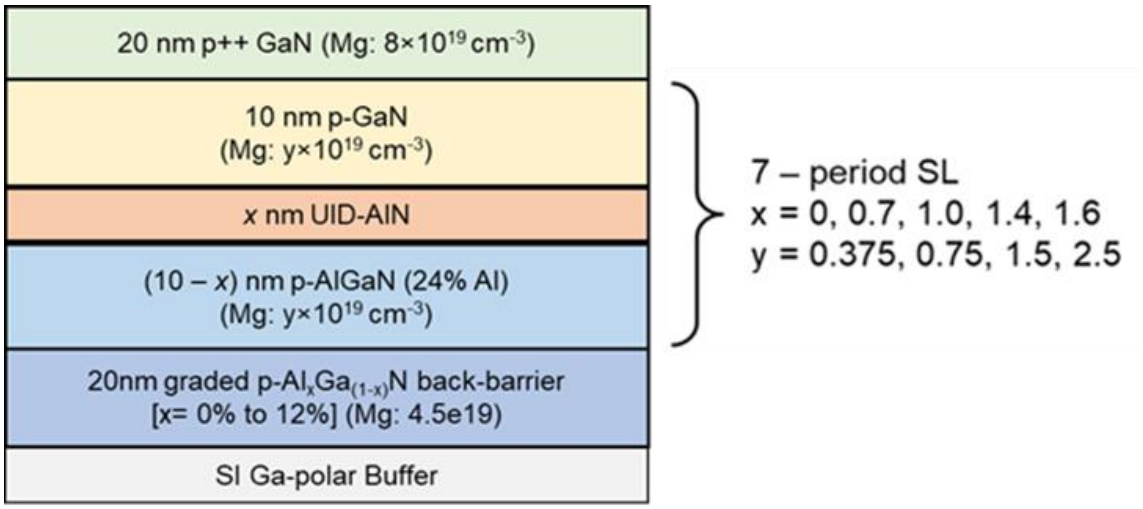

Figure 5.1 Structure of SL samples epitaxially grown using MOVPE for this work. Individual SL period had a thickness of 20nm and was composed of (10-x) nm p-AlGaN / x nm u.i.d. AlN/ 10 nm p-GaN, where, x, the AlN layer thickness was 0 nm ≤ x ≤ 1.6 nm. For each of AlN thickness series samples, the p-type doping (Mg) was varied from 3.75×10^{18} cm^{-3} ≤ [Mg]≤ 2.5×10^{19} cm^{-3}. A 20 nm p++ GaN contact layer was also grown in-situ to facilitate high quality contacts.

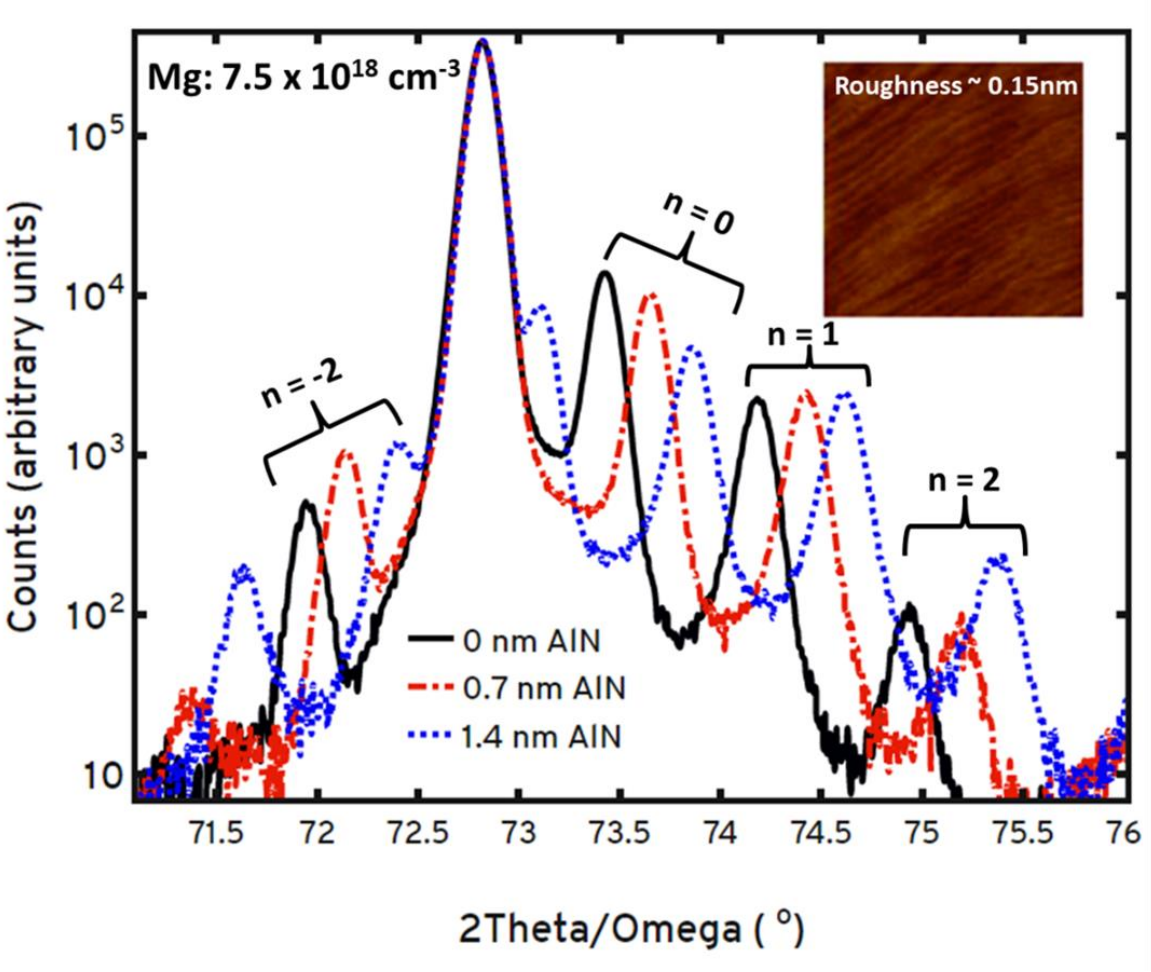

Figure 5.2 (2θ-ω) X-Ray Diffraction spectra for a sample series with varying AlN thickness from 0nm to 1.6nm with a Mg doping = 7.5×10^{18}cm^{-3} held constant. Insert: 5 µm × 5 µm Atomic force microscopy image with rms roughness= 0.15 nm of a representative sample reported in this chapter.

B. Explanation of high measured sheet charge

Four-probe Hall-effect measurements were carried out at room temperature (RT-Hall) (with the magnetic field strengths ranging from -6T to 6T) and the total sheet charge measured was compared to the simulated value calculated using STR-FETIS®. The total hole sheet charge concentration measured for varying AlN layer thickness and for the various p-type Mg doping used, is shown in Figure 5.3.

Figure 5.3 Results for Hall-effect measurements conducted at Room Temperature on samples presented in this work. The figure shows the total sheet charge concentration of holes measured as AlN layer thickness is varied, for the different Mg doping used at each AlN thickness

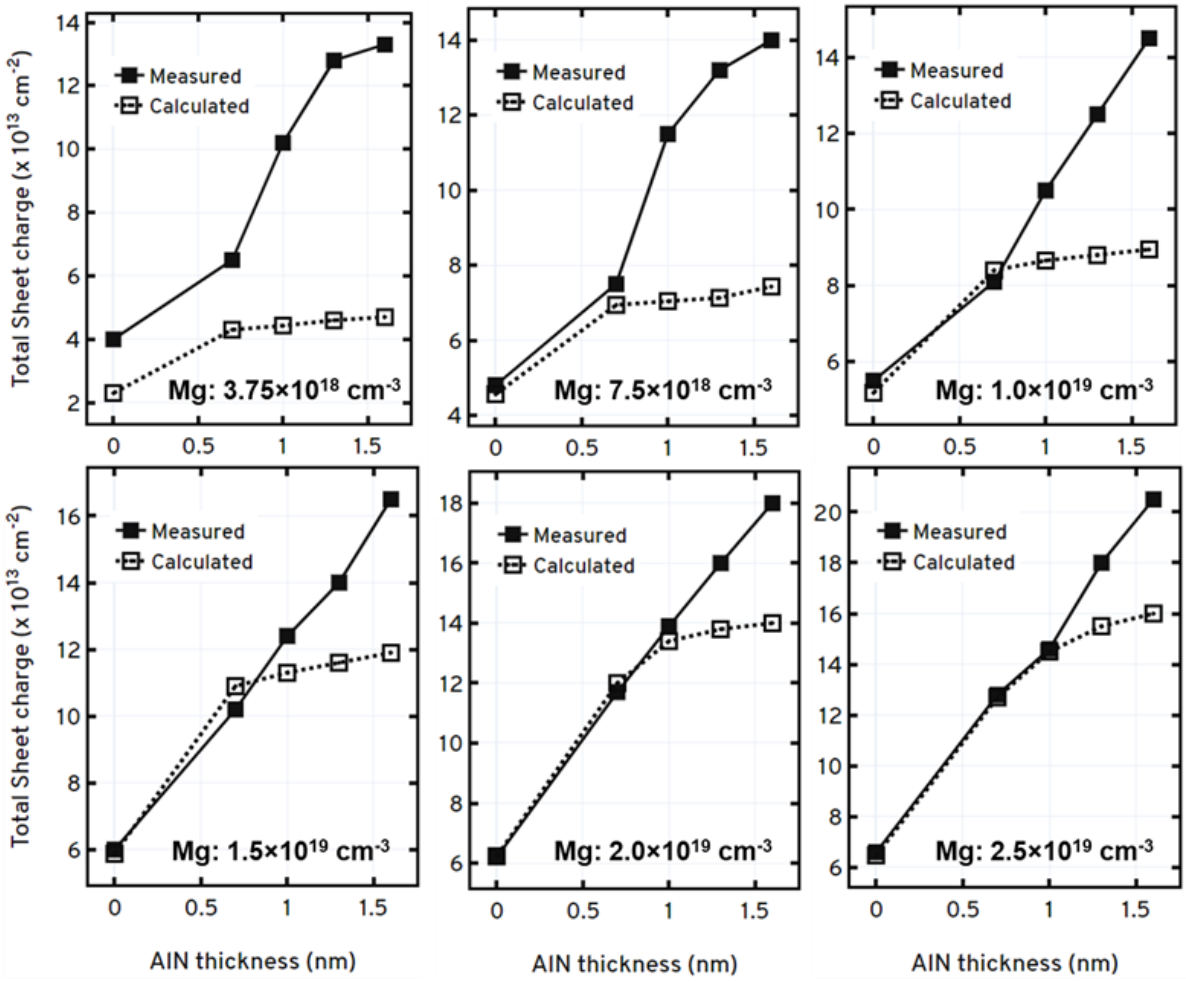

Figure 5.4 shows a cartoon schematic valence band energy diagram of a representative Ga-polar (AlGaN/AlN)/GaN SL structure, without Mg doping, which will be used to explain the trends in this section going ahead.

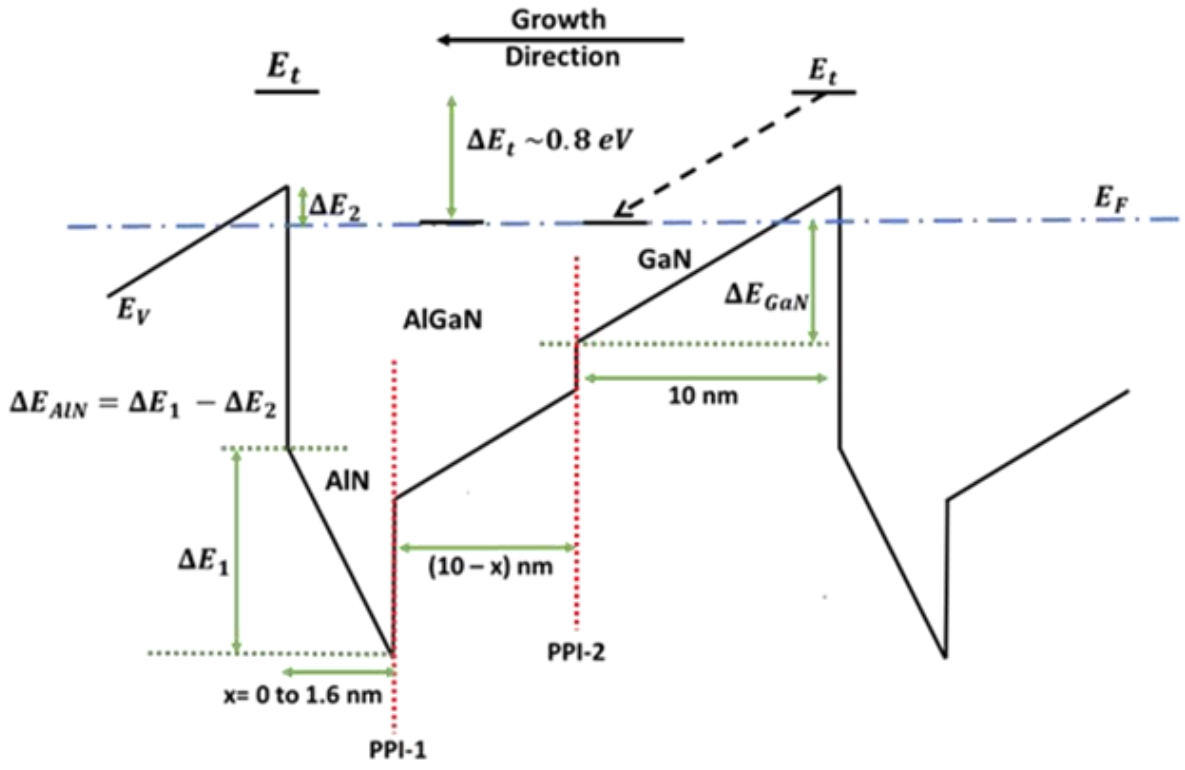

Figure 5.4 A model valence band-diagram schematic for a single p-type AlN/AlGaN/GaN SL period with very low Mg doping. E_t is the indicated acceptor trap level, with $\Delta E_t \sim 0.8$eV measured from the valence band (E_V) of GaN. The arrow from E_t indicate how the trap energy follows the band-bending and is just a guide to the eye. $\Delta E_{(AlN)} (= \Delta E_1 - \Delta E_2 \approx \Delta E_1)$ refers to band-bending in the AlN layer at the AlN/AlGaN interface and $\Delta E_{(GaN)}$ refers to band-bending in the GaN layer at the GaN/AlGaN interface. The vertical dotted lines indicate the two positive polarization interfaces (PPI), in this case – AlGaN/AlN (PPI-1) and GaN/AlGaN (PPI-2). The separation of these interfaces from the 2DHG is also shown in the diagram and we use the reduced impact of hole mobility of traps ionized at PPI-2 (relative to PPI1) because of the larger distance from the hole gas, to support the analysis.

As seen in Figure 5.3, in samples with lower Mg dopoing, and/or thicker AlN layer thickness, the observed concentration of holes exceeded that of the calculated hole concentration, and in some cases, even higher than dopants incorporated into the samples during growth. Following the methodology mentioned in Chapter 4, a proposed acceptor-like trap, 0.8eV above the valence band of GaN (also referenced in all instances to the vacuum level has been invoked) to resolve the presence of holes in excess of the Mg doping in the experiments. The level was chosen to be consistent with a Ga-vacancy and some of its complexes in GaN. The existence of bulk traps is not ruled out but the existence of a large concentration at positive polarization interfaces is proposed. When the band-bending of both GaN and AlN was < 0.8eV, the sheet charge concentration of holes (p_s) measured using RT-Hall matched with the calculated values, as can be seen in Figure 5.3. For those samples where band-bending of either GaN or AlN was ≥ 0.8eV (without accounting for the impact of trap ionization on band-bending), the measured p_s was greater than the amount of Mg dopants put into the sample during growth. This consistent measurement confirms that the excess holes originated from the acceptor traps at the positive polarization interfaces (PPI), here – AlGaN/AlN (PPI-1) and GaN/AlGaN (PPI-2) interfaces. The acceptor trap ionized when either band-bending was ≥ 0.8eV, and the Fermi level was consequently pinned at this trap level (= 0.8eV) leading to the very high measured p_s. Chapter 4 elucidates this excess hole charge with simulations and experimental demonstrations for N-polar modulation doped SLs, while the present study demonstrates the similar effect using the conventional Ga-polar uniformly doped p-type SLs, and hence shows that these acceptor-like traps at the PPI in the III-nitride systems are agnostic to both polarity and doping schemes used. Very

low sheet resistance (~3kΩ/sq) was observed for p-type Ga-polar uniformly doped AlGaN/AlN/GaN SLs, where trap states at only one or both interfaces were ionized.

C. Explanation of trends in measured hole mobility

The measured hole mobility at room temperature as a function of the AlN layer thickness for the different Mg doping levels presented in this work, is shown in Figure 5.5. Measured hole mobility as a function of measured total sheet charge for various Mg doping varying from 3.75×10^{18} cm^{-3} to 2.5×10^{19} cm^{-3}, is shown in Figure 5.6. And, the figure has samples labelled from A-1 through F-5, corresponding to Table 5.1.

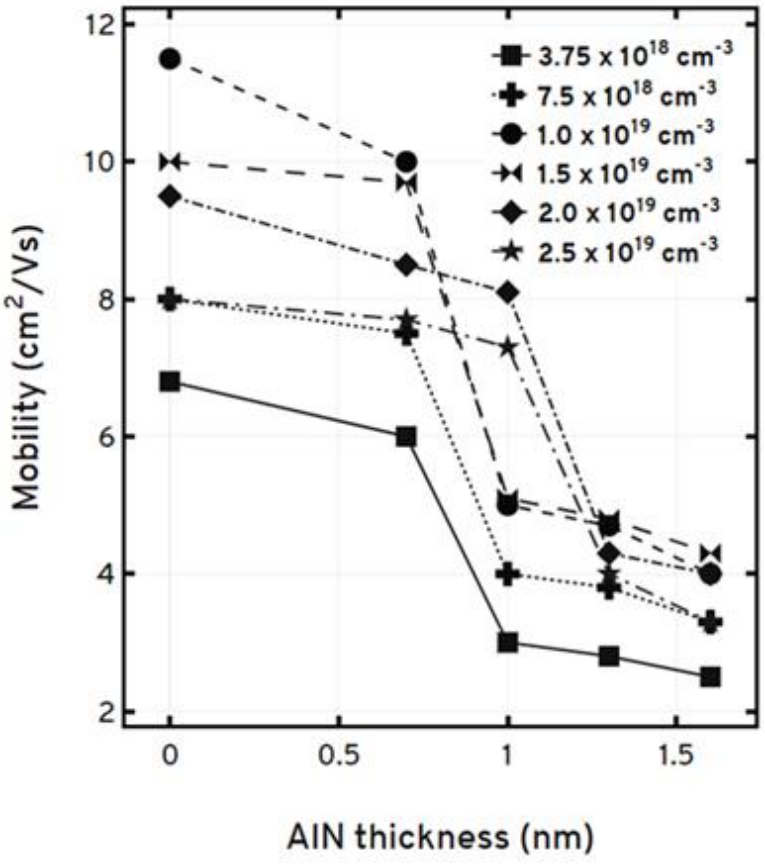

Figure 5.5 Room temperature Hall measurement results for samples presented in this work. This figure shows measured hole-mobility as AlN layer thickness is varied, for the different Mg-doping used at each AlN thickness.

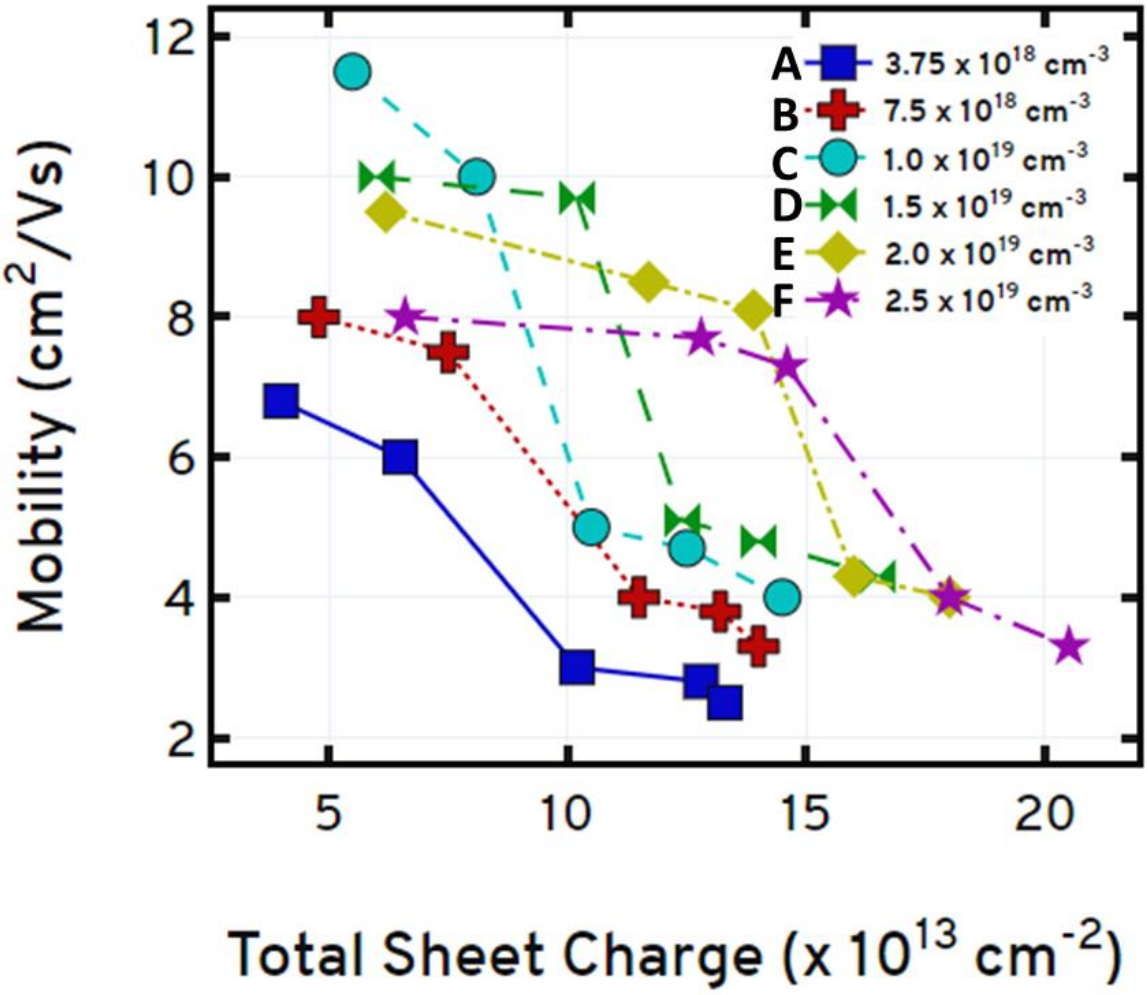

Figure 5.6 Room temperature Hall measurement results for samples reported in this study. The figure shows measured mobility as a function of measured total sheet charge concentration, for the various Mg dopings used. Series nomenclature A-F corresponds to the Table 5.1

For the samples in this study, as shown in Figure 5.4, the existence of the two-dimensional hole gas (2DHG) is at the AlN/GaN interface (for AlGaN/AlN/GaN SL) or an AlGaN/GaN interface, if no AlN is present (AlN interlayer (IL) thickness = 0 nm in Table

5.1). Table 5.1 indicates the samples presented in this work that have acceptor traps at the PPI ionizing, along with the interface where the traps ionized (PPI-1 or PPI-2).

Firstly, it was observed that for each of the AlN thickness series (with different Mg doping levels) the mobility values (μ_p) decreased in samples where the acceptor-like traps ionized. Within those set of samples, it was further observed that μ_p decreased drastically (>40% decrease) in those samples where AlN band-bending was $\geq$ 0.8eV – independent of the GaN band-bending level in the same sample. This could be explained by the fact that the 2DHG is closer to the AlGaN/AlN PPI which is referred to as PPI-1 (0 to 1.6nm) compared to the GaN/AlGaN PPI, referred to as PPI-2 (10nm). Hence, the more dominant source of scattering (and therefore the cause of the drastic decrease in μ_p) are the ionized acceptor-like traps which exist at the AlGaN/AlN PPI, the interface which closer to the 2DHG. The acceptor-like traps ionizing traps at GaN/AlGaN PPI (PPI-2) also cause scattering, but their effect is not as pronounced because they are further away from the 2DHG. This explains the observed higher mobilities in samples where only the GaN band-bending was $\geq$ 0.8eV, and the AlN band-bending was < 0.8eV leading to the ionization of traps at only the PPI-2.

This work presents 6 different series from our measurements labeled A – F based on the p-type Mg doping in the sample. Within each of those series there are 5 samples with different AlN interlayer thickness from 0 to 1.6nm. Analyzing each series of samples at a time, the main takeaway is that – traps at PPI1 (and hence AlN Band-bending) determines if the ionization of the acceptor-like trap drastically reduces the hole mobility – due to its proximity to the 2DHG (<1.6nm away) compared to PPI2 (10nm away). Figure 5.6 and Table 5.1 will be used in tandem to describe the trends in mobility reported in the study and thereby substantiate the hypothesis and analysis.

Table 5.1 Samples presented in the work labelled A-1 through F-5 with the letter referring to the Mg doping series, and the number referring to the AlN thickness series for each doping series. This table also indicates if the acceptor traps ionization is at interface PPI-1 (AlGaN/AlN interface) or interface PPI-2 (GaN/AlGaN interface), or both interfaces. The table also mentions if there is an effect on the measured mobility ($\Delta > 2.0$ cm^2/Vs) by the ionization of these traps. When traps at both interfaces are unionized, then '-' is mentioned to indicate that the acceptor-like traps are unionized and therefore have no effect on the mobility (In that case mobility may be affected slightly by the increase in charge as indicated in Figure 5.6).

S. No	Doping ($\times 10^{18}$ cm^{-3})	AlN layer thickness (nm)	Traps at PPI-1 [defined in figure 5.4]	Traps at PPI-2 [defined in figure 5.4]	μ_p affected by traps?
A-1	3.75	0	Un-ionized	Ionized	NO
A-2	3.75	0.7	Un-ionized	Ionized	NO
A-3	3.75	1.0	Ionized	Ionized	YES
A-4	3.75	1.4	Ionized	Ionized	YES
A-5	3.75	1.6	Ionized	Ionized	YES
B-1	7.5	0	Un-ionized	Un-ionized	-
B-2	7.5	0.7	Un-ionized	Ionized	NO
B-3	7.5	1.0	Ionized	Ionized	YES
B-4	7.5	1.4	Ionized	Ionized	YES
B-5	7.5	1.6	Ionized	Ionized	YES
C-1	10	0	Un-ionized	Un-ionized	-
C-2	10	0.7	Un-ionized	Un-ionized	-
C-3	10	1.0	Ionized	Ionized	YES
C-4	10	1.4	Ionized	Ionized	YES
C-5	10	1.6	Ionized	Ionized	YES

S. No	Doping ($\times 10^{18}$ cm^{-3})	AlN layer thickness (nm)	Traps at PPI-1 [defined in figure 5.4]	Traps at PPI-2 [defined in figure 5.4]	μ_p affected by traps?
D-1	**15**	**0**	**Un-ionized**	**Un-ionized**	**-**
D-2	**15**	**0.7**	**Un-ionized**	**Un-ionized**	**-**
D-3	**15**	**1.0**	**Ionized**	**Un-ionized**	**YES**
D-4	**15**	**1.4**	**Ionized**	**Ionized**	**YES**
D-5	**15**	**1.6**	**Ionized**	**Ionized**	**YES**
E-1	**20**	**0**	**Un-ionized**	**Un-ionized**	**-**
E-2	**20**	**0.7**	**Un-ionized**	**Un-ionized**	**-**
E-3	**20**	**1.0**	**Un-ionized**	**Un-ionized**	**-**
E-4	**20**	**1.4**	**Ionized**	**Un-ionized**	**YES**
E-5	**20**	**1.6**	**Ionized**	**Ionized**	**YES**
F-1	**25**	**0**	**Un-ionized**	**Un-ionized**	**-**
F-2	**25**	**0.7**	**Un-ionized**	**Un-ionized**	**-**
F-3	**25**	**1.0**	**Un-ionized**	**Un-ionized**	**-**
F-4	**25**	**1.4**	**Ionized**	**Un-ionized**	**YES**
F-5	**25**	**1.6**	**Ionized**	**Un-ionized**	**YES**

For **series-A**, by design, all the epitaxially grown samples have the traps ionizing. In A-1 and A-2 only traps at PPI2 are ionized, so the reduction in mobility is extremely negligible (Δ~1 cm^2/Vs), caused due to increase in charge. Traps at both PPI1 and PPI2 are active in samples A-3, A-4 and A-5 and therefore the drastic mobility reduction can be seen going from A-1, A-2 to A-3, A-4, and A-5.

In **series-B**, sample B-1 does not have any traps ionized, but B-2 has only traps at PPI2 ionized resulting in an exceedingly small reduction in mobility (Δ~1 cm^2/Vs), with the

increase in hole charge causing it. B-3 through B-5 have traps at both PPI1 and PPI2 ionized, and thus we can see a drastic reduction in mobility going from B-1, B-2 to B-3, B-4, and B-5.

In **series-C**, C-1 and C-2 do not have traps at any interface ionizing and we do not observe much reduction in mobility due to traps, although there is a slight decrease in mobility from C-1 to C-2 caused due to the addition of the AlN IL and the increased polarization charge. C-3 through C-5 have traps at both PPI1 and PPI2 ionized, and thus we can see a huge reduction in mobility going from C-1, C-2 to C-3, C-4, and C-5, much like what happens with series B.

In **series-D**, D-1 and D-2 do not have traps at any interface ionizing and we do not observe reduction in hole mobility due to traps. D-3 only has traps at PPI1 ionized, but not at PPI2, and we see a huge reduction in mobility, which confirms our preliminary hypothesis. D-4 and D-5 have traps at both PPI1 and PPI2 ionizing, and there is a drastic reduction in mobility from D-1, D-2, but D-3, D-4 and D-5 have similar mobilities, which reiterates the dominant effect of traps at PPI1 interface.

This is further confirmed in **series-E**, E-1, E-2, and E-3 do not have any traps ionizing and we do not observe much reduction in mobility due to traps. E-4 has only traps at PPI1 ionized, but not PPI2, and we see a huge reduction in mobility, which again confirms our preliminary hypothesis. E-5 has traps at both PPI1 and PPI2 ionizing, and there is a drastic reduction in mobility from E-1, E-2, E-3, but E-4, E-5 have similar mobilities.

In **series-F**, F-1 to F-3 do not have any traps ionizing, but F4 and F5 have traps at PPI1 ionizing, which reduces its mobility. On analyzing the series, A – F, it can be inferred that the acceptor-like trap ionizing at the PPI closer to the 2DHG scatters the holes to a greater

extent, and hence has a major effect in reducing the μ_p. Note that these samples were all predictively designed such that the various interfaces were ionized per the hypothesis. The experimental data verifies this particularly important hypothesis.

D. Cases with acceptor traps explaining measured charge

In Chapters 4 and 5, we have shown the existence of acceptor-like traps in p-type III-nitride systems using Ga-polar, and N-polar, Modulation doped and Uniformly doped GaN/AlN/AlGaN, and GaN/AlGaN superlattices as demonstration and design platforms.

Using this developed methodology, we can explain the immensely important concept of charge balance is p-type III-nitride systems which have insufficient Mg-doping in them. This section presents three recently reported studies where the measured hole concentration was greater than the amount of p-type dopants in the samples (and even greater than the polarization charge), and we use the methodology developed in Chapters 4 and 5 to explain the measured hole mobility, and the discrepancy in the measured total charge of holes, in these samples.

(i) The source of charge balance for holes in systems with no Mg doping:

Recently reported studies by R. Chaudhuri, et. al. from Cornell University [96], use undoped AlN/GaN structure and obtain a total hole sheet charge of $p_s=6\times10^{13}$ cm^{-2} with no Mg dopants. This work does not explain the source of these excess holes and does not provide charge balance.

Using the methodology presented in Chapters 4 & 5 of this dissertation, we first simulated the structure from Cornell researchers using our STR-FETIS model to obtain the expected total sheet charge of holes, if there were no acceptor traps present. The calculations provided $p_s = 2.67\times10^{13}$ cm^{-2}. Then band-diagrams are calculated for the structure (without

taking acceptor-traps into consideration) as shown in Figure 5.7. We can see that the band-bendings are greater than 0.8eV at the net positive polarization AlN/GaN interface (PPI from Figure 5.7). We therefore attribute the source of these excess charges to the ionization of acceptor traps at that PPI.

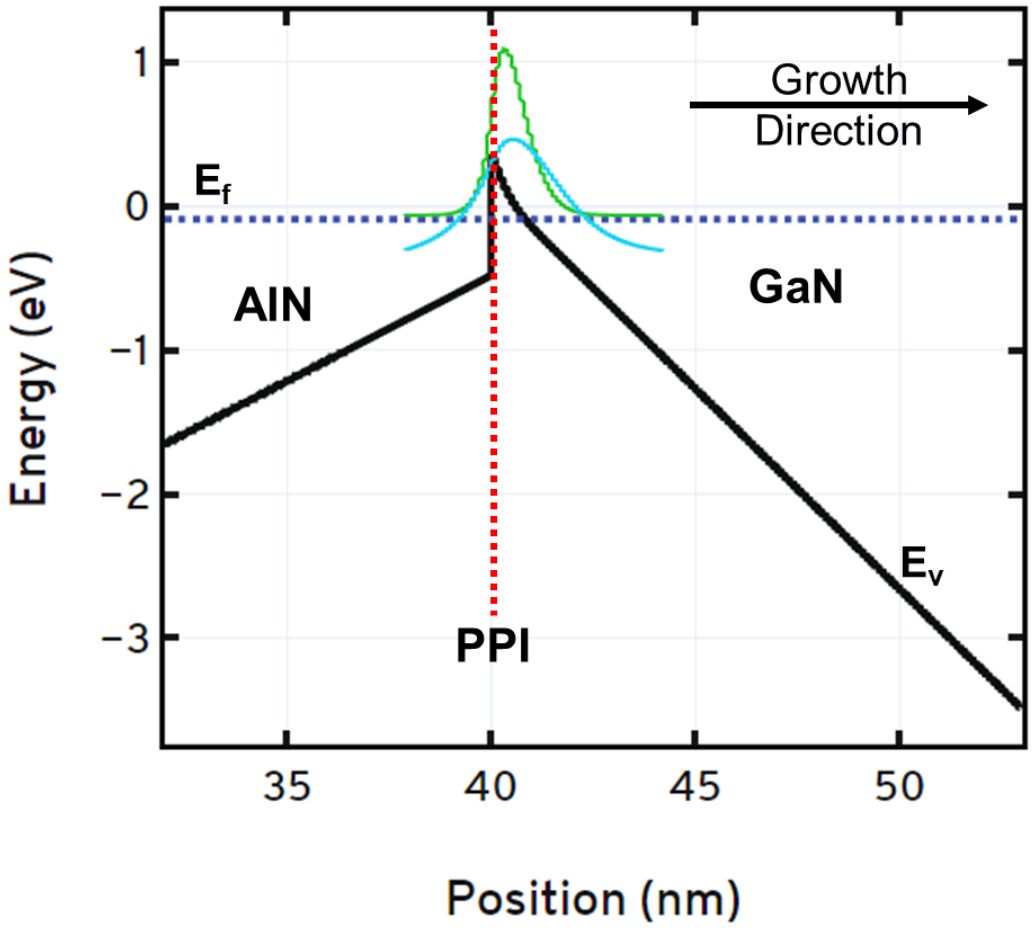

Figure 5.7 Calculated Valence Band-diagram for the AlN/GaN structure reported by R. Chaudhuri et.al., using STR-FETIS – without accounting for the acceptor traps at PPI (indicated)

In that reported work using GaN/AlN structure grown using MBE growth technique, (a) there was no alloy scattering (as the 2DHG forms at the AlN/GaN interface), (b) there was no impurity scattering (as there were no Mg doping in the structure), and (c) MBE grown p-

type III-nitrides are not passivated by hydrogen. Yet, the measured hole mobility was very low (10 – 20 cm^2/Vs) for the various reported samples. Using the methodology developed in this dissertation, one can see in Figure 5.7, that the 2DHG forms at the PPI. So, when the acceptor traps at this interface are ionized (as is the case here), these traps cause scattering due to which the hole mobility decreases.

(ii) Explaining the high p_s in recently reported E-Mode p-channel GaN FinFET:

Recently H. Du, et. al., from Xidian University, China (2022), reported a normally-off p-channel GaN FinFET grown on GaN-on-Si [97]. Figure 5.8 shows the structure of the device along with the images from the original work [© 2022 IEEE].

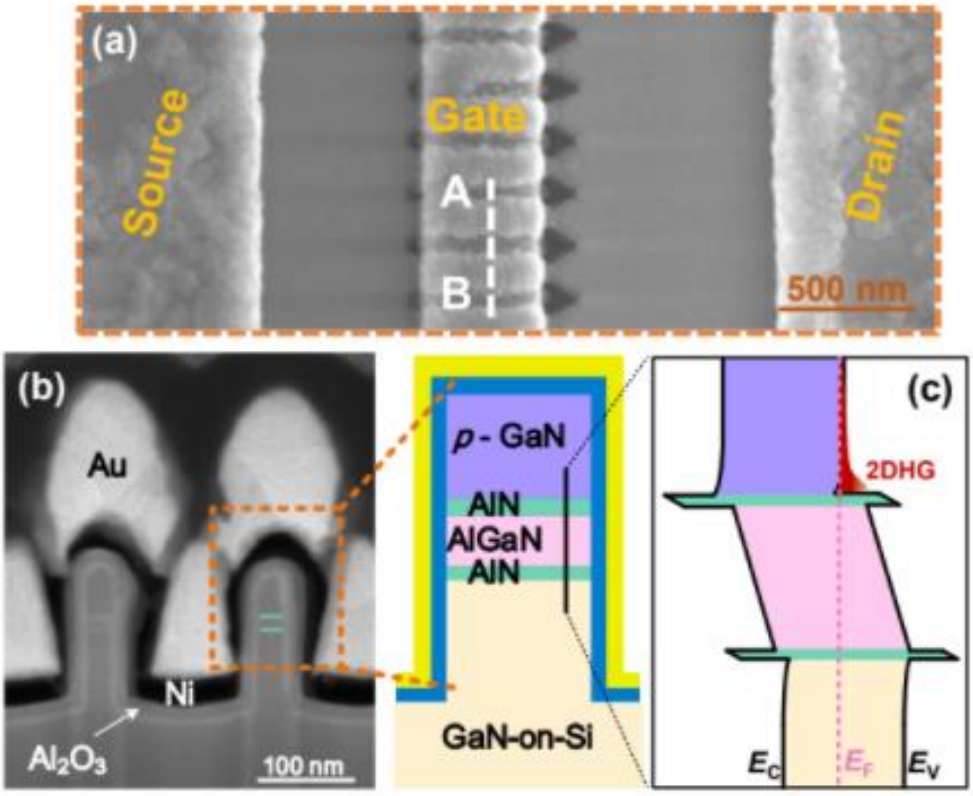

Figure 5.8 Reported p-channel FinFET from H. Du, et. al. [© 2022 IEEE] (a) Top-view SEM image of the fabricated p -channel GaN FinFET with 25-nm-wide nanowires. (b) Focused ion beam cross-section along the AB line in Fig. 5.8 (a) and diagram of the nanowires covered by the tri-gate architecture. (c) Corresponding energy-band diagram. [97]

This work claims that the measured total sheet charge of holes is $p_s = 2\times10^{14}$ cm^{-2} with the hole mobility equal to $\mu_p \sim 2$ cm^2/Vs. This charge is extremely high compared to the dopants in the sample, so the obvious question to be answered is regarding the source of holes and charge balance in this structure. Revisiting the developed methodology of acceptor traps, we first calculated the expected sheet charge density in the structure using STR-FETIS and obtained that to be $p_s = 9\times10^{12}$ cm^{-2}. We next calculated the valence band diagram for the structure (without accounting for acceptor-traps) and observed that the band-bending at both net positive polarization interfaces (PPI) was greater than 0.8eV. Figure 5.9 shows the calculated valence band diagram along with the PPI indicated, and the location of the 2DHG.

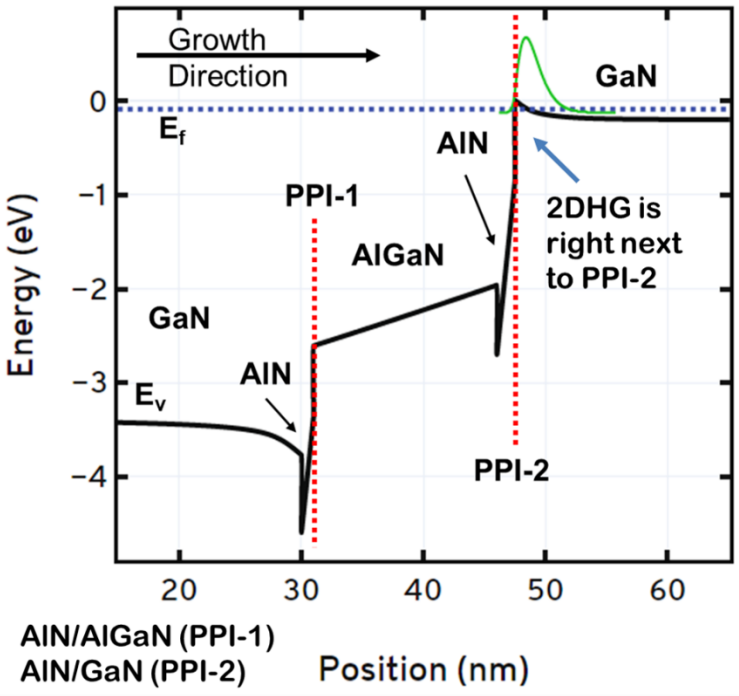

Figure 5.9 Calculated valence band diagram for the structure presented in [97]. The net positive polarization interfaces (PPI-1 and PPI-2) are indicated, along with the location of the 2DHG.

The two net positive polarization interfaces are : AlN/AlGaN (PPI-1) and AlN/GaN (PPI-2) interfaces. The 2DHG forms right at the PPI-2 interface. Now, since the AlN band bending is >0.8eV (without invoking traps), we know that the acceptor traps are ionizing at this interface, and hence lead to the scattering of holes in the 2DHG, thereby reducing the hole mobility drastically.

Going one step further, we are able to predict that if traps ionized only at PPI-1 and not at PPI-2, then we would see extremely high measured charge, along with a reasonably high hole mobility.

(iii) Holes > polarization in InGaN/AlN on AlN substrates

A recent work by R. Chaudhuri, et. al., (2022), reported a measured total sheet charge of holes, p_s = 1 to 5 $\times 10^{14}$ cm^{-2} [98]. This structure did not have any dopants, and the maximum polarization charge possible was = 1×10^{13} cm^{-2} in these InAlN/AlN undoped structures grown on AlN substrates using MBE. While our methodology in this dissertation was developed using Al(Ga)N/GaN systems, it can further extend to include all III-nitride heterostructures.

Figure 5.10 formalizes the methodology developed in Chapters 4 and 5 of this work to predict the ionization of the 0.8eV acceptor-like trap at positive polarization interfaces in dopant deficient p-type III-nitride systems.

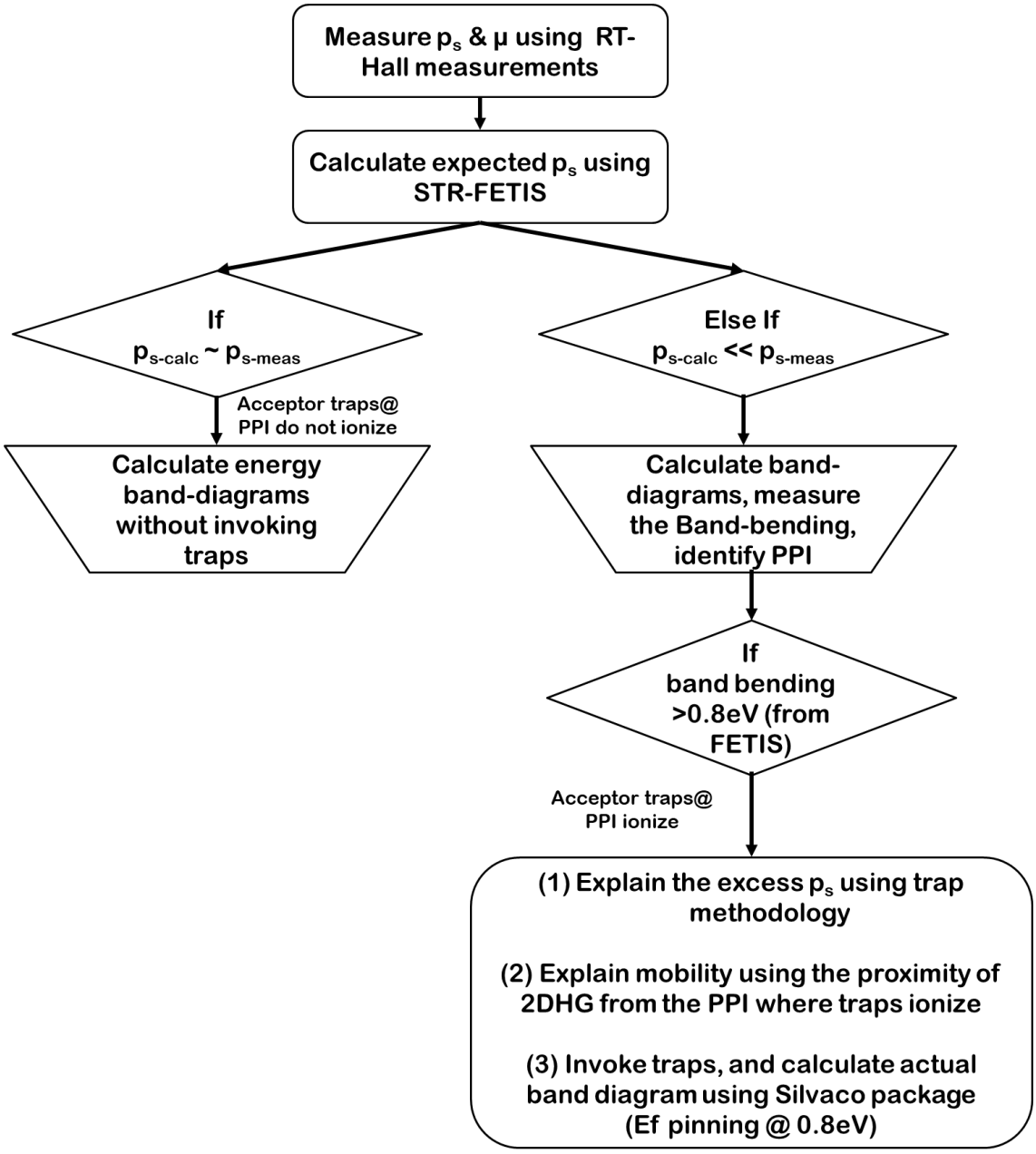

Figure 5.10 Formalized flowchart of the methodology developed in chapters 4 and 5 of this dissertation to explain the excess charge and mobility in dopant deficient p-type III-nitride systems using ionization of acceptor-like traps at Positive polarization interfaces

E. Benchmarking Rsh in p-type III-nitrides

Figure 5.11 benchmarks the Rsh in various reported p-channel systems from literature. Work from Chapters 4 & 5 present the lowest Rsh amongst III-nitrides (Rsh ~1.5kΩ/sq).

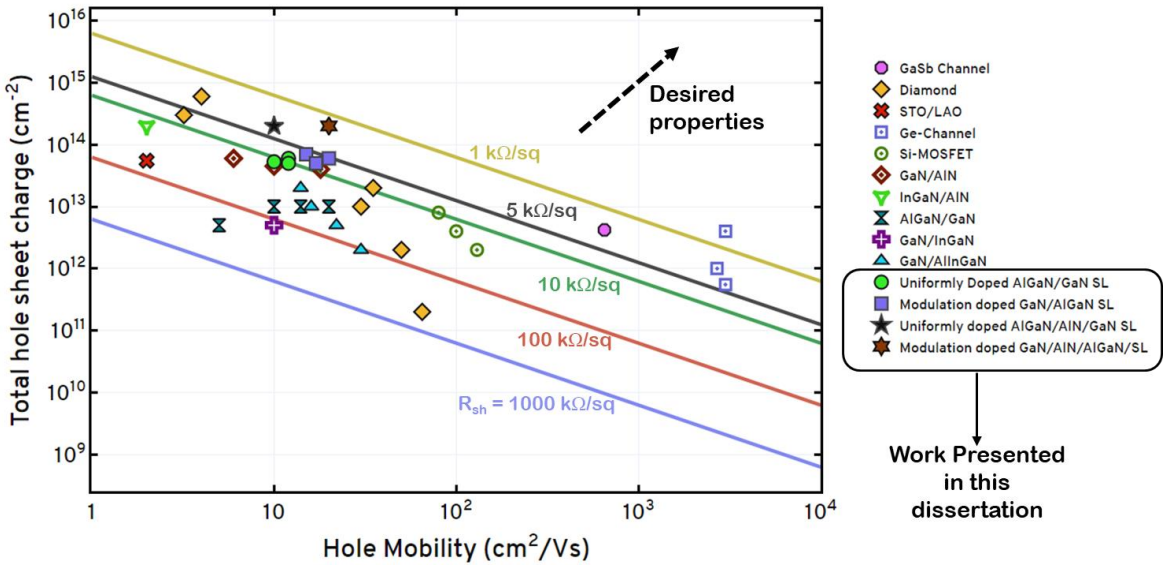

Figure 5.11 Benchmarking the Rsh in the p-type channels of various materials system reported in literature. The solid lines indicate the Rsh level (calculated using Eq. (2)), and the legend indicates the materials system. Lower the sheet resistance, better for application in p-type FETs. All the devices presented in this dissertation are indicated with a box in the plot legend.

Chapter 6

MOCVD development of p++ GaN regrowth for contact regions in pFinFETs

In Chapter 1 of this dissertation, we mentioned 4 main issues with holes in p-type III-nitrides. While we tackled and issues of low-hole mobility and deep acceptor dopants using (a) p-type AlGaN/GaN SL, (b) Modulation doping, and (c) utilizing the acceptor-like traps at PPI as the source of holes, we had not yet touched upon the issues with making good Ohmic contacts to p-GaN for fabricating pFETs. This chapter will only touch upon the development of the regrowth and its initial application in p-type FinFETs. Details of all the electronic devices (including the record-breaking ones), will be presented by Aditya Raj in their dissertation.

In previous works by A. Raj, et.al, we have achieved both normally-on and normally-off operation using GaN/AlGaN SL based FinFETs [55]. More recently, A. Raj, et. al, achieved highest reported I_{on} for normally-off GaN pFETs using MOCVD regrown p^+ contact layers around these SL fins [56]. To further scale the devices, selective area regrown contacts are

required. In this chapter, we use dry etched SiO_2 mask to selectively grow p^+ GaN contact layer around Mg-doped GaN/AlGaN SL fins. All the device processing mentioned in this chapter was carried out by A. Raj.

The Ga-polar epitaxial structure shown in Figure 6.1 was grown by MOCVD on sapphire substrate. The 7 period Mg-doped GaN/$Al_{0.2}Ga_{0.8}N$ SL provides the parallel 2DHG channels. The TLM test structure fabrication started with the activation of the epitaxial structures at 800°C in a N_2 environment for 5 min. Post activation, the fin structures were obtained by performing a low power (15W) BCl_3/Cl_2 etch using reactive ion etching (RIE) to obtain near vertical sidewalls with low damage. The fins were patterned along the m-plane to keep the structure compatible with TMAH etch step in the standard GaN/AlGaN SL FinFET process developed by A. Raj, et. al. [55]. Thereafter, SiO_2 mask was patterned for selective area regrowth.

Just before the samples were loaded into MOCVD chamber for p^+-GaN contact regrowth, it went through a 4 min HCl dip. Prior to the p^+-GaN regrowth, the sample was subjected to a 30min in-situ anneal at 900° C and a 70 sec Mg pre-flow step in the MOCVD reactor to ensure sufficient uptake of Mg in the subsequent regrown GaN layer. The targeted thickness and Mg doping in the regrown contact layer was 50 nm and 2 x 10^{20} cm^{-3}, both calibrated for c-plane.

After the contact regrowth, the SiO_2 mask was removed, and the sample again underwent the activation step described above. Post the activation step, the Transmission Line Method (TLM) test structures were isolated using the same low power RIE etch. Subsequently, ohmic contact metal (Pd/Au) was deposited using electron-beam evaporation

technique. Figure 6.2 shows the process flow described above, and Figure 6.3 shows the SEM images of the TLM structures at different steps along the fabrication flow.

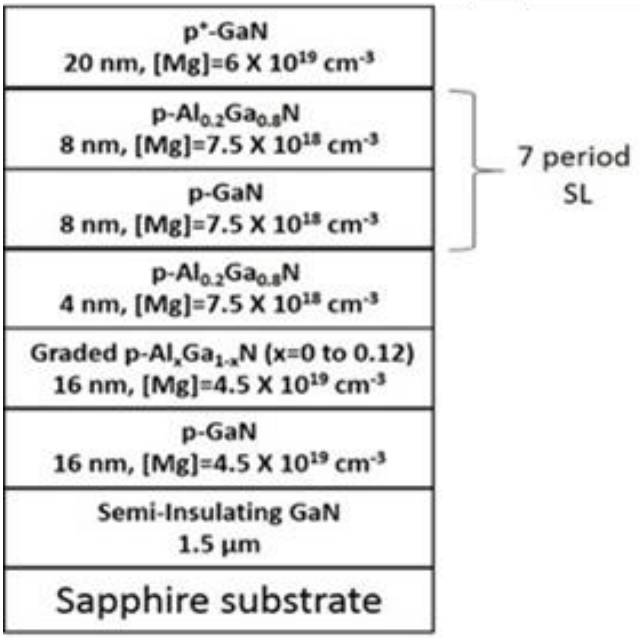

Figure 6.1 Epitaxial structure of the 7 period Ga-Polar uniformly doped GaN/AlGaN superlattice grown by MOCVD, used to fabricate the TLM structures presented in this chapter

TLM test structures with fin width varying from 400 nm to 550 nm were tested and analyzed. Each test structure had 20 fins each. Figure 6.4 (a) shows the TLM I-V characteristics of 400 nm wide fin structures for varying TLM spacing. The current has been normalized with fin width. The regrown p^+ contact layer provides electrical contacts to the hole channels in the SL fins through the sidewall without any turn-on voltage in I-V characteristics. Fig. 6.4 (b) shows I-V characteristics of the TLM structure with a spacing of 1.5µm for varying fin width.

Fig. 5(a) shows extracted R_{sh} and contact resistance (R_c) as a function of current for 500nm wide fins. R_c was normalized using 2×fin-height as current flows from metal contacts to SL channels primarily through the sidewall contacts. The R_c drops from around

30 Ω.mm at low currents to around 8 Ω.mm at current > 100 mA/mm. This decrease in R_c with increase in current is typical for p-GaN contacts. Fig. 5(b) shows the R_{sh} and R_c for different fin width devices at 100 mA/mm current.

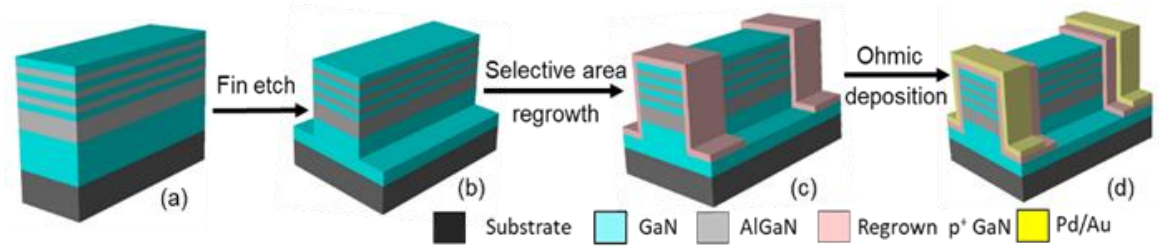

Figure 6.2 TLM structure fabrication process flow overview (a) MOCVD grown GaN/AlGaN SL epitaxial structure (from Fig 6.1); (b) dry etch patterned fin; (c) fin with selective area p^+ contact regrowth around fin; (d) Ohmic metal deposition around the regrown p^+-GaN layer.

Fig. 6 shows the effect of in-situ pre-regrowth MOCVD anneal. The sample processed without this anneal step shows significantly higher R_c at low currents. At higher currents, the difference in R_c reduces until they are equal at ~120 mA/mm current. In-situ pre-regrowth anneal has been shown to improve the electrical properties of etched sidewall regrowth interface [99].

This Chapter will only mention the TLM measurements post the MOCVD p+ selective area regrowth. All the p-FinFET device data will be presented in great detail by Aditya Raj in their dissertation.

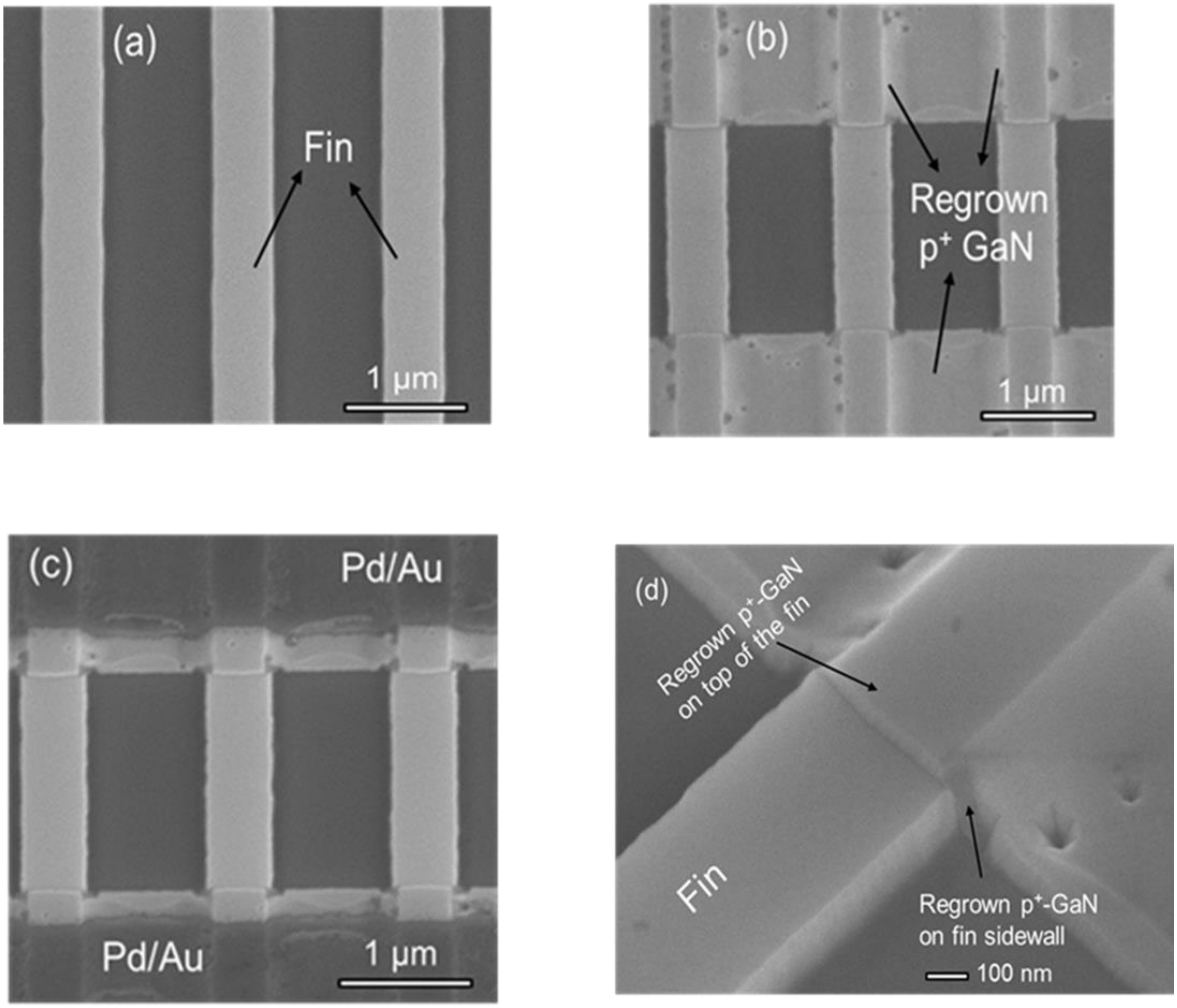

Figure 6.3 SEM images at different stages of fabrication process (as shown in Fig 6.2) (a) after fin etch; (b) after selective area regrowth; (c) after ohmic deposition. (d) angled view of the fin with regrown p^+ GaN layer around it.

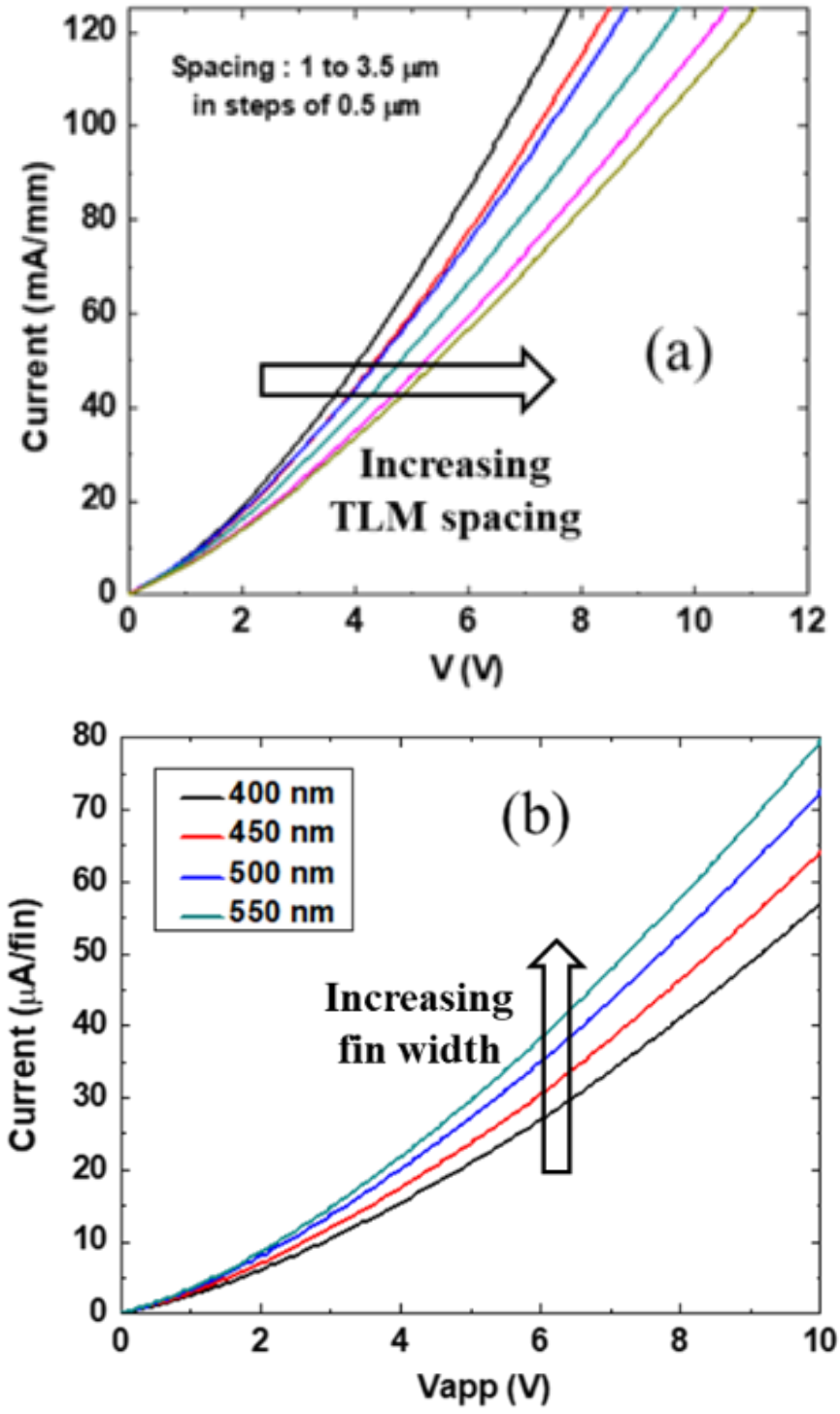

Figure 6.4 . (a) TLM I-V characteristics of 400 nm wide fin structures with varying TLM spacing. Current is normalized using fin width (b) TLM I-V characteristics of TLM spacing=1.5 μm for varying fin width.

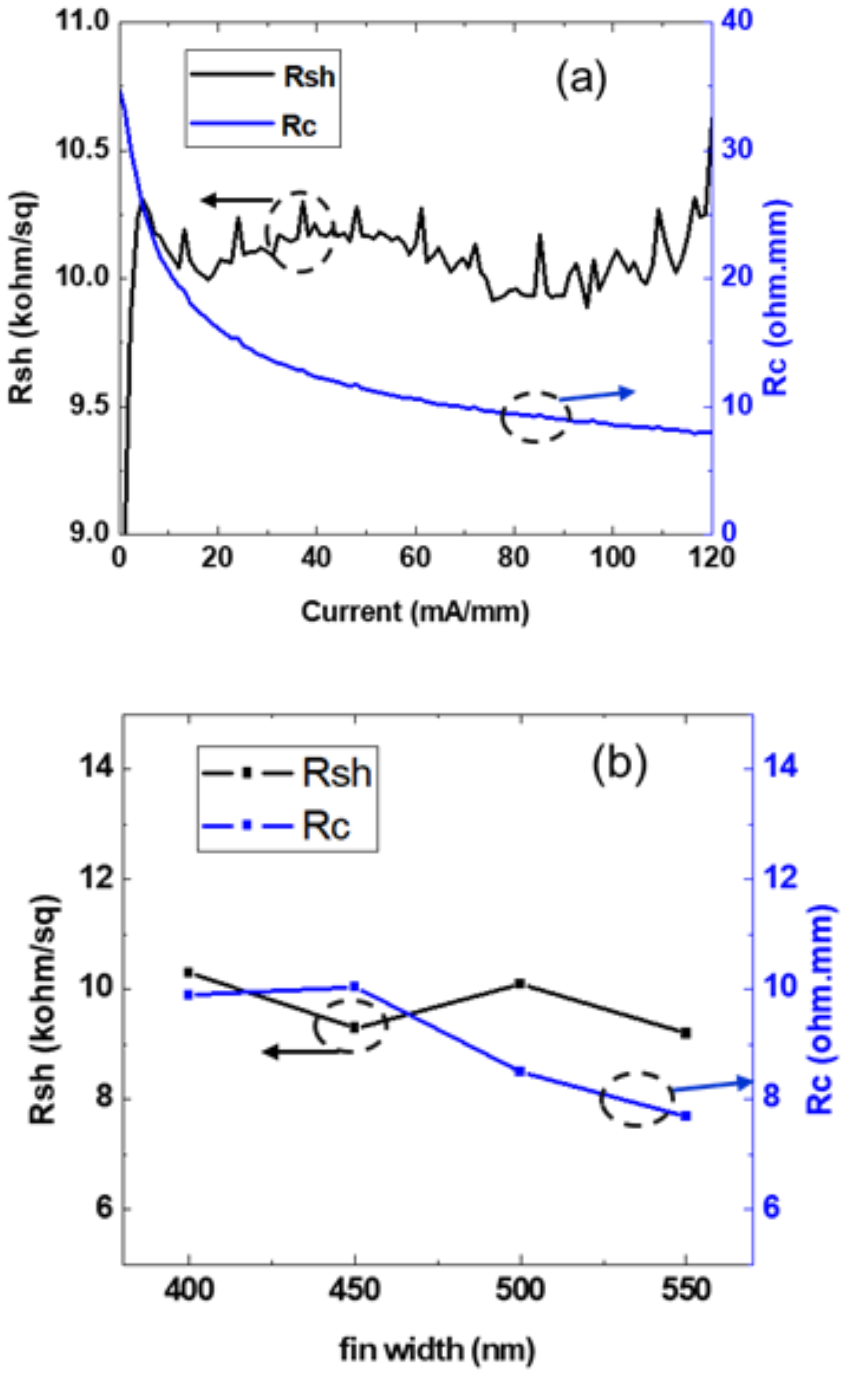

Figure 6.5 . (a) Extracted Rsh and Rc for 500 nm wide fin TLMs as a function of current. Rsh is normalized using fin width and Rc is normalized using 2×fin height. Rc decreases from ~30 ohm.mm at low current density to ~8 ohm.mm current > 100 mA/mm; (b) Extracted Rsh and Rc at current density of 100 mA/mm for varying fin width.

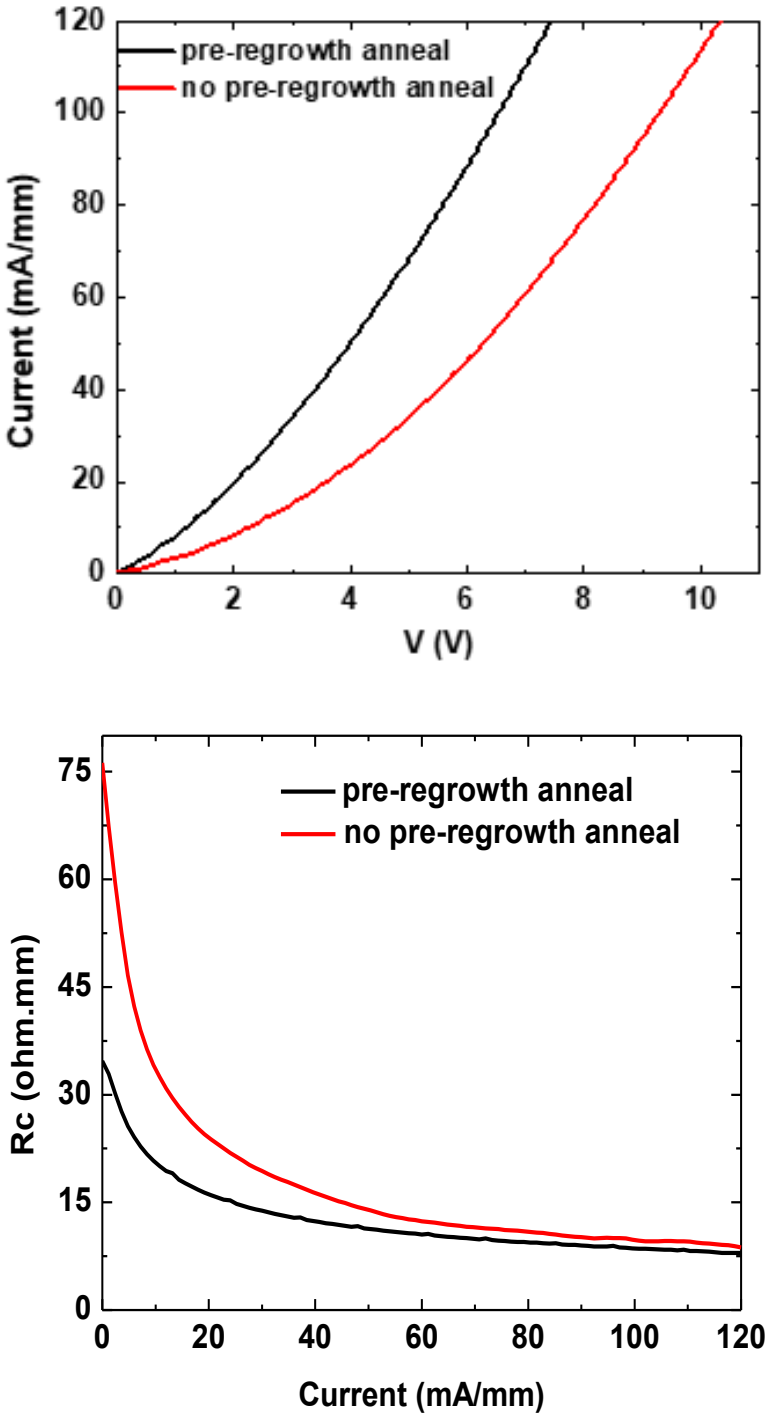

Figure 6.6. (above) Comparison of measured current shows significant improvement in current for sample which underwent in-situ pre-regrowth anneal; (below) Comparison of Rc shows significant improvement in Rc at low currents for sample which underwent in-situ pre-regrowth anneal.

Chapter 7

Future Work and Conclusion

The answer to how to get more holes in an epitaxially grown structure in p-type III-nitrides is interesting for its uses in both optoelectronics (for contact layers), and next generation electronics (for GaN-based CMOS) . The presence and subsequent experimental validity of these acceptor-like traps opens up a novel method to engineer around III-nitride structures to achieve the desired total hole concentrations. The component of this present study on traps at which PPI have a major effect on the hole mobility, provides an indication to design new LED and FET structures which can overcome the inherent challenges with holes in III-nitrides.

Looking ahead, some of the potential future experiments include:

(i) Desirable p-FinFET design

Based on the work presented in this dissertation and the device processing of SL based p-FinFETs, the ideal p-FinFET design is as follows:

- Ga-Polar epitaxial structure : Due to the ease of processing. Ga-polar structures can exploit the TMAH treatment (mentioned in Chapter 2 of this work) to remove the etch damage, scale the devices, and ultimate turn the device off.

- High-sheet charge of holes : Using the acceptor trap methodology developed in this dissertation, epitaxial structure could be design to ionize the acceptor traps at only one positive polarization interface – which is away from the interface where the 2DHG is formed (thus leaving the mobility unaffected).
- High hole mobility: Using MOCVD, we are limited to only uniform doping of Ga-Polar material (leading to a mobility of ~10cm^2/Vs). But, if MBE growth technique is used, Ga-Polar modulation doping can be realized – leading to a high hole mobility ~20 cm^2/Vs.
- High quality, highly p+ doped selective area regrowth – as described in Chapter 6 of this work.

(ii) Short-period SL for Deep-UV LED contact layers:

High performance Deep-UV LEDs desire high hole concentrations without much Mg doping. This is one possible application of the acceptor-trap hypothesis developed in this work. Initial work was carried out to inspect the validity of the ionization of acceptor traps in thin GaN/AlN SL. (Note: we used N-polar epitaxial layers since we desired modulation doping using MOCVD technique).

Figure 7.1 shows the epitaxial structure of the samples grown for this study. A superlattice period series of 4, 7 and 10 SLs were grown with each SL period consisting of : 2nm p-GaN (Mg:3.75×10^{18} cm^{-3}) / 2nm UID GaN/ 0.7nm UID AlN/ 0.7nm p-AlN (Mg:3.75×10^{18} cm^{-3}). Thin SLs were grown since we are interested in vertical transport of the LED contact layers.

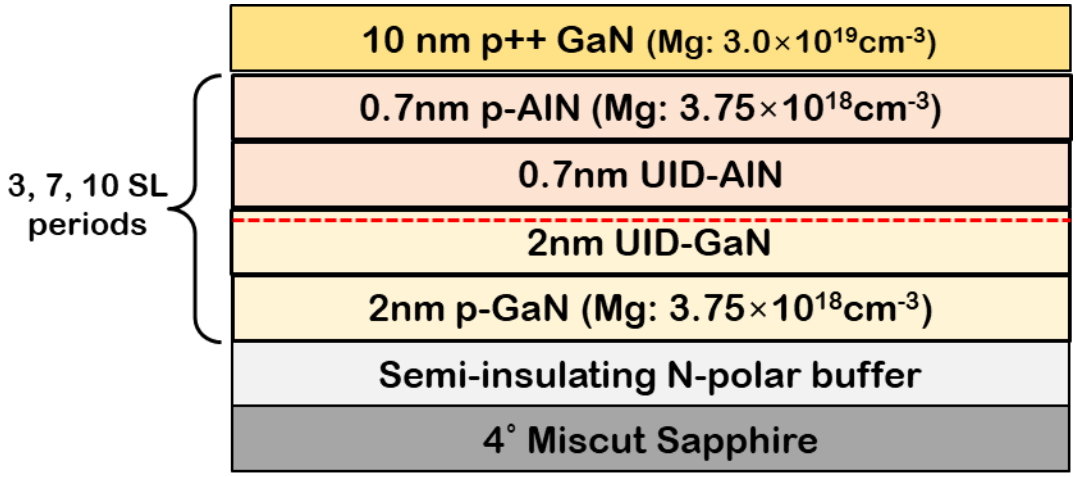

Figure 7.1 Epitaxial structure of N-Polar modulation doped short-period SL series (4, 7, and 10 SL periods) grown using MOCVD. The red dotted line indicates the formation of the 2DHG.

Figure 7.2 shows the Total sheet charge concentration of holes and the hole mobility measured using RT-Hall effect measurements for the SL period series grown for this study.

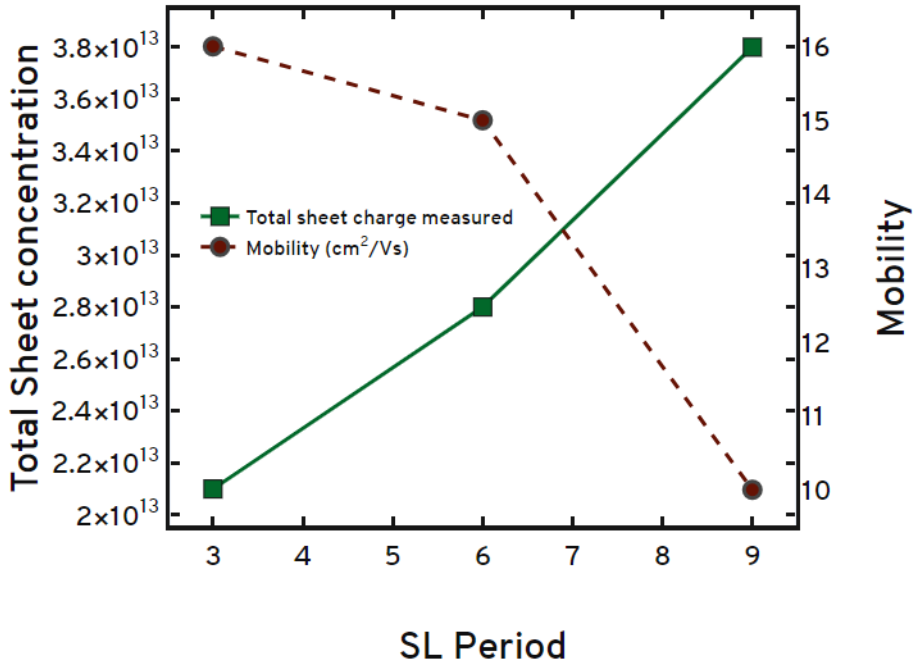

Figure 7.2 Total sheet charge concentration and mobility as a function of the SL period. Since these are very thin SLs, we are able to contact all the 10 SL layers from the top (in contrast to the contacting issues mentioned in Chapters 2-6 leading to growth of 7 period SL).

STR-FETIS simulations were then carried out to compare the measured and the calculated total sheet charge concentration of holes. Figure 7.3 shows this comparison, and since we also have a thick bulk p-type layer of 10nm on top for the purpose of making good Ohmic contacts, we decouple the effects of this layer, and account for it separately in the same figure. From the figure we can see that the acceptor traps are indeed ionizing and leading to the excess holes measured in the samples.

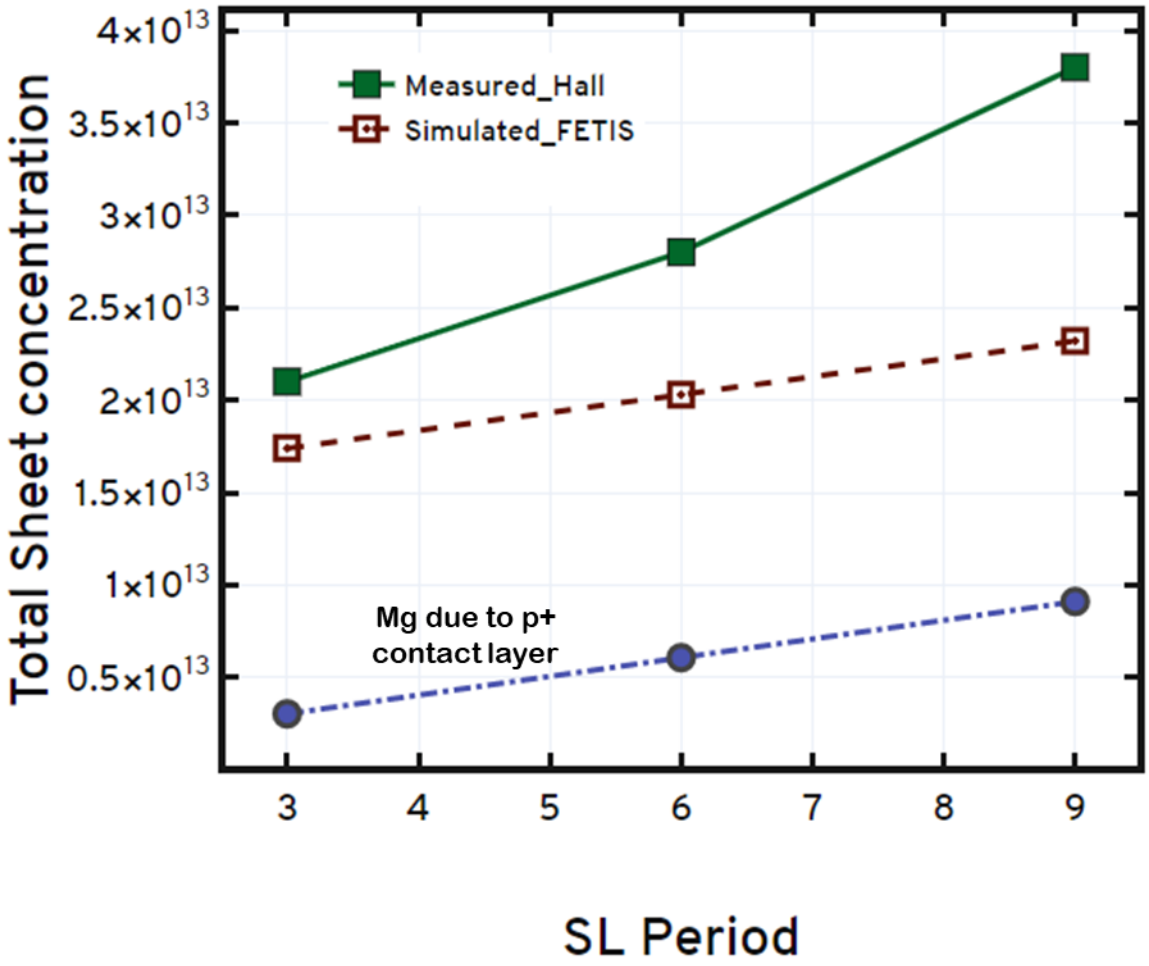

Figure 7.3 Comparison of the measured and the calculated total sheet charge concentration of holes. The measured holes from the top bulk p+ contact layer is decoupled in this figure and shown separately in the figure.

This simple study proved the ionization of acceptor traps even in short-period SL stacks, as long as the band-bending hits the 0.8eV trap level. But, this will need a few modifications

before its application in contact layer for Deep-UV LEDs. Some of the proposed design changes and modifications include:

- Ga-Polar epitaxial structure instead of the N-polar structure since Ga-Polar orientation is preferred for high-performance optoelectronic devices.
- Design of a high Al % AlGaN/AlN short-period SL stack instead of a GaN/AlN stack. Presence of GaN in a Deep-UV LED is detrimental to the performance of the device as it absorbs the emitted light.

(iii) Determining the true nature of the acceptor-like trap:

While the results in this Dissertation use simulation and experimentation to highlight the effect of these acceptor-like traps on the charge and mobility of holes in p-type nitrides, one method to determine the true nature of these traps is positron annihilation spectroscopy (PAS), which has been carried out for corresponding n-type III-nitrides. A detailed PAS study of the p-type SLs discussed in this study is under way in collaboration with Prof. Filip Tuomisto's research group at University of Helsinki, and the results will be presented in a later publication.

Summarizing the presented work, we systematically tackled the issues with holes in III-nitride materials system. First the issues with Deep acceptor dopants were tackled with the use of p-type AlGaN/GaN SL presented in Chapter 2. The polarization effects in III-nitride superlattices (SL) lead to the periodic oscillation of the energy bands, exhibiting enhanced ionization of the deep acceptors (Mg, in this study), and hence their utilization in III-nitride semiconductor-based light emitting diodes (LEDs) and p-channel FETs, is beneficial. Rsh as low as 10kΩ/sq (μ_p=10cm^2/Vs; p_s=6×10^{13} cm^{-2}) was presented.

To improve the mobility further, modulation doping scheme was used in N-polar GaN/AlGaN SL presented in Chapter 3. Rsh as low as =5kΩ/sq (μ_p=20cm^2/Vs; p_s=6×10^{13} cm^{-2}) was shown.

In an effort to improve the mobility further, GaN/AlN/AlGaN SL were grown, and their electrical characterizations led to the discovery of a novel acceptor-like trap at positive polarization interfaces, referenced 0.8eV above the valence band of GaN, in p-type III-nitrides. Chapter 4 provides the methodology to analyze the effects of this acceptor trap on the hole mobility, and the source of excess holes in dopant deficient p-type systems. In the process, p-type material with Rsh as low as =1.5 kΩ/sq (μ_p=20cm^2/Vs; p_s=2×10^{14} cm^{-2}) was demonstrated, and this is the lowest reported sheet resistance amongst all p-channel III-nitride systems reported in literature, yet.

Chapter 5 helped confirm this acceptor trap hypothesis, and this was demonstrated by designing the experiments around Ga-Polar uniformly doped AlGaN/AlN/GaN SL. Chapters 4 and 5 helped explain the source of holes and provided charge balance in Mg deficient systems and provided a method to get more holes than the Mg dopants in p-type III-nitrides – a very important application for p-type electronic and optoelectronic devices.

Chapter 6 tackled the issues with making good ohmic contacts to p-GaN – by the development of an MOCVD selective area regrowth, for application in p-channel SL FinFET.

Appendix A details the STR-FETIS model used to develop the acceptor-trap hypothesis, and mentions how the Mg dopants in the systems were counted.

References

1. Nakamura, S.; Fasol, G. *The Blue Laser Diode: GaN Based Light Emitters and Lasers*; Springer: Berlin; New York, 1997; ISBN 978-3-662-03462-0.

2. Nakamura, S.; Mukai, T.; Senoh, M. High-brightness InGaN/AlGaN Double-heterostructure Blue-green-light-emitting Diodes. *Journal of Applied Physics* **1994**, *76*, 8189–8191, doi:10.1063/1.357872.

3. Zhao, S.; Mi, Z. Recent Advances on P-Type III-Nitride Nanowires by Molecular Beam Epitaxy. *Crystals* **2017**, *7*, 268, doi:10.3390/cryst7090268.

4. Asif Khan, M.; Shatalov, M.; Maruska, H.P.; Wang, H.M.; Kuokstis, E. III–Nitride UV Devices. *Jpn. J. Appl. Phys.* **2005**, *44*, 7191–7206, doi:10.1143/JJAP.44.7191.

5. Hoo Teo, K.; Zhang, Y.; Chowdhury, N.; Rakheja, S.; Ma, R.; Xie, Q.; Yagyu, E.; Yamanaka, K.; Li, K.; Palacios, T. Emerging GaN Technologies for Power, RF, Digital, and Quantum Computing Applications: Recent Advances and Prospects. *Journal of Applied Physics* **2021**, *130*, 160902, doi:10.1063/5.0061555.

6. Meneghini, M.; De Santi, C.; Abid, I.; Buffolo, M.; Cioni, M.; Khadar, R.A.; Nela, L.; Zagni, N.; Chini, A.; Medjdoub, F.; et al. GaN-Based Power Devices: Physics, Reliability, and Perspectives. *Journal of Applied Physics* **2021**, *130*, 181101, doi:10.1063/5.0061354.

7. Romanczyk, B.; Li, W.; Guidry, M.; Hatui, N.; Krishna, A.; Wurm, C.; Keller, S.; Mishra, U.K. N-Polar GaN-on-Sapphire Deep Recess HEMTs With High W-Band Power Density. *IEEE Electron Device Letters* **2020**, *41*, 1633–1636, doi:10.1109/LED.2020.3022401.

8. Wienecke, S.; Romanczyk, B.; Guidry, M.; Li, H.; Ahmadi, E.; Hestroffer, K.; Zheng, X.; Keller, S.; Mishra, U.K. N-Polar GaN Cap MISHEMT With Record Power Density Exceeding 6.5 W/Mm at 94 GHz. *IEEE Electron Device Letters* **2017**, *38*, 359–362, doi:10.1109/LED.2017.2653192.

9. Mishra, U.K.; Shen, L.; Kazior, T.E.; Wu, Y.-F. GaN-Based RF Power Devices and Amplifiers. *Proceedings of the IEEE* **2008**, *96*, 287–305, doi:10.1109/JPROC.2007.911060.

10. Runton, D.W.; Trabert, B.; Shealy, J.B.; Vetury, R. History of GaN: High-Power RF Gallium Nitride (GaN) from Infancy to Manufacturable Process and Beyond. *IEEE Microwave Magazine* **2013**, *14*, 82–93, doi:10.1109/MMM.2013.2240853.

11. Zhang, Y.; Zubair, A.; Liu, Z.; Xiao, M.; Perozek, J.; Ma, Y.; Palacios, T. GaN FinFETs and Trigate Devices for Power and RF Applications: Review and

Perspective. *Semicond. Sci. Technol.* **2021**, *36*, 054001, doi:10.1088/1361-6641/abde17.

12. McCarthy, L.S.; Smorchkova, I.P.; Xing, H.; Kozodoy, P.; Fini, P.; Limb, J.; Pulfrey, D.L.; Speck, J.S.; Rodwell, M.J.W.; DenBaars, S.P.; et al. GaN HBT: Toward an RF Device. *IEEE Transactions on Electron Devices* **2001**, *48*, 543–551, doi:10.1109/16.906449.

13. Dahal, R.; Pantha, B.; Li, J.; Lin, J.Y.; Jiang, H.X. InGaN/GaN Multiple Quantum Well Solar Cells with Long Operating Wavelengths. *Appl. Phys. Lett.* **2009**, *94*, 063505, doi:10.1063/1.3081123.

14. Hurwitz, E.N.; Asghar, M.; Melton, A.; Kucukgok, B.; Su, L.; Orocz, M.; Jamil, M.; Lu, N.; Ferguson, I.T. Thermopower Study of GaN-Based Materials for Next-Generation Thermoelectric Devices and Applications. *Journal of Elec Materi* **2011**, *40*, 513–517, doi:10.1007/s11664-010-1416-9.

15. Huang, Y.; Melton, A.; Jampana, B.; Jamil, M.; Ryou, J.-H.; Dupuis, R.D.; Ferguson, I.T. Compositional Instability in Strained InGaN Epitaxial Layers Induced by Kinetic Effects. *Journal of Applied Physics* **2011**, *110*, 064908, doi:10.1063/1.3626434.

16. Chatzakis, I.; Krishna, A.; Culbertson, J.; Sharac, N.; Giles, A.J.; Spencer, M.G.; Caldwell, J.D. Strong Confinement of Optical Fields Using Localized Surface Phonon Polaritons in Cubic Boron Nitride. *Opt. Lett.* **2018**, *43*, 2177, doi:10.1364/OL.43.002177.

17. Fragkos, I.E.; Tansu, N. Surface Plasmon Coupling in GaN:Eu Light Emitters with Metal-Nitrides. *Sci Rep* **2018**, *8*, 13365, doi:10.1038/s41598-018-31821-8.

18. Zhou, C.; Ghods, A.; Saravade, V.G.; Patel, P.V.; Yunghans, K.L.; Ferguson, C.; Feng, Y.; Kucukgok, B.; Lu, N.; Ferguson, I.T. Review—The Current and Emerging Applications of the III-Nitrides. *ECS J. Solid State Sci. Technol.* **2017**, *6*, Q149–Q156, doi:10.1149/2.0101712jss.

19. Kako, S.; Santori, C.; Hoshino, K.; Götzinger, S.; Yamamoto, Y.; Arakawa, Y. A Gallium Nitride Single-Photon Source Operating at 200 K. *Nature Mater* **2006**, *5*, 887–892, doi:10.1038/nmat1763.

20. Bernardini, F.; Fiorentini, V.; Vanderbilt, D. Spontaneous Polarization and Piezoelectric Constants of III-V Nitrides. *Phys. Rev. B* **1997**, *56*, R10024–R10027, doi:10.1103/PhysRevB.56.R10024.

21. Baliga, B.J. Gallium Nitride Devices for Power Electronic Applications. *Semicond. Sci. Technol.* **2013**, *28*, 074011, doi:10.1088/0268-1242/28/7/074011.

22. Denbaars, S.P. Gallium-Nitride-Based Materials for Blue to Ultraviolet Optoelectronics Devices. *Proceedings of the IEEE* **1997**, *85*, 1740–1749, doi:10.1109/5.649651.

23. Romanczyk, B.; Zheng, X.; Guidry, M.; Li, H.; Hatui, N.; Wurm, C.; Krishna, A.; Ahmadi, E.; Keller, S.; Mishra, U.K. W-Band Power Performance of SiN-Passivated N-Polar GaN Deep Recess HEMTs. *IEEE Electron Device Letters* **2020**, *41*, 349–352, doi:10.1109/LED.2020.2967034.

24. Shrestha, P.; Guidry, M.; Romanczyk, B.; Hatui, N.; Wurm, C.; Krishna, A.; Pasayat, S.S.; Karnaty, R.R.; Keller, S.; Buckwalter, J.F. High Linearity and High Gain Performance of N-Polar GaN MIS-HEMT at 30 GHz. *IEEE Electron Device Letters* **2020**, *41*, 681–684.

25. Wong, M.H.; Keller, S.; Dasgupta, N., Sansaptak; Denninghoff, D.J.; Kolluri, S.; Brown, D.F.; Lu, J.; Fichtenbaum, N.A.; Ahmadi, E.; Singisetti, U.; et al. N-Polar GaN Epitaxy and High Electron Mobility Transistors. *Semicond. Sci. Technol.* **2013**, *28*, 074009, doi:10.1088/0268-1242/28/7/074009.

26. Al-Zuhairi, O.; Shuhaimi, A.; Nayan, N.; Azman, A.; Kamarudzaman, A.; Alobaidi, O.; Ghanim, M.; Abdullah, E.T.; Zhu, Y. Non-Polar Gallium Nitride for Photodetection Applications: A Systematic Review. *Coatings* **2022**, *12*, 275, doi:10.3390/coatings12020275.

27. Wang, T.; Oliver, R.A.; Taylor, R.A. Non-Polar Nitride Single-Photon Sources. *J. Opt.* **2020**, *22*, 073001, doi:10.1088/2040-8986/ab97c2.

28. Wang, T. Topical Review: Development of Overgrown Semi-Polar GaN for High Efficiency Green/Yellow Emission. *Semicond. Sci. Technol.* **2016**, *31*, 093003, doi:10.1088/0268-1242/31/9/093003.

29. Monavarian, M.; Rashidi, A.; Feezell, D. A Decade of Nonpolar and Semipolar III-Nitrides: A Review of Successes and Challenges. *Phys. Status Solidi A* **2018**, 1800628, doi:10.1002/pssa.201800628.

30. Schubert, E.F. *Light-Emitting Diodes*; 2nd ed.; Cambridge University Press: Cambridge, 2006; ISBN 978-0-511-79054-6.

31. Amano, H.; Collazo, R.; Santi, C.D.; Einfeldt, S.; Funato, M.; Glaab, J.; Hagedorn, S.; Hirano, A.; Hirayama, H.; Ishii, R.; et al. The 2020 UV Emitter Roadmap. *J. Phys. D: Appl. Phys.* **2020**, *53*, 503001, doi:10.1088/1361-6463/aba64c.

32. Wu, J. When Group-III Nitrides Go Infrared: New Properties and Perspectives. *Journal of Applied Physics* **2009**, *106*, 011101, doi:10.1063/1.3155798.

33. Park, J.-S.; Kim, J.K.; Cho, J.; Seong, T.-Y. Review—Group III-Nitride-Based Ultraviolet Light-Emitting Diodes: Ways of Increasing External Quantum Efficiency. *ECS J. Solid State Sci. Technol.* **2017**, *6*, Q42–Q52, doi:10.1149/2.0111704jss.

34. Ambacher, O.; Foutz, B.; Smart, J.; Shealy, J.R.; Weimann, N.G.; Chu, K.; Murphy, M.; Sierakowski, A.J.; Schaff, W.J.; Eastman, L.F.; et al. Two Dimensional Electron Gases Induced by Spontaneous and Piezoelectric Polarization in Undoped and Doped AlGaN/GaN Heterostructures. *Journal of Applied Physics* **2000**, *87*, 334–344, doi:10.1063/1.371866.

35. Ballestín-Fuertes, J.; Muñoz-Cruzado-Alba, J.; Sanz-Osorio, J.F.; Laporta-Puyal, E. Role of Wide Bandgap Materials in Power Electronics for Smart Grids Applications. *Electronics* **2021**, *10*, 677, doi:10.3390/electronics10060677.

36. Amano, H.; Kito, M.; Hiramatsu, K.; Akasaki, I. P-Type Conduction in Mg-Doped GaN Treated with Low-Energy Electron Beam Irradiation (LEEBI). *Jpn. J. Appl. Phys.* **1989**, *28*, L2112, doi:10.1143/JJAP.28.L2112.

37. Nakamura, S.; Senoh, M.; Mukai, T. Highly P-Typed Mg-Doped GaN Films Grown with GaN Buffer Layers. **1991**, doi:10.1143/JJAP.30.L1708.

38. Nakamura, S.; Mukai, T.; Senoh, M.S.M.; Iwasa, N.I.N. Thermal Annealing Effects on P-Type Mg-Doped GaN Films. *Jpn. J. Appl. Phys.* **1992**, *31*, L139, doi:10.1143/JJAP.31.L139.

39. Strite, S.; Morkoç, H. GaN, AlN, and InN: A Review. *Journal of Vacuum Science & Technology B: Microelectronics and Nanometer Structures Processing, Measurement, and Phenomena* **1992**, *10*, 1237–1266, doi:10.1116/1.585897.

40. Reuters, B.; Hahn, H.; Pooth, A.; Holländer, B.; Breuer, U.; Heuken, M.; Kalisch, H.; Vescan, A. Fabrication of P-Channel Heterostructure Field Effect Transistors with Polarization-Induced Two-Dimensional Hole Gases at Metal–Polar GaN/AlInGaN Interfaces. *J. Phys. D: Appl. Phys.* **2014**, *47*, 175103, doi:10.1088/0022-3727/47/17/175103.

41. Arakawa, Y.; Ueno, K.; Kobayashi, A.; Ohta, J.; Fujioka, H. High Hole Mobility P-Type GaN with Low Residual Hydrogen Concentration Prepared by Pulsed Sputtering. *APL Mater.* **2016**, *4*, 086103, doi:10.1063/1.4960485

42. Chen, J.; Brewer, W.D. Ohmic Contacts on P-GaN. *Adv. Electron. Mater.* **2015**, *1*, 1500113, doi:10.1002/aelm.201500113.

43. Shatalov, M.; Simin, G.; Jianping Zhang; Adivarahan, V.; Koudymov, A.; Pachipulusu, R.; Asif Khan, M. GaN/AlGaN p-Channel Inverted Heterostructure

JFET. *IEEE Electron Device Lett.* **2002**, *23*, 452–454, doi:10.1109/LED.2002.801295.

44. Li, G.; Jena, D.; Wang, R.; Song, B.; Verma, J.; Cao, Y.; Ganguly, S.; Verma, A.; Guo, J.; Xing, H.G. Polarization-Induced GaN-on-Insulator E/D Mode p-Channel Heterostructure FETs. *IEEE Electron Device Lett.* **2013**, *34*, 852–854, doi:10.1109/LED.2013.2264311.

45. Hahn, H.; Reuters, B.; Pooth, A.; Hollander, B.; Heuken, M.; Kalisch, H.; Vescan, A. P-Channel Enhancement and Depletion Mode GaN-Based HFETs With Quaternary Backbarriers. *IEEE Trans. Electron Devices* **2013**, *60*, 3005–3011, doi:10.1109/TED.2013.2272330.

46. Hahn, H. Threshold Voltage Engineering of GaN-Based n-Channel and p-Channel Heterostructure Field Effect Transistors, Thesis, 2015.

47. Chu, R.; Cao, Y.; Chen, M.; Li, R.; Zehnder, D. An Experimental Demonstration of GaN CMOS Technology. *IEEE Electron Device Lett.* **2016**, *37*, 269–271, doi:10.1109/LED.2016.2515103.

48. Bader, S.J.; Chaudhuri, R.; Nomoto, K.; Hickman, A.; Chen, Z.; Then, H.W.; Muller, D.A.; Xing, H.G.; Jena, D. Gate-Recessed E-Mode p-Channel HFET With High On-Current Based on GaN/AlN 2D Hole Gas. *IEEE Electron Device Lett.* **2018**, *39*, 1848–1851, doi:10.1109/LED.2018.2874190.

49. Bader, S.J.; Lee, H.; Chaudhuri, R.; Huang, S.; Hickman, A.; Molnar, A.; Xing, H.G.; Jena, D.; Then, H.W.; Chowdhury, N.; et al. Prospects for Wide Bandgap and Ultrawide Bandgap CMOS Devices. *IEEE Trans. Electron Devices* **2020**, *67*, 4010–4020, doi:10.1109/TED.2020.3010471.

50. Nomoto, K.; Bader, S.J.; Lee, K.; Bharadwaj, S.; Hu, Z.; Xing, H.G.; Jena, D. Wide-Bandgap Gallium Nitride p-Channel MISFETs with Enhanced Performance at High Temperature. In Proceedings of the 2017 75th Annual Device Research Conference (DRC); IEEE: South Bend, IN, USA, June 2017; pp. 1–2.

51. Chowdhury, N.; Lemettinen, J.; Xie, Q.; Zhang, Y.; Rajput, N.S.; Xiang, P.; Cheng, K.; Suihkonen, S.; Then, H.W.; Palacios, T. P-Channel GaN Transistor Based on p-GaN/AlGaN/GaN on Si. *IEEE Electron Device Lett.* **2019**, *40*, 1036–1039, doi:10.1109/LED.2019.2916253.

52. Chowdhury, N.; Xie, Q.; Yuan, M.; Cheng, K.; Then, H.W.; Palacios, T. Regrowth-Free GaN-Based Complementary Logic on a Si Substrate. *IEEE Electron Device Lett.* **2020**, *41*, 820–823, doi:10.1109/LED.2020.2987003.

53. Chowdhury, N.; Xie, Q.; Palacios, T. Self-Aligned E-Mode GaN *p* -Channel FinFET With I_{ON} > 100 MA/Mm and $I_{ON}/I_{OFF} > 10^7$. *IEEE Electron Device Lett.* **2022**, *43*, 358–361, doi:10.1109/LED.2022.3140281.

54. Zheng, Z.; Song, W.; Zhang, L.; Yang, S.; Wei, J.; Chen, K.J. High I_{on} and I_{on}/ I_{off} Ratio Enhancement-Mode Buried p-Channel GaN MOSFETs on p-GaN Gate Power HEMT Platform. *IEEE Electron Device Lett.* **2020**, *41*, 26–29, doi:10.1109/LED.2019.2954035.

55. Raj, A.; Krishna, A.; Hatui, N.; Gupta, C.; Jang, R.; Keller, S.; Mishra, U.K. Demonstration of a GaN/AlGaN Superlattice-Based p-Channel FinFET With High ON-Current. *IEEE Electron Device Lett.* **2020**, *41*, 220–223, doi:10.1109/LED.2019.2963428.

56. Raj, A.; Krishna, A.; Hatui, N.; Romanczyk, B.; Wurm, C.; Guidry, M.; Hamwey, R.; Pakala, N.; Keller, S.; Mishra, U.K. GaN/AlGaN Superlattice Based E-Mode p-Channel MES-FinFET with Regrown Contacts and >50 MA/Mm on-Current. In Proceedings of the 2021 IEEE International Electron Devices Meeting (IEDM); IEEE: San Francisco, CA, USA, December 11 2021; p. 5.4.1-5.4.4.

57. Kozodoy, P.; DenBaars, S.P.; Mishra, U.K. Depletion Region Effects in Mg-Doped GaN. *Journal of Applied Physics* **2000**, *87*, 770–775, doi:10.1063/1.371939.

58. Kozodoy, P.; Xing, H.; DenBaars, S.P.; Mishra, U.K.; Saxler, A.; Perrin, R.; Elhamri, S.; Mitchel, W.C. Heavy Doping Effects in Mg-Doped GaN. *Journal of Applied Physics* **2000**, *87*, 1832–1835, doi:10.1063/1.372098.

59. Kozodoy, P.; Hansen, M.; DenBaars, S.P.; Mishra, U.K. Enhanced Mg Doping Efficiency in $Al_{0.2}Ga_{0.8}N$/GaN Superlattices. *Appl. Phys. Lett.* **1999**, *74*, 3681–3683, doi:10.1063/1.123220.

60. Kozodoy, P.; Smorchkova, Y.P.; Hansen, M.; Xing, H.; DenBaars, S.P.; Mishra, U.K.; Saxler, A.W.; Perrin, R.; Mitchel, W.C. Polarization-Enhanced Mg Doping of AlGaN/GaN Superlattices. *Appl. Phys. Lett.* **1999**, *75*, 2444–2446, doi:10.1063/1.125042.

61. Kozodoy, P.; Keller, S.; DenBaars, S.P.; Mishra, U.K. MOVPE Growth and Characterization of Mg-Doped GaN. *Journal of Crystal Growth* **1998**, *195*, 265–269, doi:10.1016/S0022-0248(98)00676-9.

62. Amano, H.; Baines, Y.; Beam, E.; Borga, M.; Bouchet, T.; Chalker, P.R.; Charles, M.; Chen, K.J.; Chowdhury, N.; Chu, R.; et al. The 2018 GaN Power Electronics Roadmap. *J. Phys. D: Appl. Phys.* **2018**, *51*, 163001, doi:10.1088/1361-6463/aaaf9d.

63. Agarwal, A. Materials Development for Gallium Nitride Power Devices, Thesis, University of California, Santa Barbara, 2018.

64. Davis, R.F.; Bishop, S.M.; Mita, S.; Collazo, R.; Reitmeier, Z.J.; Sitar, Z. Epitaxial Growth Of Gallium Nitride. *AIP Conference Proceedings* **2007**, *916*, 520–540, doi:10.1063/1.2751931.

65. Krishna, A.; Raj, A.; Hatui, N.; Koksaldi, O.; Jang, R.; Keller, S.; Mishra, U.K. AlGaN/GaN Superlattice-Based P-Type Field-Effect Transistor with Tetramethylammonium Hydroxide Treatment. *Phys. Status Solidi A* **2020**, *217*, 1900692, doi:10.1002/pssa.201900692.

66. Kodama, M.; Sugimoto, M.; Hayashi, E.; Soejima, N.; Ishiguro, O.; Kanechika, M.; Itoh, K.; Ueda, H.; Uesugi, T.; Kachi, T. GaN-Based Trench Gate Metal Oxide Semiconductor Field-Effect Transistor Fabricated with Novel Wet Etching. *Appl. Phys. Express* **2008**, *1*, 021104, doi:10.1143/APEX.1.021104.

67. Quay, R. *Gallium Nitride Electronics*; Springer series in materials science; Springer: Berlin, 2008; ISBN 978-3-540-71890-1.

68. Smorchkova, I.P.; Haus, E.; Heying, B.; Kozodoy, P.; Fini, P.; Ibbetson, J.P.; Keller, S.; DenBaars, S.P.; Speck, J.S.; Mishra, U.K. Mg Doping of GaN Layers Grown by Plasma-Assisted Molecular-Beam Epitaxy. *Appl. Phys. Lett.* **2000**, *76*, 718–720, doi:10.1063/1.125872.

69. Xing, H.; Green, D.S.; Yu, H.; Mates, T.; Kozodoy, P.; Keller, S.; DenBaars, S.P.; Mishra, U.K. Memory Effect and Redistribution of Mg into Sequentially Regrown GaN Layer by Metalorganic Chemical Vapor Deposition. *Jpn. J. Appl. Phys.* **2003**, *42*, 50, doi:10.1143/JJAP.42.50.

70. Fichtenbaum, N.A.; Mates, T.E.; Keller, S.; DenBaars, S.P.; Mishra, U.K. Impurity Incorporation in Heteroepitaxial N-Face and Ga-Face GaN Films Grown by Metalorganic Chemical Vapor Deposition. *Journal of Crystal Growth* **2008**, *310*, 1124–1131, doi:10.1016/j.jcrysgro.2007.12.051.

71. Keller, S.; Li, H.; Laurent, M.; Hu, Y.; Pfaff, N.; Lu, J.; Brown, D.F.; Fichtenbaum, N.A.; Speck, J.S.; DenBaars, S.P.; et al. Recent Progress in Metal-Organic Chemical Vapor Deposition of N-Polar Group-III Nitrides. *Semicond. Sci. Technol.* **2014**, *29*, 113001, doi:10.1088/0268-1242/29/11/113001.

72. Lund, C.; Agarwal, A.; Romanczyk, B.; Mates, T.; Nakamura, S.; DenBaars, S.P.; Mishra, U.K.; Keller, S. Investigation of Mg δ-Doping for Low Resistance N-Polar p-GaN Films Grown at Reduced Temperatures by MOCVD. *Semicond. Sci. Technol.* **2018**, *33*, 095014, doi:10.1088/1361-6641/aad5cf.

73. Krishna, A.; Raj, A.; Hatui, N.; Keller, S.; Mishra, U.K. Investigation of Nitrogen Polar P-Type Doped GaN/Al $_{x}$ Ga $_{(1-x)}$ N Superlattices for Applications in Wide-

Bandgap p-Type Field Effect Transistors. *Appl. Phys. Lett.* **2019**, *115*, 172105, doi:10.1063/1.5124326.

74. Schroder, D.K. *Semiconductor Material and Device Characterization: Schroder/Semiconductor Material and Device Characterization, Third Edition*; John Wiley & Sons, Inc.: Hoboken, NJ, USA, 2005; ISBN 978-0-471-74909-7.

75. Keller, S.; Heikman, S.; Shen, L.; Smorchkova, I.P.; DenBaars, S.P.; Mishra, U.K. GaN–GaN Junctions with Ultrathin AlN Interlayers: Expanding Heterojunction Design. *Appl. Phys. Lett.* **2002**, *80*, 4387–4389, doi:10.1063/1.1484551.

76. Shen, L.; Heikman, S.; Moran, B.; Coffie, R.; Zhang, N.-Q.; Buttari, D.; Smorchkova, I.P.; Keller, S.; DenBaars, S.P.; Mishra, U.K. AlGaN/AlN/GaN High-Power Microwave HEMT. *IEEE Electron Device Lett.* **2001**, *22*, 457–459, doi:10.1109/55.954910.

77. Rajan, S.; Chini, A.; Wong, M.H.; Speck, J.S.; Mishra, U.K. N-Polar GaN/AlGaN/GaN High Electron Mobility Transistors. *Journal of Applied Physics* **2007**, *102*, 044501, doi:10.1063/1.2769950.

78. Prozheeva, V.; Makkonen, I.; Li, H.; Keller, S.; Mishra, U.K.; Tuomisto, F. Interfacial N Vacancies in Ga N /(Al , Ga) N / Ga N Heterostructures. *Phys. Rev. Applied* **2020**, *13*, 044034, doi:10.1103/PhysRevApplied.13.044034.

79. Ibbetson, J.P.; Fini, P.T.; Ness, K.D.; DenBaars, S.P.; Speck, J.S.; Mishra, U.K. Polarization Effects, Surface States, and the Source of Electrons in AlGaN/GaN Heterostructure Field Effect Transistors. *Appl. Phys. Lett.* **2000**, *77*, 250–252, doi:10.1063/1.126940.

80. Schaake, C.A.; Brown, D.F.; Swenson, B.L.; Keller, S.; Speck, J.S.; Mishra, U.K. A Donor-like Trap at the InGaN/GaN Interface with Net Negative Polarization and Its Possible Consequence on Internal Quantum Efficiency. *Semicond. Sci. Technol.* **2013**, *28*, 105021, doi:10.1088/0268-1242/28/10/105021.

81. Ogino, T.; Aoki, M. Mechanism of Yellow Luminescence in GaN. *Jpn. J. Appl. Phys.* **1980**, *19*, 2395–2405, doi:10.1143/JJAP.19.2395.

82. Lyons, J.L.; Janotti, A.; Van de Walle, C.G. Carbon Impurities and the Yellow Luminescence in GaN. *Appl. Phys. Lett.* **2010**, *97*, 152108, doi:10.1063/1.3492841.

83. Christenson, S.G.; Xie, W.; Sun, Y.Y.; Zhang, S.B. Carbon as a Source for Yellow Luminescence in GaN: Isolated C_N Defect or Its Complexes. *Journal of Applied Physics* **2015**, *118*, 135708, doi:10.1063/1.4932206.

84. Liang, F.; Zhao, D.; Jiang, D.; Liu, Z.; Zhu, J.; Chen, P.; Yang, J.; Liu, S.; Xing, Y.; Zhang, L.; et al. Carbon-Related Defects as a Source for the Enhancement of Yellow

Luminescence of Unintentionally Doped GaN. *Nanomaterials* **2018**, *8*, 744, doi:10.3390/nano8090744.

85. Saarinen, K.; Seppälä, P.; Oila, J.; Hautojärvi, P.; Corbel, C.; Briot, O.; Aulombard, R.L. Gallium Vacancies and the Growth Stoichiometry of GaN Studied by Positron Annihilation Spectroscopy. *Appl. Phys. Lett.* **1998**, *73*, 3253–3255, doi:10.1063/1.122735.

86. Armitage, R.; Hong, W.; Yang, Q.; Feick, H.; Gebauer, J.; Weber, E.R.; Hautakangas, S.; Saarinen, K. Contributions from Gallium Vacancies and Carbon-Related Defects to the "Yellow Luminescence" in GaN. *Appl. Phys. Lett.* **2003**, *82*, 3457–3459, doi:10.1063/1.1578169.

87. Neugebauer, J.; Van de Walle, C.G. Gallium Vacancies and the Yellow Luminescence in GaN. *Appl. Phys. Lett.* **1996**, *69*, 503–505, doi:10.1063/1.117767.

88. Tuomisto, F. Vacancy Defects in III-Nitrides: What Does Positron Annihilation Spectroscopy Reveal? *J. Phys.: Conf. Ser.* **2011**, *265*, 012003, doi:10.1088/1742-6596/265/1/012003.

89. Hautakangas, S.; Oila, J.; Alatalo, M.; Saarinen, K.; Liszkay, L.; Seghier, D.; Gislason, H.P. Vacancy Defects as Compensating Centers in Mg-Doped GaN. *Phys. Rev. Lett.* **2003**, *90*, 137402, doi:10.1103/PhysRevLett.90.137402.

90. Oila, J.; Saarinen, K.; Wickenden, A.E.; Koleske, D.D.; Henry, R.L.; Twigg, M.E. Ga Vacancies and Grain Boundaries in GaN. *Appl. Phys. Lett.* **2003**, *82*, 1021–1023, doi:10.1063/1.1542946.

91. Krishna, A.; Raj, A.; Hatui, N.; Sayed, I.; Keller, S.; Mishra, U.K. Proposed Existence of Acceptor-like Traps at Positive Polarization Interfaces in p-Type III-Nitride Semiconductors. *Appl. Phys. Lett.* **2020**, *117*, 042104, doi:10.1063/5.0015290.

92. Bader, S.J.; Chaudhuri, R.; Schubert, M.F.; Then, H.W.; Xing, H.G.; Jena, D. Wurtzite Phonons and the Mobility of a GaN/AlN 2D Hole Gas. *Appl. Phys. Lett.* **2019**, *114*, 253501, doi:10.1063/1.5099957.

93. Poncé, S.; Jena, D.; Giustino, F. Hole Mobility of Strained GaN from First Principles. *Phys. Rev. B* **2019**, *100*, 085204, doi:10.1103/PhysRevB.100.085204.

94. Poncé, S.; Jena, D.; Giustino, F. Route to High Hole Mobility in GaN via Reversal of Crystal-Field Splitting. *Phys. Rev. Lett.* **2019**, *123*, 096602, doi:10.1103/PhysRevLett.123.096602.

95. Krishna, A.; Raj, A.; Hatui, N.; Keller, S.; Denbaars, S.; Mishra, U.K. Acceptor Traps as the Source of Holes in P-Type N-Polar GaN/(AlN/AlGaN) Superlattices. *Appl. Phys. Lett.* **2022**, *120*, 132104, doi:10.1063/5.0083790.

96. Chaudhuri, R.; Bader, S.J.; Chen, Z.; Muller, D.A.; Xing, H.G.; Jena, D. A Polarization-Induced 2D Hole Gas in Undoped Gallium Nitride Quantum Wells. *Science* **2019**, *365*, 1454–1457, doi:10.1126/science.aau8623.

97. Du, H.; Liu, Z.; Hao, L.; Su, H.; Zhang, T.; Zhang, W.; Zhang, J.; Hao, Y. High-Performance E-Mode *p* -Channel GaN FinFET on Silicon Substrate With High I_{ON} / I_{OFF} and High Threshold Voltage. *IEEE Electron Device Lett.* **2022**, *43*, 705–708, doi:10.1109/LED.2022.3155152.

98. Chaudhuri, R.; Zhang, Z.; Xing, H.G.; Jena, D. Very High Density ($>10^{14}$ cm^{-2}) Polarization-Induced 2D Hole Gases Observed in Undoped Pseudomorphic InGaN/AlN Heterostructures. *Adv Elect Materials* **2022**, 2101120, doi:10.1002/aelm.202101120.

99. Chan, S.H.; Keller, S.; Tahhan, M.; Li, H.; Romanczyk, B.; DenBaars, S.P.; Mishra, U.K. High Electron Mobility Recovery in AlGaN/GaN 2DEG Channels Regrown on Etched Surfaces. *Semicond. Sci. Technol.* **2016**, *31*, 065008, doi:10.1088/0268-1242/31/6/065008.

Appendix A

STR-FETIS Model and Counting Mg Dopants in the SL

STR-FETIS is a software package in which we have used its 1-D Poisson solver capabilities, along with the quantum correction for holes to simulate the expected sheet charge and the energy band-diagrams for all the devices presented in the work. Figure A.1 shows the setup for a representative N-Polar SL structure in STR-FETIS.

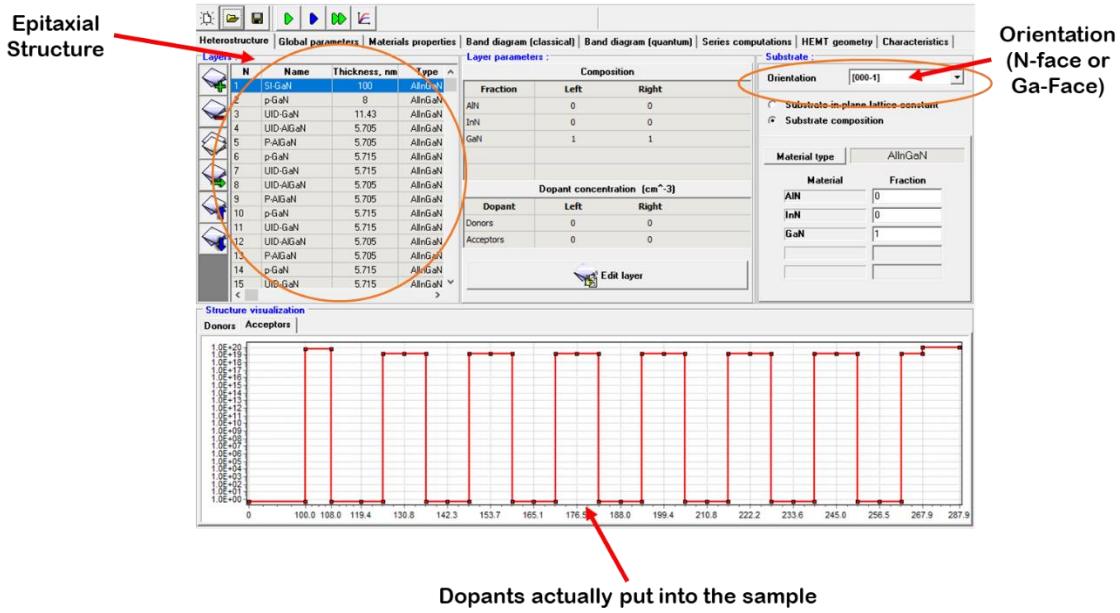

Figure A.1 Structure setup in STR-FETIS interface

Figure A.2 shows the post-simulation tabs from the package with calculated band-diagram (with quantum correction), carrier concentration, and polarization. Here, we use a representative 7-period N-polar GaN/AlGaN SL with 22% Al (and we see a calculated hole sheet charge of 7×10^{13} cm^{-2})

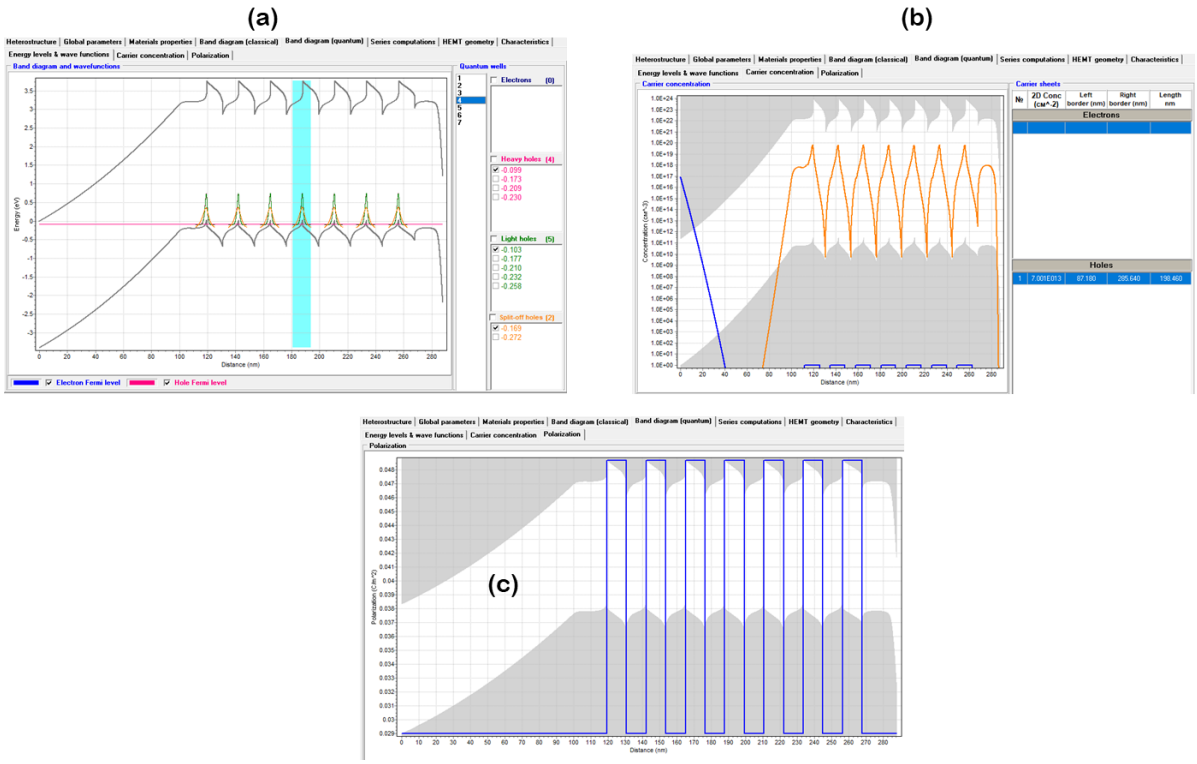

Figure A.2 Post-Simulation tabs from STR-FETIS – (a) calculated energy band diagrams with quantum correction, (b) carrier concentration in the structure, and (c) polarization in the simulated structure.

Before we started calculating band diagrams of samples where measured total sheet charge was greater than the calculated charge, we first carried out RT-Hall effect measurements on samples without any superlattice (shown in Figure A.3), and determined the contribution of holes from the contact layers, and the Mg-doped layer underneath the SL. The measured result was then compared to the calculated value from STR-FETIS. RT-Hall measurements on this activated "Control structure - 1" resulted in $p_s = 2.3\times10^{12}$ cm^{-2}, and this matched very well with the value calculated using the model developed in STR-FETIS (which gave a $p_s = 2.074\times10^{12}$ cm^{-2}). This made sense because the p-type layers without the superlattice can be considered as bulk p-type regions with very low incorporation (or ionization) of Mg dopants in the epitaxially grown layers.

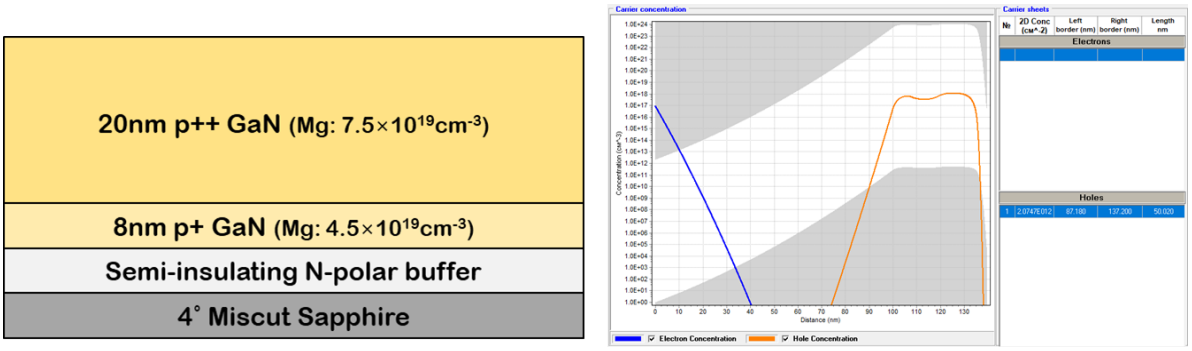

Figure A.3 Structure of the "Control Structure -1" without any superlattice, first measured using RT-Hall and then calculated with STR-FETIS. Total number of holes experimentally measured matched with the calculated value from the simulation model.

Next a second control SL series was grown, and the total sheet charge concentration of holes was measured using RT-Hall effect measurements. This control series was a 7-period N-Polar modulation doped SL stack in which each SL period was composed of 4nm p-GaN/ 4nm UID GaN/ x nm UID AlN/ (4-x) nm UID AlGaN (20% Al)/ 4nm p-AlGaN (20% Al), where AlN thickness x was varied from 0nm to 1.4nm, and p-type Mg doping was held constant at 1.5×10^{19} cm^{-3}. This structure is like the one presented in Chapter 4, but for all samples in this series, the acceptor traps were NOT expected to be ionized, and the measured total sheet charge of holes was expected to be the same as the value calculated using STR-FETIS. Figure A.4 shows the Total Sheet charge as a function of the AlN layer thickness and includes the calculated values from STR-FETIS – which is seen to be matching the experimentally measured value. After the corroboration of the experimental and calculated values of holes from these two sets of control samples, a dopant counting model was developed, as shown in Figure A.5, and this counting model was used for all the epitaxial structures presented in Chapters 4 and 5 – and to demonstrate the acceptor-like trap in p-type III-nitride systems.

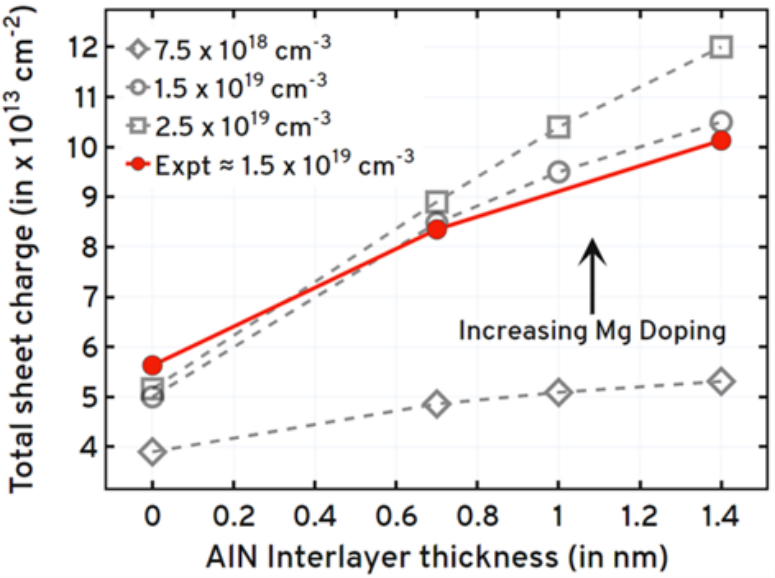

Figure A.4 Total sheet charge as a function of AlN interlayer thickness for Control Series 2. This includes simulated values (in gray, dotted lines) and the experimental data (solid line). There is substantial agreement between simulation and measurement (for the experimental doping of $1.5\times10^{19}cm^{-3}$). Note: This includes the contributed charges from the "bulk" regions ~ 5×10^{12} cm^{-2}.

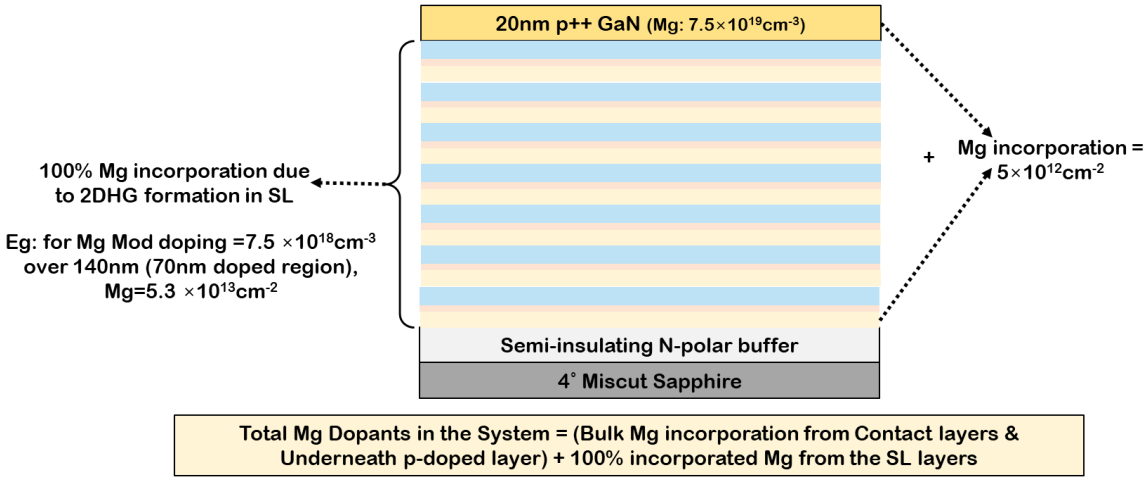

Figure A.5 Methodology for the counting of Mg dopants in the samples using simulations.

Whenever we have mentioned "greater than Mg dopants put into the sample" in this dissertation, we mean that the measured value of total sheet charge is greater than the total Mg dopants in the system according to Fig A.5 (since we have experimentally measured value for total number of Mg-incorporated holes from Control Structure 1 without any SL).